A View Into the Interstellar Medium of Galaxies Across Cosmic Time

Cortzen, Isabella Chi Gieseler

Publication date:
2020

Document version
Publisher's PDF, also known as Version of record

A view into the interstellar medium of galaxies across cosmic time

Dissertation submitted for the degree of

Philosophiæ Doctor

to the PhD School of the Faculty of Science,
University of Copenhagen

Isabella Chi Gieseler Cortzen

Supervisors
Associate Professor Georgios Magdis
Cosmic Dawn Center (DAWN)
Professor Sune Toft
Cosmic Dawn Center (DAWN)

Abstract

Ever since the discovery of galaxies, understanding their formation and evolution through cosmic time is one of the major challenges in modern astrophysics. During the last 15 years, substantial theoretical and observational evidence has shown that the majority of galaxies form well-known and relatively tight scaling relations. These include a relation between the star formation rate (SFR) and the stellar mass, dubbed the main sequence (MS) of star formation, and between the SFR and gas surface densities, known as the Schmidt-Kennicutt relation. These regularities underlying the observed properties have brought us to argue that the bulk of the stellar growth in galaxies mainly occurs through secular and steady evolution. A minor fraction of star-forming galaxies, named starbursts, are located well above the MS at all redshifts, where their extreme star formation is thought to be ignited following violent collisions. Although the details of the mechanisms responsible for triggering and quenching the star formation activity in main-sequence and starburst galaxies are still debated, it is clear that the available amount of molecular gas plays a major role in both these processes, since it constitutes the fuel for the birth of new stars. Therefore, accurate estimates of the gas mass and fraction in galaxies are key to interpret the buildup of stellar mass, and how the gas is transformed into stars. Quantifying the amount of molecular gas in galaxies has proved to be a major challenge for astrophysicists due to the lack of direct observables of H_2, the most abundant molecule in the Universe. As a consequence, we have to rely on indirect tracers, traditionally being carbon monoxide (CO) and dust. However, the use of these proxies suffers from uncertainties and degeneracies that prevent us from reaching definitive conclusions about the processes mentioned above. Exploring alter-

native tracers is thus imperative to reach a coherent picture of the interstellar medium (ISM) properties of galaxies.

The first part of this thesis is dedicated to this exploration. Specifically, I will compare the gas content using the classical CO and dust tracers with the emission from polycyclic aromatic hydrocarbons (PAHs). I will present evidence supporting the existence of a universal linear relation between the emission from PAHs and CO for galaxies on and above the MS. This relation implies that the PAH/CO luminosity ratio is independent of the star formation efficiency (SFE). This is at odds with the infrared/PAH luminosity ratio, which is rising with increasing SFE. In addition, a stronger correlation is found between the emission from PAHs and cold rather warm dust. All these results indicate that PAHs can trace the molecular gas mass similarly to CO and dust, rather than the total SFR, as commonly thought in the classical picture. This may impact future studies, as PAHs will be readily detectable up to $z \sim 3.5$ with the *James Webb Space Telescope*.

In the second part, I will focus on the dust and gas properties of a typical distant starburst galaxy to address several puzzling findings emerged during the last few years. These include unphysically large dust-to-stellar-mass ratios, which are inconsistent with the current models of dust production and destruction, in addition to surprisingly cold dust temperatures and faible radiation fields that are below that of main-sequence galaxies at similar redshift. As these extreme galaxies go through intense bursts of star formation activity, forming up to thousands of solar masses per year, these properties are perplexing. The latter are generally derived from sparse far-infrared spectral energy distributions (SEDs) and under the assumption of optically thin dust emission. However, a free opacity model provides an equally good description of the FIR SED, but with radically different implications on the physical properties of the dust. In this thesis, I will present a new method that can potentially break the degeneracy between optically thin and thick solutions. This method relies on the empirical correlation between the dust temperature and the gas excitation temperature derived from the neutral atomic carbon lines, [C I]. By means of new NOEMA observations, we will test this concept for a $z = 4$ starburst galaxy for which the [C I] gas temperature favors an optically thick solution, alleviating the observed tensions by returning a warmer dust temperature and a lower mass.

The last part of this thesis will be dedicated to future developments of the

methods presented here to bring them to full maturity. I will also introduce preliminary results of an ongoing project aimed at studying the radio and FIR emission in a sample of spectroscopically confirmed massive quiescent galaxies in the distant Universe, in order to investigate the presence of active galactic nuclei and possible residual pockets of dust, and gain insight into the physics of quenching. A brief introduction of this project will be presented in the last chapter.

Resumé

Galaksers tilblivelse og efterfølgende udvikling over kosmisk tid er en af de største udfordringer inden for den moderne astrofysik, siden opdagelsen af galakser. I løbet af de seneste 15 år har der været omfattende teoretiske og observationelle beviser for, at størstedelen af galakser danner velkendte og relativt tætte skaleringsforhold. Sådanne relationer inkluderer forholdet mellem hvor mange stjerner der dannes (SFR) og deres masse, som kaldes stjernedannelses-sekvensen (MS), samt mellem overfladetæthederne af SFR og gas, der kendetegnes som Schmidt-Kennicutt-relationen. Disse regelmæssigheder, der danner basis for de observerede egenskaber, har bragt os til den konklusion, at stjerners vækst hovedsagligt foregår via sekulær og stabil udvikling. En mindre brøkdel af de stjernedannende galakser, som kaldes starbursts, er placeret langt over stjernedannelses-sekvensen ved alle rødsforskydninger, hvor deres ekstreme stjernedannelse menes at antændes grundet voldelige kollisioner. Selvom detaljerne omkring de mekanismer, der er ansvarlige for at udløse og undertrykke stjernedannelsesaktiviteten i normale galakser og starburst-galakser stadig debatteres, så er det dog tydeligt, at mængden af gas der er til rådighed spiller en stor rolle i begge disse processer, da denne udgør selve brændstoffet, der bruges til at danne nye stjerner. Derfor er nøjagtige estimater af gasmassen og fraktionen af gas centrale for at fortolke hvordan stjernemassen i galakser opbygges, og hvordan gassen omdannes til stjerner. Det har vist sig at det at kvantificere mængden af molekylær gas i galakser er en stor udfordring for astrofysikere, da man ikke direkte kan måle mængden af H_2, som er det molekyle universet primært består af. Konsekvensen af dette er, at vi er nødsaget til at benytte indirekte metoder til at måle gassen, som traditionelt gøres ved at benytte kulilte (CO) og støv. Disse metoder inkluderer dog betydelige usikkerheder samt degenerationer, der forhindrer os i at opnå

definitive konklusioner på de ovennævnte processer. Det er således essentielt at udforske alternative metoder for at komme frem til et sammenhængende billede af det interstellare mediums (ISM) egenskaber i galakser.

Den første del af afhandlingen er dedikeret til denne udforskning. Jeg vil sammenligne gasmængden ved brug af klassiske CO- og støv-metoder med lyset fra polycykliske aromatiske carbonhydrider (PAHs). Jeg vil præsentere beviser, der understøtter eksistensen af en universel samt lineær relation mellem lyset fra PAHs og CO for galakser, der befinder sig på og ovenover MS-sekvensen. Denne relation indikerer, at forholdet mellem PAH/CO luminositeterne ikke afhænger af, hvor effektivt stjernerne dannes (SFE). Dette strider imod forholdet mellem infrarød/PAH luminositeterne, som øges ved stigende SFE. Derudover så indikerer disse resultater, at PAH molekylerne kan benyttes til at måle massen af molekylær gas, på samme vis som ved brug af CO og støv, fremfor at måle hvor mange stjerner der dannes, som tidligere konstateret. Dette kan således få betydning for fremtidige studier, da PAHs vil blive observeret op til $z \sim 3.5$ med *the James Webb Space Telescope*.

I den anden del vil jeg fokusere på støv- og gasegenskaberne i en typisk fjern starburst-galakse for at adressere flere forunderlige fund, der er opstået inden for de sidste par år. Dette inkluderer ufysisk store forhold mellem støv- og stjernemasser, som både strider imod de nuværende modeller for produktionen samt ødelæggelsen af støv, og derudover har overraskende kolde støvtemperaturer og svage strålingsfelter i forhold til MS-galakser ved samme rødforskydninger. Da disse ekstreme galakser gennemgår intense stjernedannende udbrud, hvor der produceres op til tusinder af solmasser om året, så virker disse egenskaber derfor uforståelige. Sidstnævnte udledes som regel ud fra galaksers spektrale energifordelinger (SED), der ofte er sparsomt dækket ved infrarøde (FIR) bølgelængder og under antagelse af, at lyset fra støvet er optisk tyndt. Derimod kan en model, der inkluderer en fri opacitet, give en tilsvarende god beskrive af galaksers FIR SED, men med radikalt forskellige konsekvenser for støvets fysiske egenskaber. I denne afhandling vil jeg præsentere en ny metode, som potentielt kan løse degenerationen mellem optisk tynde samt tykke løsninger. Metoden underbygges af den empiriske korrelation mellem støvtemperaturen og excitationstemperaturen af gassen, der er udledt ved brug af neutrale carbonlinjer, [C I]. Ved hjælp af nye NOEMA-observationer, da vil vi teste dette koncept for en starburst-galakse ved $z = 4$, hvor [C I]-gastemperaturen favoriserer en optisk tyk løsning,

som mildner de observerede spændinger ved både at returnere en varmere temperatur samt masse af støvet.

Den sidste del af afhandlingen vil blive dedikeret til at beskrive de fremtidige udviklinger af de metoder, der er blevet præsenteret. Jeg vil også introducere foreløbige resultater fra et igangværende projekt, hvis formål er at studere radio- samt infrarød-emission i et udpluk af spektroskopisk-bekr**ae**ftede massive galasker i det fjerne univers for at undersøge tilstedeværelsen af aktive galaksekerner (AGNs) og mulige resterende lommer af stæv, samt at få indblik i de fysiske processer der omhandler "quenching". En kort introduktion af dette projekt vil blive præsenteret i det sidste kapitel.

Contents

CHAPTER 1

Introduction

The formation and evolution of galaxies remain one of the major challenges of modern astrophysics. The word "galaxy" originates from Greek, meaning "milk", and refers to the fuzzy and milky appearance of our Galaxy when observed with the naked eye. In the seventeenth century, C. Huygens reported several diffuse and blurry objects, which were believed to be nebulae or stellar systems, known as island universes. Towards the end of the eighteenth century, W. Herschel suggested that some of these blurry nebulae could be island universes similar to the Milky Way. However, the nature of these island universes was controversial, as it was believed that these systems were either objects within our Milky Way or extra-galactic systems. These blurry systems were first confirmed to be at distances well beyond our Galaxy when Lemaître and Hubble independently of each other demonstrated that their recession velocity were proportional to their distance, confirming the expansion of the Universe (Lemaître 1927; Hubble 1929; Hubble & Humason 1931). At the time when A. Einstein published the general theory of relativity in 1917, he predicted that the Universe must either expand or contract and thus introduced the cosmological constant to support the idea of a static Universe (Einstein 1916). In 1922, A. Friedmann presented solutions to Einstein's field equations where he provided evidence for an expanding Universe (Friedmann

1922), which naturally suggested that the Universe was both smaller and denser in the past.

In this direction, R. Alpher, G. Gamow, and R. Herman suggested that the fundamental elements in the early Universe formed through primordial nucleosynthesis (Gamow 1946; Alpher, Bethe & Gamow 1948; Alpher & Herman 1949), which was later confirmed to take place within stars by A. Cameron and F. Hoyle among others (Hoyle 1946; Hoyle 1954; Cameron 1955). Moreover, R. Alpher and G. Gamow predicted that residual heat from the early Universe would still be visible as thermal background radiation if the Universe had expanded from a dense and hot initial state. This model, referred to as the Hot Big Bang theory, was strongly supported years after with the discovery of the cosmic microwave background (CMB, Dicke et al. 1965; Penzias & Wilson 1965). The CMB represents the earliest image of the Universe and changed our perception of the formation of the first structures in the Universe.

1.1 FROM THE GROWTH OF STRUCTURES TO GALAXIES

In 1990, the Cosmic Microwave Background Explorer (COBE) measured the background radiation temperature away from the Galactic plane, finding small variations that revealed the density fluctuations in the early Universe (Smoot et al. 1992). The observations provided information about the cosmological recombination, which took place roughly 400,000 years after the Big Bang. During this epoch, the temperature and density dropped, allowing lithium, helium, and hydrogen to recombine with electrons and start forming neutral atoms. In 1981, A. Guth suggested that the Universe went through a period of exponential expansion, known as inflation (Guth 1981), which was later modified by Linde (1982) and Albrecht & Steinhardt (1982). The inflation theory was able to explain both the homogeneity of the Universe on large scales and the observations of the primordial density fluctuations in the early Universe. These initial density variations acted as seeds, where the first structures formed through gravitational instability (Jeans 1902). These fluctuations would then eventually form large, complex systems such as galaxies.

Decades later, type Ia supernovae were reported to be effective standard candles to estimate cosmological distances through the distance-redshift relation, which provided evidence for that the expansion of the Universe is accelerating (Garnavich et al. 1998; Perlmutter et al. 1999). Their observations

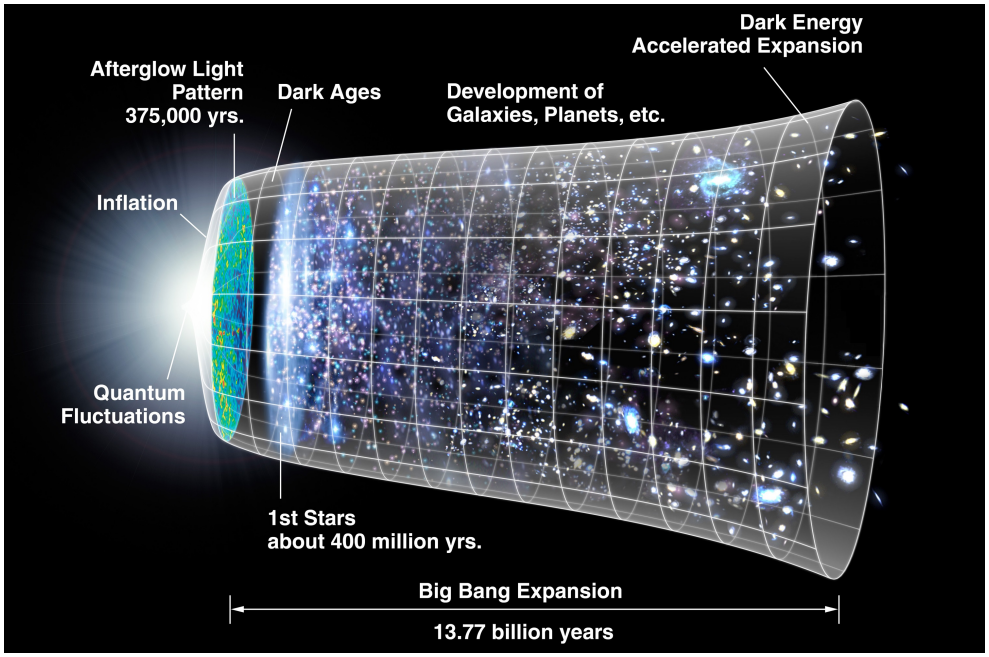

Figure 1.1: Figurative illustration of the history of the Universe based on observations and the current standard cosmological model. It presents some of the central events that occurred from the early phases of the cosmos to the present-day Universe. Image credit: WMAP Science Team.

favored the ΛCDM model as the standard cosmological model, which was able to explain the dynamics of the Universe and provide a model of the structure formation in agreement with the existing observations. The ΛCDM model describes a flat universe of which ∼ 75% of the energy density is due to the cosmological constant associated with dark energy (Λ), ∼ 21% is due to cold dark matter (CDM), and the remaining ∼ 4% is due to the baryonic matter out of which stars and galaxies form (Planck Collaboration et al. 2018).

The continuously growing observations of galaxies, closely following the development of improved telescopes and observatories, have established that the Milky Way is a sole drop in the ocean of a Universe containing hundreds of billions of galaxies spanning a wide range of shapes and sizes. The local Universe consists of a diverse crowd of galaxies, ranging from spiral galaxies similar to the Milky Way and its nearest neighbor Andromeda, starburst galaxies which are powerful and efficient factories to form stars, to "red and dead" massive elliptical galaxies representing the final phase of a galaxy's life. Since the lifetime of galaxies spans billions of years, observing how they

change and evolve over time is impossible. However, because time travels at a finite speed and due to the expansion of the Universe, observations of galaxies at farther distances enables one to peek into the past and capture a snapshot of their current state. As such, characterizing the physical properties of galaxies at different epochs of the Universe can be used to piece together their formation and evolution over cosmic time.

1.2 THE STAR FORMATION ACTIVITY IN GALAXIES

Understanding how galaxies in the nearby and distant Universe formed and evolved remains a challenge. During the last two decades, several works have established that the majority of star-forming galaxies (SFGs) follow a tight correlation between the star formation rate (SFR) and the stellar mass ($M_\star$) defining the so-called main-sequence (MS) of star formation (e.g., Brinchmann et al. 2004; Daddi et al. 2007; Elbaz et al. 2007; Noeske et al. 2007; Whitaker et al. 2012) with a normalization that increases as a function of redshift (e.g., Schreiber et al. 2015). On the other hand, starburst galaxies (SBs), a minor fraction of galaxies lying well above the MS (with SFR $\geq 4\times$ above the MS at fixed $M_\star$), are thought to undergo an accelerated mode of star formation. These galaxies form stars at prodigious rates, usually following stochastic events including mergers, where the collision triggers intense star formation as the gas rapidly compresses and cools (Sanders & Mirabel 1996). Lastly, galaxies falling well below the MS of star formation are classified as quiescent galaxies (QGs), which are no longer forming stars and thus at the endpoint of their life cycle.

In the local Universe, starburst galaxies are rare (making up only 2% of the integral of the IR luminosity function) and heavily dust-obscured with signs of an ongoing major merger (Sanders & Mirabel 1996; Rodighiero et al. 2011). They are classified as luminous and ultraluminous infrared galaxies (LIRGs and ULIRGs) with bolometric infrared luminosities (in the range $8-1000\,\mu$m) of $L_{\rm IR} > 10^{11}\,L_\odot$ and $> 10^{12}\,L_\odot$, respectively. As the specific star formation rate (sSFR = SFR/$M_\star$) rises with increasing redshift, the ULIRGs become the dominant population of galaxies at $z \sim 2$ (Le Floc'h et al. 2005). Do these high-redshift MS galaxies exhibit similar properties to that of local ULIRGs? Are major mergers dominating the cosmic star formation activity at high redshifts? A great deal of both observational and theoretical effort has been produced by the extragalactic astrophysical community to answer these

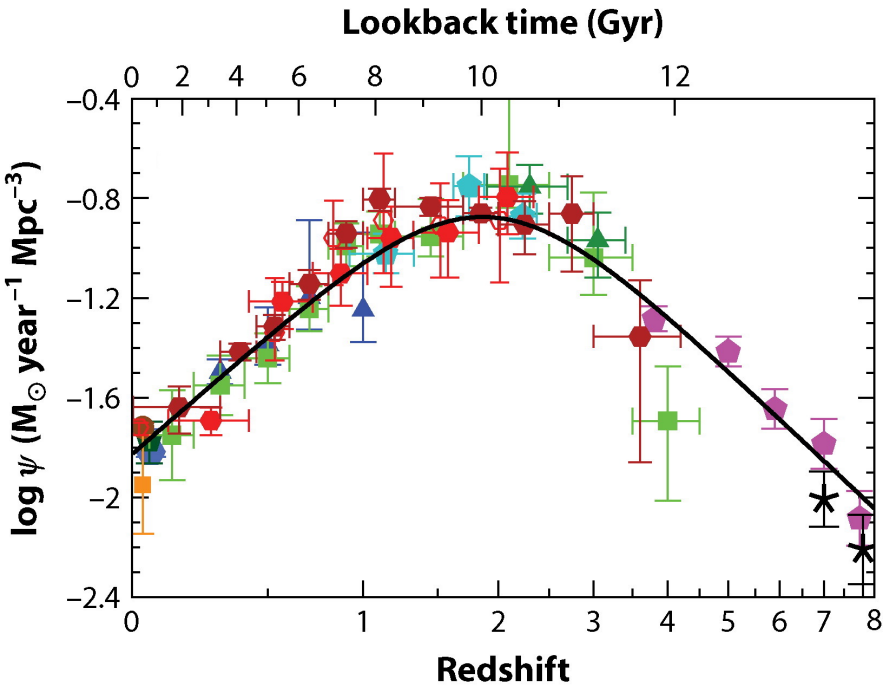

Figure 1.2: **SFRD:** The cosmic star formation rate density as a function of redshift from far-UV at $z < 3$ (blue, green) and at $z > 3$ (purple) and infrared (orange, red) rest-frame measurements. Figure is modified from Madau & Dickinson (2014).

fundamental questions.

Cosmic SFRD: Large galaxy surveys have unveiled that the Universe was more active in the past in terms of star formation (e.g., Le Floc'h et al. 2005, and references therein), where galaxies formed the bulk of their stellar mass at the peak of the cosmic star formation rate density (SFRD) at $z \sim 2-3$ (Figure 1.2). The tightness of the MS correlation at low and high redshift (with dispersions < 0.3 dex; Whitaker et al. 2012; Speagle et al. 2014) suggests that the majority of galaxies in the Universe are increasing their stellar mass through quasi-steady processes with smooth star formation histories (e.g., Elbaz et al. 2011; Sargent et al. 2012). Moreover, simulations report that gas compaction, depletion, and replenishment can explain the tightness of the MS, where the sSFR of galaxies can oscillate across the MS band (Tacchella et al. 2016). Do galaxies lying above the MS of star formation have more massive gas reservoirs or are they more efficient in converting their gas into stars?

Scoville et al. (2016) argue that starburst galaxies above the MS are simply more gas-rich and do not necessarily have higher star formation efficiencies (SFE $\equiv$ SFR/$M_{\mathrm{H_2}}$, where $M_{\mathrm{H_2}}$ is the molecular gas mass) than that of MS galaxies. Meanwhile, others suggest that two distinct modes of star formation exist, where MS galaxies follow the Schmidt-Kennicutt (SK) Law (Schmidt 1959; Kennicutt 1998; Kennicutt et al. 2003), a correlation between the star formation rate density (Σ_{SFR}) and the molecular gas surface density ($\Sigma_{\mathrm{H_2}}$), whereas SBs lie on a parallel sequence with systematically larger star formation efficiencies (Bouché et al. 2007; Daddi et al. 2010a; Genzel et al. 2010; Silverman et al. 2015; Magdis et al. 2017). These works find that galaxies exhibiting high SFEs (and thus short depletion timescales $\tau_{\mathrm{depl}} = M_{\mathrm{H_2}}/\mathrm{SFR} = 1/\mathrm{SFE}$) can maintain the current SFR for a short period of time of a few tens or hundreds million years, which is the opposite case for long-lasting star formation for main-sequence galaxies.

What is causing this exponential increase of the SFRD from $z = 0$ to the peak roughly 11 Gyr ago? Several works report an evolution of the gas fraction ($f_{\mathrm{gas}} = M_\star/M_{\mathrm{H_2}}$) with increasing redshift up to $z \sim 3$ (e.g., Daddi et al. 2008; Daddi et al. 2010a; Tacconi et al. 2008; Magdis et al. 2012a; Liu et al. 2019), where f_{gas} rises from 10% for local galaxies (Leroy et al. 2008) to $\sim 60\%$ at $z \sim 3$ (Tacconi et al. 2010; Daddi et al. 2010a; Geach et al. 2011; Magdis et al. 2012b; Saintonge et al. 2013; Santini et al. 2014; Genzel et al. 2015; Béthermin et al. 2015). Both simulations and semi-analytical models agree that the general decrease of the sSFR since the peak of the SFRD can be explained by a decline of gas accretion rate onto galaxies from the cosmic web (e.g., Bouché et al. 2010; Sparre et al. 2015; Mitchell et al. 2014), which determines how much gas is available to form stars, although this is yet to be confirmed by observations.

However, both the inferred SFE and f_{gas} heavily depend on the estimate of the mass of the molecular gas, which is the main driver for the growth of galaxies. How does the cold molecular gas in galaxies evolve with cosmic time? Its evolution is less well constrained than the SFRD as the validity of various gas tracers is still an open debate (e.g., Magdis et al. 2012b; Scoville et al. 2014; Genzel et al. 2015; Riechers et al. 2019; Decarli et al. 2019; Liu et al. 2019). To answer these fundamental questions, robust measurements of the gas content are thus imperative.

1.3 QUANTIFYING THE AMOUNT OF MOLECULAR GAS

As mentioned, the molecular gas represents the necessary fuel for the formation of new stars and is thus an essential component in terms of galaxy evolution. It is generally cold (10 – 50 K) due to inefficient heating by cosmic rays (in absence of UV radiation), and efficient cooling by molecular lines (Omont 2007). Although the majority of the molecular gas is dominated by molecular hydrogen (H_2), which is the most abundant molecule in the Universe, the emission from H_2 is rather difficult to observe due to its lack of a permanent dipole moment. As a consequence, the lower rovibrational transitions of H_2 are forbidden. Furthermore, because the first quadrupole line of H_2 lies 500 K above the ground state, it is excited in gas with temperatures above 100 K, significantly larger than the temperatures of giant molecular clouds (GMCs) where stars are formed. As the bulk of the molecular H_2 in galaxies is invisible in emission, reliable tracers are thus needed to detect the molecular gas reservoir.

1.3.1 *Carbon monoxide*

One of the most common molecular gas tracers is carbon monoxide (^{12}CO, hereafter CO), the second most abundant molecule after H_2, which is combined from oxygen and carbon in molecular clouds and is excited through a combination of collisional and radiative excitation (Carilli & Walter 2013). It is a favorable tracer due to several reasons. CO has a weak permanent dipole moment, a ground rotational transition ($\nu = 115.27$ GHz) with a relatively low excitation energy ($h\nu/k \approx 5.53$ K) and critical density ($n_{\rm crit} = 2.1 \times 10^3\,{\rm cm}^{-3}$), and it can easily be detected in cold molecular clouds from ground-based telescopes. As the emission from CO is reported to overlap in the same regions as molecular hydrogen, it is commonly assumed that the column density of H_2 is proportional to the CO(1 – 0) intensity (Bolatto, Wolfire & Leroy 2013). The intrinsic brightness of the CO lines depends on the excitation of the CO molecules, which is affected by the temperature and density of the gas. While the CO(1 – 0) is a tracer of the cold and diffuse molecular gas in galaxies, the emission from higher-J rotational lines of the CO molecule traces warmer and denser gas (Carilli & Walter 2013; Casey, Narayanan & Cooray 2014).

Since the first extra-galactic detection of CO was reported (Rickard et al. 1975), the wealth of data from facilities including the Atacama Large

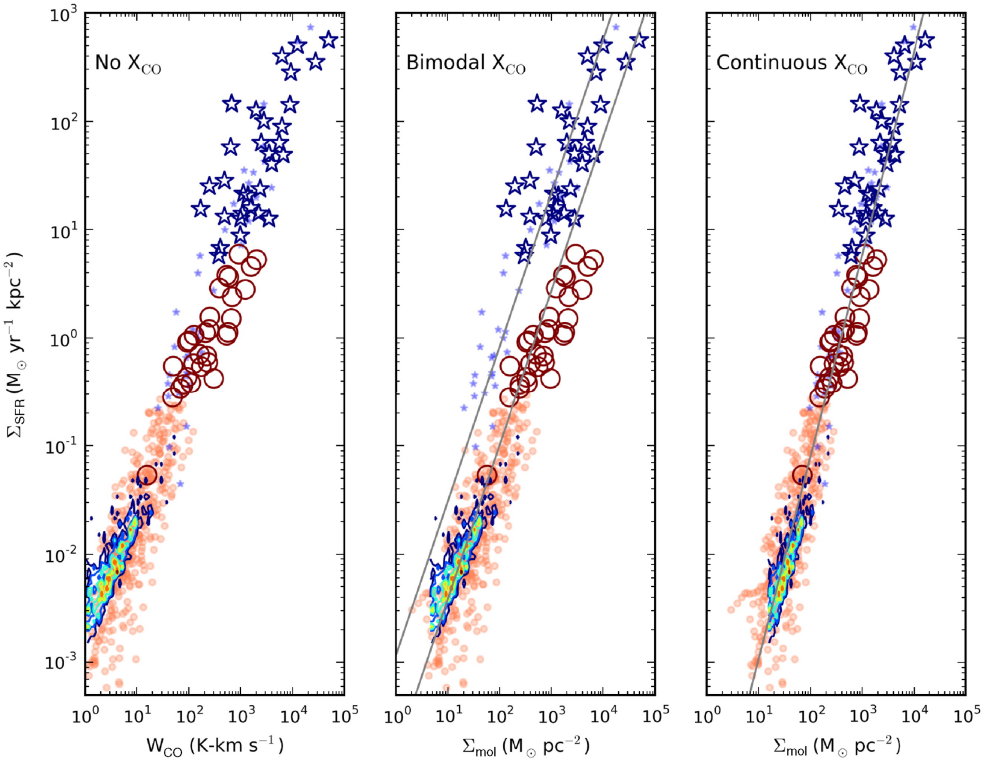

Figure 1.3: **SK-law.** The effect of adopting various CO–H_2 conversion factor on the Schmidt-Kennicutt law when including main-sequence galaxies (circles) and starbursts (stars). Local and high-redshift galaxies are shown as small and large symbols, respectively. *Left*: The correlation between the SFR surface density (Σ_{SFR}) and CO intensity (W_{CO}). *Center*: Σ_{SFR} as a function of H_2 surface density (Σ_{mol}), when adopting a bimodal X_{CO} for main-sequence and starburst galaxies. *Right*: Correlation between Σ_{SFR} and Σ_{mol} assuming a metallicity-dependent X_{CO}. Figures are from Casey, Narayanan & Cooray (2014).

Millimeter/submillimeter Array (ALMA), the Northern Extended Millimeter Array (NOEMA), and the Very Large Array (VLA) have grown and enabled large CO studies of various galaxies at both high and low redshift (e.g., Carilli & Walter 2013; Tacconi et al. 2013; Combes 2018; Decarli et al. 2019; Liu et al. 2019; Neri et al. 2020). The CO emission is commonly expressed as the areal integrated source brightness temperature in units of $\mathrm{K\,km\,s^{-1}\,pc^2}$ (Solomon & Vanden Bout 2005):

$$L'_{\mathrm{CO}} = 3.25\times10^7 \times S_{\mathrm{CO}}\Delta v \frac{D_L^2}{(1+z)^3 \nu_{\mathrm{obs}}^2}\,, \tag{1.1}$$

where $S_{\mathrm{CO}}\Delta v$ is the velocity integrated flux of the line in units of $\mathrm{Jy\,km\,s^{-1}}$, D_L is the luminosity distance in Mpc, z is the redshift, and ν_{obs} is the observed frequency of the line in GHz. Converting the CO line luminosity to a total molecular gas mass ($M_{\mathrm{H_2}}$) includes the α_{CO} conversion factor (Bolatto, Wolfire & Leroy 2013):

$$M_{\mathrm{H_2}} = \alpha_{\mathrm{CO}} L'_{\mathrm{CO}}\,, \tag{1.2}$$

where the molecular gas mass is in units of $M_\odot$, and α_{CO} in $M_\odot\,(\mathrm{K\,km\,s^{-1}\,pc^2})^{-1}$. The CO-$H_2$ conversion factor is often expressed as $X_{\mathrm{CO}} = N_{\mathrm{H_2}}/W_{\mathrm{CO}}$ in units of $\mathrm{cm^{-2}\,(K\,km\,s^{-1})^{-1}}$, where W_{CO} is the velocity-integrated CO intensity in units of ($\mathrm{K\,km\,s^{-1}}$) and $N_{\mathrm{H_2}}$ is the column density of the gas. The conversion between α_{CO} and X_{CO} is: $X_{\mathrm{CO}} = 6.3\times10^{19}\times\alpha_{\mathrm{CO}}$[1]. Although the CO conversion factor is well-calibrated at low redshift (in particular for the Milky Way), it varies significantly with metallicity (Z), galaxy type, molecular gas surface density, and kinematic state (e.g., Bolatto, Wolfire & Leroy 2013; Casey, Narayanan & Cooray 2014). Moreover, it is common practice to apply different α_{CO} values for MS and SB galaxies, which exacerbates the difference between these two populations in the SFR – $M_{\mathrm{H_2}}$ plane (Figure 1.3). For local ULIRGs, the α_{CO} is a factor of ~ 6 smaller than that of normal spiral galaxies with $\alpha_{\mathrm{CO}} \sim 4\,\mathrm{M_\odot\,(K\,km\,s^{-1}\,pc^2)^{-1}}$ (Downes & Solomon 1998; Daddi et al. 2010a; Leroy et al. 2011; Magdis et al. 2011), whereas for high-redshift submillimeter galaxies (SMGs), an upper limit of $\alpha_{\mathrm{CO}} \sim 0.8\,\mathrm{M_\odot\,(K\,km\,s^{-1}\,pc^2)^{-1}}$ have been reported to avoid that the inferred gas masses become larger than the dynamical masses (Tacconi et al. 2008; Carilli et al. 2010; Magdis et al. 2011; Hodge et al. 2012). Computational models of galaxy disks and mergers report that the α_{CO}

[1] If including the contribution from Helium, a factor of $\sim 4.65\times10^{19}$ should be applied to the conversion between X_{CO} and α_{CO}.

conversion factor decreases in massive mergers during the starburst phase with high gas surface densities (Narayanan et al. 2011; Narayanan et al. 2012). Furthermore, the conversion factor is reported to increase for low-metallicity galaxies (Wolfire, Hollenbach & McKee 2010; Krumholz, Leroy & McKee 2011; Genzel et al. 2012; Lagos et al. 2012), where the CO line luminosity decreases as Z^{-2} (Israel 1997). This effect has been attributed to smaller CO emitting gas regions, and less dust shielding which causes CO to be photodissociated by far-UV radiation (e.g., Narayanan et al. 2012; Bolatto, Wolfire & Leroy 2013). In such low-metallicity systems, CO dark molecular clouds are thus expected (Papadopoulos, Thi & Viti 2002; Wolfire, Hollenbach & McKee 2010; Leroy et al. 2011; Genzel et al. 2012). As the metallicity decreases with increasing redshift, photodissociation of CO may hamper detections of the molecular gas in galaxies and reach a point where CO becomes and inefficient tracer of the H_2 gas. Furthermore, both observational studies (Allen et al. 2012; Langer et al. 2014; Pineda et al. 2017), and theoretical works (Wolfire, Hollenbach & McKee 2010; Smith et al. 2014; Glover & Smith 2016) suggest that even under typical local interstellar medium (ISM) conditions, 30 – 70% of the total H_2 mass might be located in CO-poor regions.

1.3.1.1 Using dust to derive $M_{\rm gas}$

Alternative methods that are commonly used to infer the molecular gas mass of galaxies include the relation between the dust mass (see also Section 1.4) and gas-to-dust ratio ($M_{\rm d} - \delta_{\rm GDR}$), in addition to using single-band measurements of the dust continuum at the Rayleigh-Jeans (RJ) tail of the dust SED. As these techniques are relatively inexpensive in terms of observing time when compared to molecular line spectroscopy, they provide powerful tools to infer the molecular gas mass in galaxies at both low and high redshift.

Dust mass: The total gas-to-dust ration ($\delta_{\rm GDR}$) in the ISM has been reported to correlate with the metallcity in local (Leroy et al. 2011) and $0 < z < 2$ star-forming galaxies (Magdis et al. 2012b), where $\delta_{\rm GDR}$ increases with decreasing metallicity (Figure 1.4):

$$\log\delta_{\rm GDR} = (10.54 \pm 1.00) - (0.99 \pm 0.12) \times (12 + \log({\rm O/H})), \qquad (1.3)$$

where $Z = (12+\log({\rm O/H}))$ is the metallicity expressed as the gas-phase oxygen abundance. The molecular gas masses can then be inferred assuming (Magdis

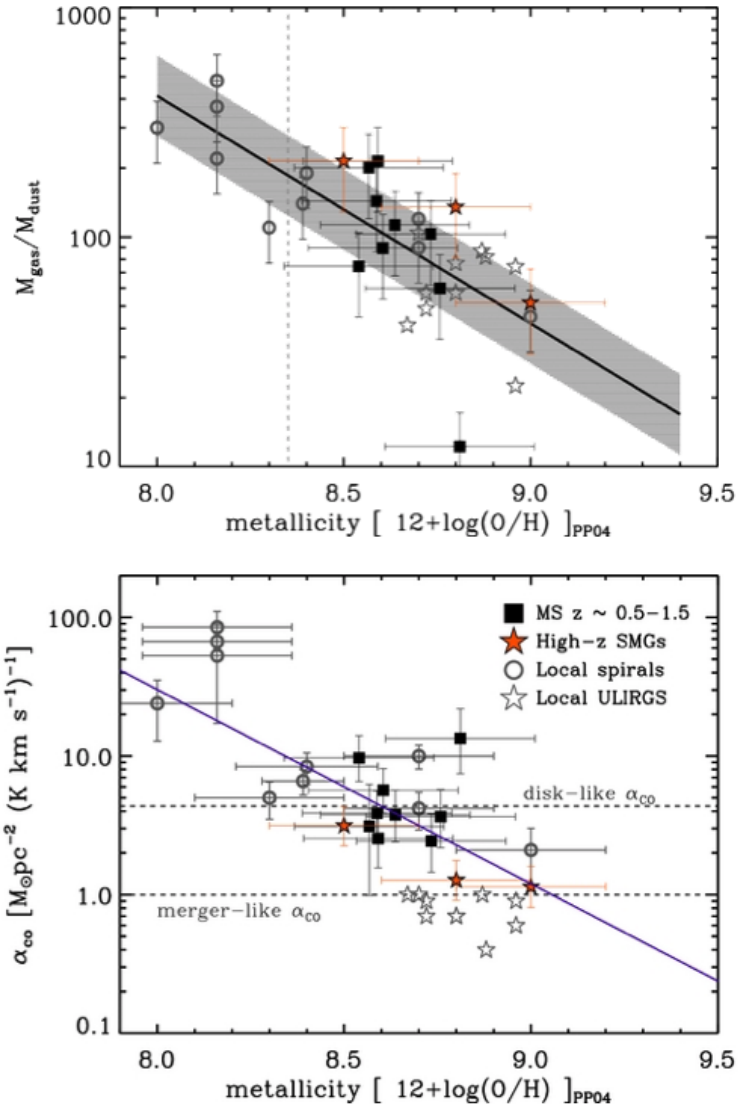

Figure 1.4: $M_{\rm d}$ **inferred gas masses.** *Upper*: Total gas to dust mass ratio ($M_{\rm gas}/M_{\rm d}$) as a function of metallicity of nearby galaxies in the Local Group (Leroy et al. 2011) (grey circles), ULIRGs (Downes & Solomon 1998) (grey stars), and $z \sim 0.5 - 1.5$ main-sequence galaxies (black squares) and high-redshift SMGs (orange stars) (Magdis et al. 2012b) with $\alpha_{\rm CO}$ inferred from the $\alpha_{\rm CO}$–metallicity relation (lower panel). The best-fitted relation and the dispersion of the Local Group galaxies are shown as the solid black line. The lowest metallicity used in the study is shown as the dashed line ($Z \sim 8.35$). *Lower*: $\alpha_{\rm CO}$ inferred using the $\delta_{\rm GDR}$ method as a function of metallicity, where the solid line shows the best-fitted line to the galaxies when excluding the local ULIRGs. Figures are from Magdis et al. (2012b).

et al. 2011; Magdis et al. 2012b):

$$M_{\rm gas} \equiv \delta_{\rm GDR} M_{\rm dust} = M_{\rm H_2} + M_{\rm HI} \ , \tag{1.4}$$

where $M_{\rm dust}$ is the dust mass in units of $M_\odot$ and $M_{\rm gas}$ is the total gas mass including both the contribution from the molecular ($M_{\rm H_2}$) and atomic ($M_{\rm HI}$) gas. For high-redshift galaxies, both observational and theoretical works suggest that the molecular gas dominates such that $M_{\rm gas} \approx M_{\rm H_2}$ (Obreschkow et al. 2009; Daddi et al. 2010a; Tacconi et al. 2010; Geach et al. 2011; Lagos et al. 2011). The dust-derived $M_{\rm gas}$ has previously been reported to be consistent with that of CO within a factor of $\sim 2\times$ when the FIR SED is well sampled up to a rest-frame 160 µm yielding secure estimates of $M_{\rm d}$ (e.g., Berta et al. 2016). As for the CO-based method, the derivation of the molecular gas mass from dust depends on the, metallicity which can be challenging to assess especially for starburst and low-metallicity galaxies. While the $M_{\rm d} - \delta_{\rm GDR}$ method assumes that the gas-to-dust mass ratio holds for galaxies regardless of the redshift, variations of the balance of dust creation and destruction or changes of the dust grain properties may lead to changes in $\delta_{\rm GDR}$ (e.g., Bolatto, Wolfire & Leroy 2013). Moreover, recent works by Rémy-Ruyer et al. (2014) and Capak et al. (2015) report strong variations of $\delta_{\rm GDR}$ with metallicity, suggesting that the relation changes at low Z.

RJ dust continuum: Another approach is to use the Rayleigh-Jeans tail of the dust SED to infer the mass of the molecular ISM ($M_{\rm ISM}$) and $M_{\rm gas}$ (Scoville et al. 2014; Scoville et al. 2016), which has been reported to be tightly correlated with the emission from CO in both nearby and distant ($z \sim 2-3$) galaxies (Scoville et al. 2016; Hughes et al. 2017; Bertemes et al. 2018; Saintonge et al. 2018; Kaasinen et al. 2019). This method uses the rest-frame 850 µm to estimate the ISM mass which has been calibrated to a sample of 70 galaxies with CO(1 – 0) and $M_\star > 10^{10}\,M_\odot$ (including 28 local SFGs, 12 local ULIRGs, and 30 SMGs at $z \sim 2$), where the dust-to-gas ratios are $\sim 1:100$, thus excluding low-metallicity systems and thus variations in $\delta_{\rm GDR}$ (Figure 1.5), and later recalibrated using larger samples of galaxies (e.g., Hughes et al. 2017). This method assumes that the dust continuum at rest-frame 850 µm is optically thin, mixed within the ISM, and that the observed flux density is proportional to the mass of dust. The gas mass can thus be derived after multiplying by the conversion factor $\alpha_{\nu_{850\ \mu\rm m}} \equiv L_{\nu_{850\,\mu\rm m}}/M_{\rm gas} = (6.7 \pm 1.7) \times 10^{19}\,{\rm erg\,s^{-1}\,Hz^{-1}}\,{M_\odot}^{-1}$, where $L_{\nu_{850\,\nu\rm m}}$is the luminosity at 850 µm (Scoville et al. 2017a). The latter

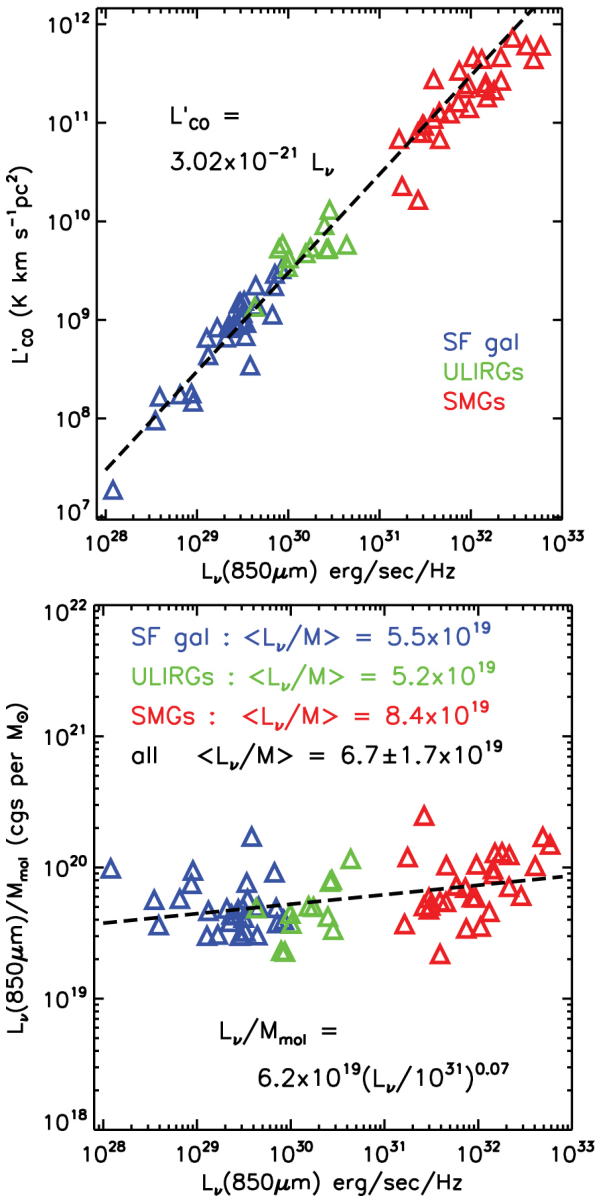

Figure 1.5: **Gas masses from dust continuum.** *Upper*: Correlation between CO(1 – 0) and 850 µm luminosity for low-redshift star-forming galaxies (blue) and ULIRGs (green), and SMGs at $z \sim 2$ (red). *Lower*: 850 µm luminosity to molecular gas mass ratio as a function of the 850 µm luminosity, where the molecular gas masses are estimated assuming $X_{\rm CO} = 3 \times 10^{20}\,{\rm N(H_2)\,cm^{-2}\,(K\,km\,s^{-1})^{-1}}$. Figures are from Scoville et al. (2016).

can either be estimated by fitting the FIR SED (Hughes et al. 2017) or from a single-band measurement in the RJ tail, assuming a dust opacity coefficient and mean mass-weighted temperature of the dust, which is often assumed to be $\langle T_{\rm d} \rangle = 25\,{\rm K}$ (Scoville et al. 2016; Scoville et al. 2016). Recent simulations suggest that the $M_{\rm gas}$ derived using the RJ dust technique correlates with the actual molecular gas mass of massive star-forming galaxies, although the method breaks down for galaxies with $L_{\nu_{850\,\mu{\rm m}}} < 10^{28}\,{\rm erg\,s^{-1}}$ or low metallicities with $\log(Z/Z_{\odot}) < -0.8$ (Liang et al. 2018; Privon, Narayanan & Davé 2018). Furthermore, Genzel et al. (2015) derive gas mass estimates from CO and dust emission for galaxies at $z \sim 0-3$, finding that the dust continuum method on average underestimate the inferred $M_{\rm gas}$ by 0.3 dex, when excluding a metallicity dependent dust-to-gas ratio. Moreover, several studies report an increasing dust temperature with redshift for galaxies on and above the MS (Elbaz et al. 2011; Nordon et al. 2012; Magnelli et al. 2014; Béthermin et al. 2015; Schreiber et al. 2018), which may affect the inferred $M_{\rm gas}$ estimates for high-redshift galaxies under the assumption of a constant $\langle T_{\rm d} \rangle = 25\,{\rm K}$. This will be further discussed in Chapter 1.4.2.

To determine the cosmic evolution of the cold molecular gas mass density, a recent study by Liu et al. (2019) combine existing dust continuum observations of ~ 700 galaxies at $0.3 < z < 6.0$ from the ALMA archive in the COSMOS deep field with $\sim 1{,}000$ CO observations of galaxies at $0 < z < 4$. The combined sample allows for a comparison of the molecular gas mass estimates using CO lines, dust masses, and dust continuum observations at the RJ-tail assuming various $\alpha_{850\,\mu{\rm m}}$ conversion factors. They find systematic offsets of 0.15 – 0.25 dex between the estimates of $M_{\rm gas}$, where the $M_{\rm d} - \delta_{\rm GDR}$ systematically underestimate the gas mass when compared to those inferred using CO lines and the RJ–$\alpha_{850\,\mu{\rm m}}$ approach. Figure 1.6 presents the redshift evolution of the molecular gas mass density where metallicity-dependent $\alpha_{\rm CO}$ values have been used to convert the CO line emission to $M_{\rm gas}$ and dust continuum emission has been converted after adopting the $\alpha_{850\,\mu{\rm m}}$ from Hughes et al. (2017). Although a cosmic evolution of the molecular gas mass is emerging with a trend similar to that of the cosmic SFRD, the uncertainties linked to the $\alpha_{\rm CO}$ and $\alpha_{850\,\mu{\rm m}}$ conversion factors and how these vary with physical properties (metallicity, cosmic rays, redshift etc.) may affect the inferred gas mass densities.

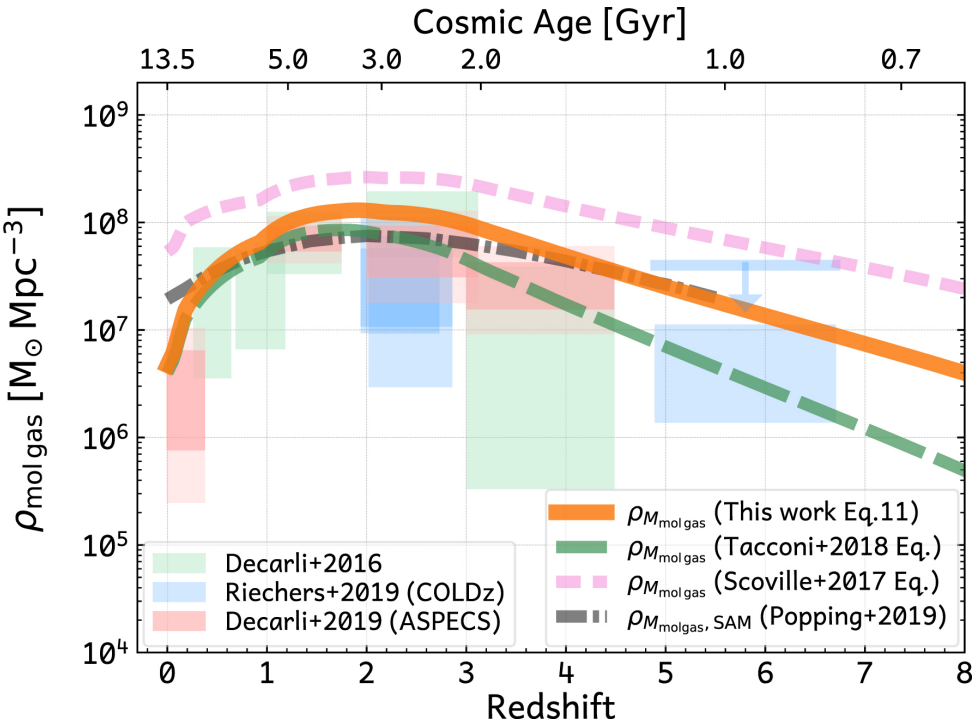

Figure 1.6: **Cosmic evolution of CO- and dust-inferred molecular gas mass.** The evolution of the cold molecular gas mass density as a function of redshift based on the large ALMA compilation of Liu et al. (2019), in addition to the numerous CO studies included from the literature. CO blind deep field studies from Decarli et al. (2016) (green), Riechers et al. (2019) (blue), and Decarli et al. (2019) (red) are also shown. For comparison, the integrated cosmic cold molecular gas density obtained from the computed gas fraction functions from Liu et al. (2019) (orange line), Tacconi et al. (2018) (green dashed line), and Scoville et al. (2017a) (pink dashed line) are shown. The results based on semi-analytic model simulation from Popping et al. (2019) is presented as well (grey dashed line). Figure is from Liu et al. (2019).

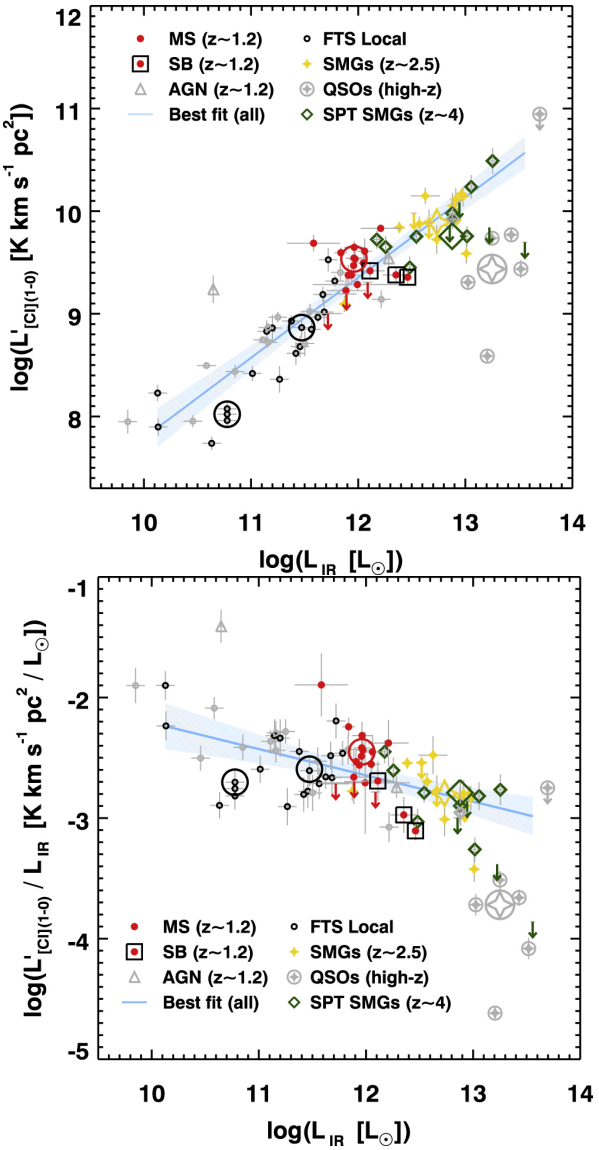

Figure 1.7: **[CI] and SFR.** *Upper*: Correlation between [C I]($^3P_1 - {}^3P_0$) and IR luminosity for local SFGs (black circles) and AGNs (gray circles). At $z \sim 1.2$ main-sequence (red circles), starburst galaxies (red circles within black squares) and AGNs (gray triangles) are included, in addition to SMGs at $z \sim 2.5$ (yellow stars), high-redshift QSOs (gray stars and open circles), and SPT SMGs at $z \sim 4$ (open green diamonds). The best-fitted line regression and 95% confidence interval for the star-formation dominated galaxies is shown as the blue line and colored area, respectively. *Lower*: [C I]($^3P_1 - {}^3P_0$)/IR luminosity ratio, probing the gas depletion timescale, as a function of IR luminosity. Figures are from Valentino et al. (2018).

1.3.2 *Neutral atomic carbon*

An alternative proxy for the molecular gas content is the neutral atomic carbon ([C I]). Its two line transitions, [C I]($^3P_1 - {}^3P_0$) at $\nu_{\rm rest} = 492.161\,$GHz and [C I]($^3P_2 - {}^3P_1$) at $\nu_{\rm rest} = 809.344\,$GHz, have been proposed as a superior molecular gas tracer than CO(1 – 0) (Papadopoulos, Thi & Viti 2004). In particular, in local starbursting ULIRGs, [C I] has been proposed as a powerful tool to study the molecular gas in galaxies with high cosmic ray rates where CO is easily destroyed (Papadopoulos, Thi & Viti 2004; Papadopoulos, Bisbas & Zhang 2018; Bisbas, Papadopoulos & Viti 2015; Bisbas et al. 2017). Traditionally, the emission from [C I] is thought to originate from the surface of photodissociation regions (PDRs) where CO is dissociated by UV radiation from young stars (Carilli & Walter 2013). However, several works suggest that [C I] is closely associated with the CO emission and effectively maps the bulk of the molecular gas in galaxies (Ojha et al. 2001; Weiß et al. 2003). [C I] has a similar critical density as CO(1 – 0) of $n_{\rm crit} \approx 10^3\,{\rm cm}^{-3}$, which suggests that the [C I] emission arises from the same volumes and shares similar excitation temperatures to that of CO(1 – 0) (Ikeda et al. 2002). Furthermore, a constant ratio of $N({\rm CO})/N([{\rm CI}]) \sim 0.1 - 0.2$ has been reported over a large range of conditions (Ojha et al. 2001; Ikeda et al. 2002). Moreover, models suggests that the [C I]($^3P_1 - {}^3P_0$) luminosity is better correlated with the $M_{\rm H_2}$ than CO(1 – 0) and ionized carbon ([C II]) over a wide range of gas densities ($n = 10 - 10^4\,{\rm cm}^{-3}$) and independently of the intensity of the radiation field (Madden et al. 2020, in prep).

Numerous observations of [C I] have been reported in the literature, including in molecular clouds within the Milky Way (Ojha et al. 2001; Ikeda et al. 2002), and local and high-redshift galaxies (for a recent compilation of the extragalactic [C I] detections see Valentino et al. 2020a and references therein). In Valentino et al. (2018), the authors report that the [C I]($^3P_1 - {}^3P_0$) and low-J CO line emissions correlate on global scales for both local IR luminous galaxies, MS and SBs at $z \sim 1$, and SMGs at high-redshift. Furthermore, they report a systematic variation of the [C I]($^3P_1 - {}^3P_0$)/IR luminosity ratio of normal MS and SB galaxies, a behavior similar to that of the CO/IR luminosity ratio, which indicates different star formation modes for MS and SB galaxies.

As the fine structure system of [C I] forms a simple three-level system, the emission from the [C I] line transitions can be used to derive the excitation temperature ($T_{\rm ex}$), the column density of [C I], and the mass of [C I]

($M_{[CI]}$) which can be converted into M_{H_2} (Ojha et al. 2001; Weiß et al. 2003; Walter et al. 2011). Under the assumption of local thermodynamical equilibrium (LTE) and assuming that both [C I] line transitions are optically thin, the excitation temperature can be derived as $T_{ex} = 38.8/\ln(2.11/R)$, where $R = L'_{[CI](^3P_2-^3P_1)}/L'_{[CI](^3P_1-^3P_0)}$ is the ratio of the [C I] line luminosities[2] (Stutzki et al. 1997; Schneider et al. 2003). The neutral atomic carbon mass can be derived from the $[C\,I](^3P_1 - {}^3P_0)$ line as follows[3] (Weiß, Walter & Scoville 2005):

$$M_{[CI]} = 5.706 \times 10^{-4} Q(T_{ex}) \frac{1}{3} e^{(23.6\,K/T_{ex})} L'_{[CI]^3P_1-^3P_0}\,, \tag{1.5}$$

in units of $M_\odot$, where $Q(T_{ex}) = 1 + 3e^{(-23.6\,K/T_{ex})} + 5e^{(-62.5\,K/T_{ex})}$ is the partition function of [C I]. The estimate of $M_{[CI]}$ derived from $[C\,I](^3P_1 - {}^3P_0)$ is expected to be insensitive to $T_{ex} > 20\,K$ (Weiß, Walter & Scoville 2005; Bothwell et al. 2017). The $M_{[CI]}$ can then be converted to M_{H_2} after applying a conversion factor, $X_{[CI]} = [CI]/H_2 = M_{[CI]}/(6M_{H_2})$, describing the abundance of [C I] relative to H_2 when excluding the contribution from helium (Ikeda et al. 2002; Weiß et al. 2003; Walter et al. 2011; Valentino et al. 2018). A common approach is to adopt the derived abundance from a mixed sample of local starburst galaxies and nearby clouds of $X_{[CI]} = 3 \times 10^{-5}$ (Weiß et al. 2003; Papadopoulos, Thi & Viti 2004). However, as the [C I]-inferred M_{H_2} scales as $([CI]/[H_2])^{-1}$, adopting a universal value can highly bias the estimate of M_{H_2}. Moreover, if M_{H_2} is inferred based on dust or CO emission, the uncertainties of these tracers affect the calibration of [C I] (e.g., Valentino et al. 2018).

1.4 THE DUST IN THE INTERSTELLAR MEDIUM

In the previous sections, we described the importance of the cold molecular gas in regulating the formation and evolution of galaxies, and the challenges we face when trying to estimate its mass and properties. Although it was briefly described how dust can be used to derive M_{gas}, the importance of this component goes well beyond its simple use as a proxy for the cold gas. In the ISM, dust is directly connected with the galaxy growth, as its

[2] The [C I] luminosities can be derived from eq. 1.3.1 by substituting the CO parameters with that of [C I].

[3] Note that $M_{[CI]}$ can also be derived from the $[C\,I](^3P_2 - {}^3P_1)$ line following Weiß et al. (2003): $M_{[CI]} = 4.566 \times 10^{-3} Q(T_{ex}) \frac{1}{5} e^{(62.5\,K/T_{ex})} L'_{[CI]^3P_2-^3P_1}$. However, the dependency on T_{ex} for $[C\,I](^3P_2 - {}^3P_1)$ is reported to be stronger than for that of $[C\,I](^3P_1 - {}^3P_0)$ (Weiß, Walter & Scoville 2005).

buildup and destruction are linked to the formation of new stars and their explosion. Moreover, dust acts as a catalyst for the conversion of atomic into molecular hydrogen, which is formed on the surface of dust grains (Wolfire et al. 1995; Wakelam et al. 2017). Dust is also responsible for the heating of gas, due to electrons freed up by the photoelectric effect on dust grains in PDR (Tielens et al. 1994; Holland et al. 1999). It is thus clear that dust is an essential component of the ISM and, in general, a fundamental piece of information to understand galaxy evolution.

The bulk of the dust contributing to the dust mass is usually from relatively cold dust grains (with temperatures of $\sim 15-60\,\mathrm{K}$) that contribute to the bulk of the emission at far-IR (FIR) and submillimeter wavelengths (8-1000 µm) of the galaxy's spectral energy distribution (SED). It is well known that a significant fraction of the UV radiation from young stars, a direct measure of the instantaneous SFR, is absorbed by dust and thermally re-radiated at FIR wavelengths (Madau & Dickinson 2014). As such, the emission from dust is commonly used to probe the obscured SFR in galaxies (Kennicutt 1998; Nordon et al. 2010; Elbaz et al. 2011).

Thanks to the Multi-Band Imaging Photometer for Spitzer (MIPS: Rieke et al. 2004) instrument on the *Spitzer* Space Telescope (Werner et al. 2004), in addition to Photodetector Array Camera & Spectrometer (PACS: Poglitsch et al. (2010)) and Spectral and Photometric Imaging Receiver (SPIRE: Griffin et al. 2010) on-board the *Herschel* Space Telescope (Pilbratt et al. 2010), mid-IR (MIR) to FIR observations of large samples of galaxies have been exploited to study the dust emission in galaxies. These large surveys allowed us to quantify the relative importance of the unobscured and obscured star formation traced by the UV and IR dust emission, respectively, finding them comparable (e.g., Madau & Dickinson 2014, for a recent review).

1.4.1 *The emission from polycyclic aromatic hydrocarbons*

The pioneering work from the *Infrared Space Observatory* (ISO: Kessler et al. 1996) in the 1990s followed by the InfraRed Spectrograph (IRS: Houck et al. 2005) on *Spitzer* enabled spectroscopy studies in galaxies at MIR wavelengths, where the emission at $3-17\,\mu\mathrm{m}$ are dominated by polycyclic aromatic hydrocarbons (PAHs: Sellgren 1984; Puget & Leger 1989). These species are planar molecules composed of $\sim 10-1000$ carbon atoms, and trace the emission from very small grains (VSGs: Puget & Leger 1989; Allamandola, Tielens

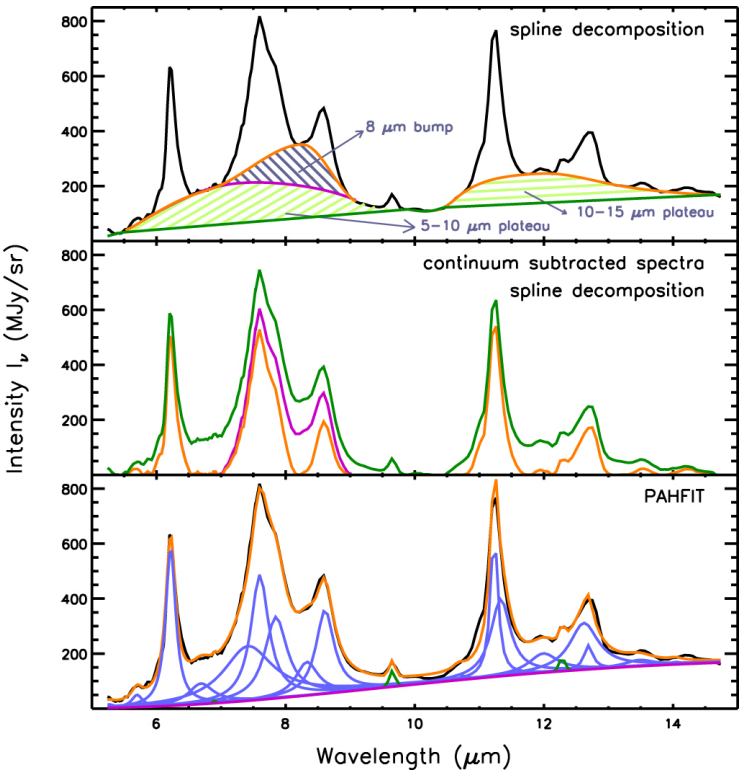

Figure 1.8: **PAHs.** Mid-infrared observations of a reflection nebula, NGC 2023, using three different continuum extraction methods including a spline (*upper*), modified spline (*middle*), and PAHFIT (Smith et al. 2007) decomposition (*lower*). Figures are from Peeters et al. (2017).

& Barker 1989; Desert, Boulanger & Puget 1990). The main PAH features arise at 3.2, 6.2, 7.7, 8.6, 11.3, and 12.7 µm (Figure 1.8), where the strength of their emission highly depends on the metallicity and radiation field intensity (Helou et al. 2001; Engelbracht et al. 2005; Engelbracht et al. 2008; Smith et al. 2007; Shivaei et al. 2017).

The PAH molecules comprise up 5% of the elemental carbon, representing a carbon reservoir similar to that of CO (Tielens 2011). They are ubiquitous in the ISM (Tielens 2008) and, together with dust, they are thought to be an important mechanism to convert the stellar radiation to thermal energy in regions with ongoing star formation via the photoelectric effect (Bakes & Tielens 1994; Helou et al. 2001). The emission from PAHs has been widely observed in the Universe, including in star-forming regions within the Milky Way (Helou et al. 2004; Calzetti et al. 2005; Churchwell et al. 2006; Rho et al. 2006; Calzetti et al. 2007; Lebouteiller et al. 2007; Povich et al. 2007;

Thilker et al. 2007), nearby ULIRGs (Genzel et al. 1998; Lutz et al. 1998; Rigopoulou et al. 1999; Armus et al. 2007; Desai et al. 2007; Pereira-Santaella et al. 2010), local SFGs, starbursts and galaxies with the presence of an AGN (Moorwood 1986; Roche et al. 1991; Laurent et al. 2000; Peeters, Spoon & Tielens 2004; Weedman et al. 2005; Houck et al. 2007; Smith et al. 2007; Spoon et al. 2007; Sales, Pastoriza & Riffel 2010; Alonso-Herrero et al. 2016; Jensen et al. 2017; Kirkpatrick et al. 2017), SFGs at intermediate redshift at $0.01 < z < 0.3$ (O'Dowd et al. 2009; Veilleux et al. 2009; Wu et al. 2010), and high-redshift galaxies at $z \sim 1 - 4$ (Valiante et al. 2007; Yan et al. 2007; Farrah et al. 2008; Sajina et al. 2008; Huang et al. 2009; Murphy et al. 2009; Fadda et al. 2010; Pope et al. 2013; Rujopakarn et al. 2013; Riechers et al. 2014).

SFR indicator: PAHs are classically assumed to be tracing ongoing star formation (Figure 1.9) as they are observed to be bright in regions including [H II] regions that are powered by young stars (e.g., Genzel et al. 1998; Calzetti et al. 2007; Lutz et al. 2007; Pope et al. 2008b; Xie & Ho 2019), where the emission from PAHs can contribute up to 20% of the total IR emission (Smith et al. 2007; Dale et al. 2009). However, several works report that the emission from PAHs instead are detected in shell-like structures surrounding the star-forming regions (Churchwell et al. 2006; Rho et al. 2006), where the strength of the PAHs decrease inside [H II] regions (e.g., Helou et al. 2004; Calzetti et al. 2005; Povich et al. 2007). Moreover, numerous observations indicate a decreasing PAH/IR luminosity ratio in (U)LIRGs and starburst galaxies (e.g., Lutz et al. 1998; Pereira-Santaella et al. 2010; Shivaei et al. 2017), which has been attributed to destruction of PAHs by the strong and intense UV radiation in [H II] regions and shocks from supernovae or re-absorption of MIR radiation (O'Halloran, Satyapal & Dudik 2006; Tielens 2008; Micelotta, Jones & Tielens 2010b; Micelotta, Jones & Tielens 2010a; Murata et al. 2017).

Effect of AGN: A similar trend of absent PAH emission is observed for AGN-dominated galaxies, where the PAH/IR luminosity ratio is lower with respect to that of SFGs. These results suggest that the PAHs have been suppressed or destroyed close to the vicinity of the AGN (Voit 1992; Lutz et al. 1998; Diamond-Stanic & Rieke 2010). However, other works report strong 11.3 µm PAH emission close to the nuclei of AGNs (Hönig et al. 2010; Esquej et al. 2014; Alonso-Herrero et al. 2016) and extended PAH emission where the

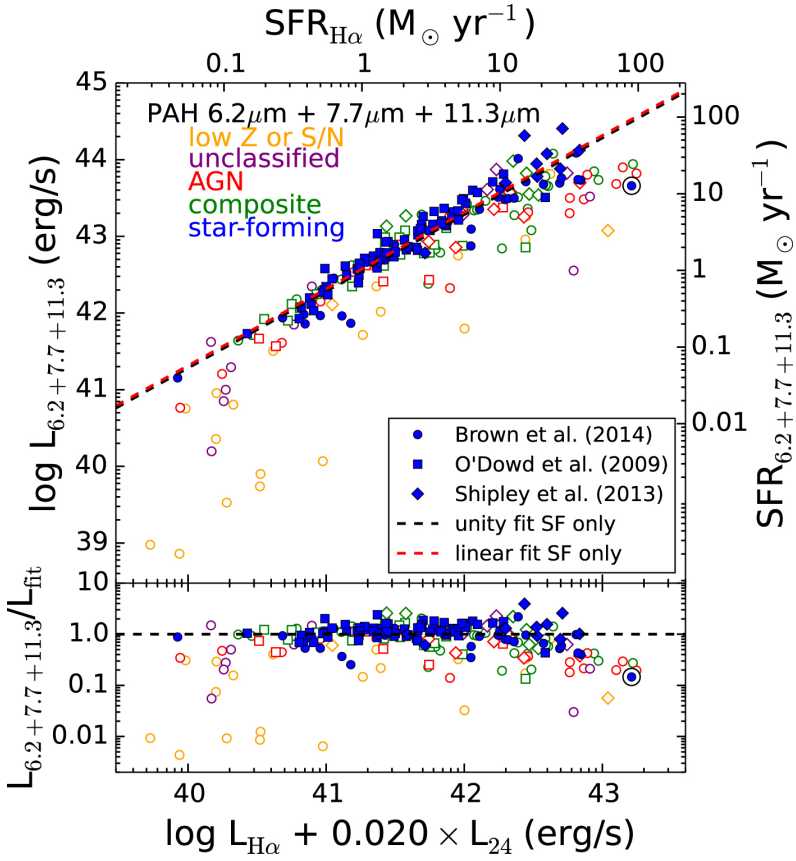

Figure 1.9: **PAH and SFR.** Total PAH luminosity as a function of Hα luminosity of galaxies at $z < 0.4$, including SFGs (filled blue), AGNs (open red), composites (SFG+AGN) (open green), unclassified (open purple), and SFGs with low metallicity or S/N (open orange). The best-fitted relation is shown as the dashed black line when only including the SFGs. Figure is from Shipley et al. (2016).

width of the PAH feature rises with increasing distance from the nucleus (Alonso-Herrero et al. 2014). These findings have been interpreted as the PAH molecules are not destroyed but instead diluted by the AGN. Interestingly Jensen et al. (2017) measured the radial emission profiles of the 11.3 µm PAH within $\sim 10 - 500$ pc of the nucleus and suggested that the AGN itself may excite the PAHs close to the nucleus. Furthermore, the smaller equivalent width of the 6.2 µm PAH feature observed in AGN-dominated galaxies has been used as a useful tool to determine the contamination from the AGN to the MIR+IR emission (e.g., Smith et al. 2007; Sales, Pastoriza & Riffel 2010).

Metallicity: A key parameter that can explain the observed PAH deficit in ULIRGs and starbursts is metallicity. Several studies have observed a deficiency of PAHs in low-metallicity galaxies (Engelbracht et al. 2005; Madden et al. 2006; O'Halloran, Satyapal & Dudik 2006; Hunt et al. 2010). For a sample of SFGs at $z < 0.4$, Shipley et al. (2016) report that the PAH intensity depends on the galaxy gas-phase metallicity and propose that PAHs are not as effectively formed in low-metallicity environments as fewer carbon atoms are available in the ISM. Sandstrom et al. (2012) argue that the suppression of the PAH emission observed in the Small Magellanic Cloud (SMC) may be due to their ISM conditions: the low abundance of carbon available in the ISM might be inefficient in forming large PAHs resulting in a smaller average size distribution of PAH molecules when compared to environments with higher metallicities. When the PAHs pass through the diffuse ISM they are exposed to radiation from UV photons, cosmic rays, and shocks, in which a fraction of the PAHs will be destroyed. Theoretical models predict that small PAH molecules (< 50 carbon atoms) are rapidly destroyed by all typical ISM processes, whereas larger PAHs survive as they are less fragile (Allain, Leach & Sedlmayr 1996; Le Page, Snow & Bierbaum 2003). If the PAHs, when formed, are smaller than the average PAH molecule in a high-metallicity galaxy, the observed PAH deficit may be caused by rather average conditions of the ISM and not only by the extreme radiation fields as seen in local ULIRGs and starburst galaxies.

Gas connection: Since the 1970s, the connection between H_2 and dust has been well established as the formation of H_2 is thought to take place on the surface of dust grains (e.g., Hollenbach & Salpeter 1971; Wakelam et al. 2017, see above). Recent works suggest the H_2 formation on PAHs can be as effective as on dust grains in PDRs based on simulations (Castellanos et al. 2018a; Castellanos et al. 2018b). Moreover, several studies report empirical evidence for a correlation between the emission from PAHs and CO, including similar radial profiles (Regan et al. 2006) and coincident spatial emission between PAHs and CO in local star-forming galaxies (Sandstrom et al. 2010; Schinnerer et al. 2013; Schinnerer et al. 2017, see also Figure 1.10), and observed CO–PAH luminosity correlations on galaxy-integrated scales for nearby and distant galaxies (Tan et al. 2013; Pope et al. 2013). Moreover, PAHs have been reported to spatially correlate with the cold dust emission

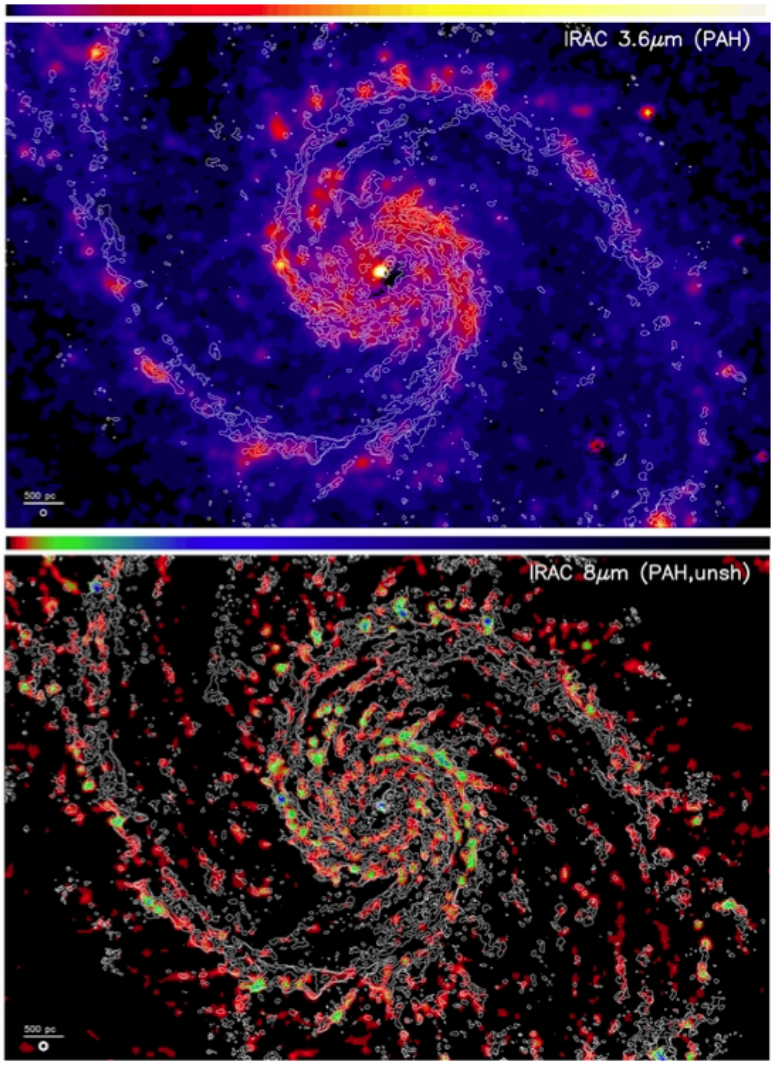

Figure 1.10: **PAH and CO in M51:** 3.3 µm PAH emission (*upper*) and emission at 8 µm (*lower*), where CO(1 – 0) intensity distribution is shown as white contours. Figures are modified from Schinnerer et al. (2013).

at rest-frame $\geq 160\,\mu$m and up to submillimeter wavelengths (Haas, Klaas & Bianchi 2002; Bendo et al. 2008; Jones et al. 2015). All these observed trends suggest that PAHs are closely linked to the cold ISM in galaxies.

1.4.2 *The far-infrared properties of galaxies*

Several physical properties of the dust in galaxies, including its mass ($M_{\rm d}$), temperature ($T_{\rm d}$), the infrared luminosity ($L_{\rm IR}$), and the intensity of the radiation field ($\langle {\rm U} \rangle$), can be estimated by fitting the observed SED at far-IR to sub-mm wavelengths, where the thermalized dust emits a blackbody spectrum in first approximation. There are several approaches to model the FIR SED of galaxies (for a recent review see Casey, Narayanan & Cooray 2014). In this thesis, two commonly used methods will be presented; modified blackbody (MBB) prescriptions and physically motivated dust models.

MBB prescription: A common way to derive the $M_{\rm d}$ is by fitting the SED with a single-temperature modified blackbody prescription (Blain, Barnard & Chapman 2003; Casey, Narayanan & Cooray 2014):

$$S_\nu = \epsilon_\nu B_\nu(T_{\rm d})\,, \tag{1.6}$$

where S_ν is the flux density at frequency ν, ϵ_ν is the emissivity coefficient and $B_\nu(T_{\rm d})$ is the Planck function with the luminosity-weighted dust temperature $T_{\rm d}$. The Planck function is defined as:

$$B_\nu(T_{\rm d}) = \frac{2h}{c^2}\frac{\nu^3}{{\rm e}^{(h\nu/k_{\rm B}T_{\rm d})}-1}\,, \tag{1.7}$$

where h and $k_{\rm B}$ are the Planck and Boltzmann's constants, respectively. The emissivity coefficient can be expressed as $\epsilon_\nu = (1-\exp(-\tau_\nu))$ (Benford et al. 1999; Omont et al. 2001; Berta et al. 2016). The optical depth is defined as $\tau_\nu = \kappa_\nu \Sigma_{\rm dust}$, where $\kappa_\nu = \kappa_0(\nu/\nu_0)^\beta$ is the dust mass absorption coefficient, $\Sigma_{\rm dust}$ is the dust surface density, and β is the spectral emissivity index (typically in the range of $1.5-2$). τ_ν can thus also be expressed as: $\tau_\nu = \tau_0(\nu/\nu_0)^\beta$, where ν_0 is the frequency at which $\tau_{\nu_0}=1$. In the optically thin case, $\epsilon_\nu \sim \nu^\beta$, and the MBB prescription is thus reduced to:

$$S_\nu \propto \nu^\beta B_\nu(T_{\rm d})\,. \tag{1.8}$$

The dust mass can then be derived from the best-fitted model:

$$M_{\rm d,MBB} = \frac{S_\nu D_L^2}{(1+z)\kappa_\nu B_\nu(T_{\rm d})}\,. \tag{1.9}$$

The $L_{\rm IR}$ is commonly estimated as the integrated emission at $8-1000\,\mu$m:

$$L_{\rm IR} = 4\pi\, D_L^2 \int_{8\,\mu{\rm m}}^{1000\,\mu{\rm m}} S_\nu\, d\nu\ . \tag{1.10}$$

Although the dust temperature determines the frequency of the SED peak, several degeneracies exist between the parameters including the luminosity-weighted $T_{\rm d}$ and ν_0 (the frequency at which the dust emission in a galaxy becomes optically thick), in addition to $T_{\rm d}$ and β, as the peak of the FIR SED is proportional to $\beta/T_{\rm d}$ (e.g., Blain, Barnard & Chapman 2003; Casey, Narayanan & Cooray 2014; Lutz 2014; Magnelli et al. 2014; Berta et al. 2016). For galaxies in which the sampling of the FIR SED is sparse, it is common practice to adopt an optically thin rather than a general opacity MBB prescription, as the fit parameters are otherwise unconstrained.

Draine and Li (2007) dust models: Another common approach to determine the FIR properties of galaxies is to use physically motivated dust models. Some of the most widespread and commonly used templates are provided in Draine & Li (2007, hereafter DL07). These models describe the interstellar dust as a mixture of carbonaceous and amorphous silicate grains where the size distributions correspond to the observed extinction law in the Milky Way, Large Magellanic Cloud, and Small Magellanic Cloud bar region. The PAH abundance is characterized by the PAH index ($q_{\rm PAH}$), which is the fraction of dust mass in the form of PAH molecules. The models assume that the dust is optically thin and include two components: a diffuse ISM that is heated by radiation field with constant intensity ($U_{\rm min}$=$U_{\rm max}$), and dust enclosed in photo-dissociation regions (PDRs), exposed to starlight within an intensity range ($U_{\rm min}$ to $U_{\rm max}$). The amount of dust exposed to radiation intensities from U to $U+dU$ for the two components is:

$$\frac{dM_{\rm d}}{dU} = (1-\gamma)\,\delta(U-U_{\rm min}) + \gamma M_{\rm d}\frac{\alpha-1}{U_{\rm min}^{(1-\alpha)} - U_{\rm max}^{(1-\alpha)}} U^{-\alpha}\ , \tag{1.11}$$

where α is the effective radius of the grains and γ is the fraction of dust in the PDRs to the total amount of dust. For $\alpha \neq 1$, δ is the delta function representing the diffuse interstellar radiation field of intensity $U = U_{\rm min} = U_{\rm max}$. The emission spectrum is a linear combination of a stellar component assumed to be a blackbody with a color temperature of $T = 5000\,$K, a dust component heated by a radiation field of $U_{\rm min}$ in the diffuse ISM, and a second

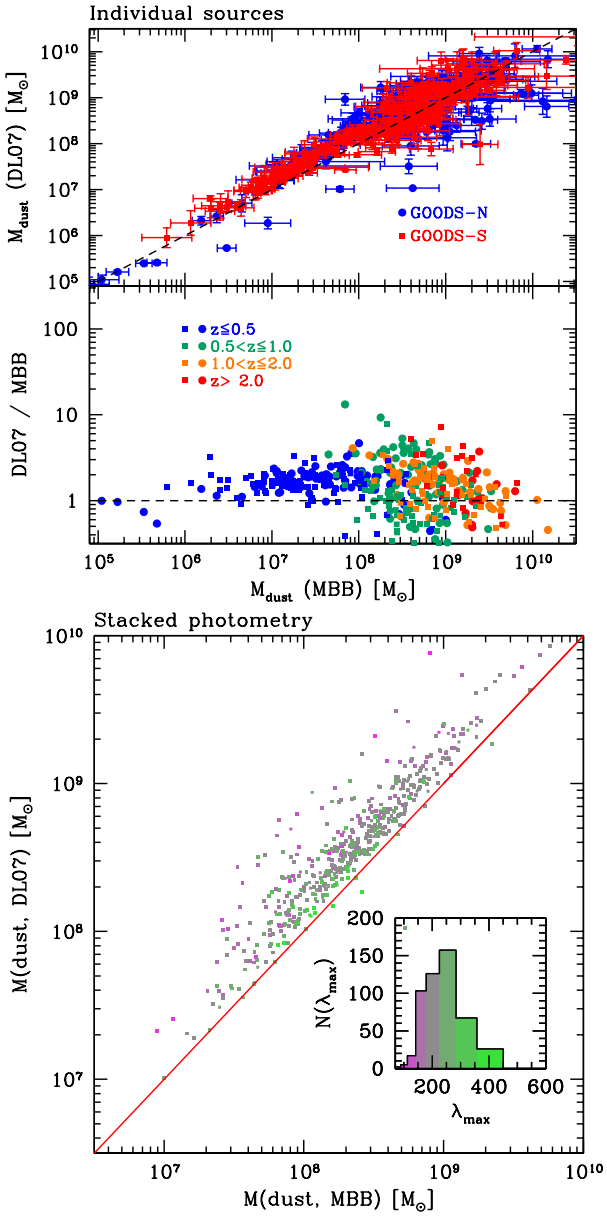

Figure 1.11: $M_{\rm d}$ **from MBB and DL07.** *Upper panel (1)*: Comparison between the dust mass derived from MBB prescriptions (adopting $\beta = 2.08$ and $\lambda \geq 50\,\mu$m) and DL07 models for galaxies from GOODS-N (blue) and GOODS-S (red). *Upper panel (2)*: The ratio of the inferred $M_{\rm d}$ from MBB and DL07 prescriptions as a function of MBB-derived $M_{\rm d}$ for galaxies at $z \leq 0.5$ (blue), $0.5 < z \leq 1.0$ (green), $1.0 < z \leq 2.0$ (orange), and $z > 2.0$ (red). *Lower*: Comparison for stacked sources from Magnelli et al. (2014), where galaxies are color coded based on the maximum available rest-frame wavelength. Figures are from Berta et al. (2016).

portion heated by a power-law distribution of starlight in PDRs. At a distance D, the emission spectrum of a galaxy can be described as:

$$F_{\nu,\mathrm{model}} = \Omega_{\star} B_{\nu}(T) + \frac{M}{4\pi D^2}\Bigg[(1-\gamma)\, p^0_{\nu}(q_{\mathrm{PAH}}, U_{\mathrm{min}}) + \gamma p_{\nu}(q_{\mathrm{PAH}}, U_{\mathrm{min}}, U_{\mathrm{max}}, \alpha)\Bigg], \tag{1.12}$$

where $\Omega_{\star}$ is the solid angle subtended by stars, and $p^0_{\nu}(q_{\mathrm{PAH}}, U_{\mathrm{min}})$ and $p_{\nu}(q_{\mathrm{PAH}}, U_{\mathrm{min}}, U_{\mathrm{max}}, \alpha)$ are the emitted power per unit frequency per unit dust mass for dust heated by a radiation intensity of U_{min}, and a power-law distribution with intensities $dM/dU \propto U^{-\alpha}$ ranging from U_{min} to U_{max}, respectively. Following Draine & Li (2007), small variations are found for α and U_{max} which can be fixed to $\alpha = 2$ and $U_{\mathrm{max}} = 10^6$. The dust mass is derived assuming:

$$M_{\mathrm{d,DL07}} = \left(\frac{M_{\mathrm{d}}}{M_{\mathrm{H}}}\right) m_{\mathrm{H}} \frac{L_{\nu}}{4\pi j_{\nu}}, \tag{1.13}$$

where $j_{\nu} = (M_{\mathrm{d}}/M_{\mathrm{H}})\, m_{\mathrm{H}}\, (p_{\nu}/4\pi)$ is the emissivity per hydrogen nucleon, m_{H} is the mass of the hydrogen nucleon, and L_{ν} is the luminosity at frequency ν. The mean intensity of the radiation field due to starlight ($\langle U \rangle$) can then be determined from the best-fitted model as (Magdis et al. 2012b):

$$\langle U \rangle = \frac{L_{\mathrm{d}}}{P_0 M_{\mathrm{d}}} \quad \text{for } \alpha \neq 2 \tag{1.14}$$

where P_0 is the power absorbed in a radiation field with $U = 1$. The mean radiation field can be expressed as $\langle U \rangle \propto L_{\mathrm{IR}}/M_{\mathrm{d}}$ (e.g., Magdis et al. 2012b), and is related to the mass-weighted dust temperature as: $\langle U \rangle = (T'_{\mathrm{d}}/18.9)^{6.04}$ (Magdis et al. 2012b; Magdis et al. 2017). The relation between the mass- and luminosity-weighted temperature have been reported to be: $T'_{\mathrm{d}} = 0.91 \times T_{\mathrm{d}}$ (Schreiber et al. 2018).

Comparison between MBB and DL07: Several studies report systematically lower M_{d} derived from MBB prescriptions than that of the DL07 models by a factor of $\sim 1.5 - 3\times$ for both local galaxies (Dale & Helou 2002) and star-forming galaxies at $0.5 < z < 2$ (Magdis et al. 2012b), $z > 1$ (Magnelli et al. 2012b), $z \sim 0.15$ (Magdis et al. 2013), and $z < 2.5$ (Berta et al. 2016). An example of such a study reporting a discrepancy between the MBB- and DL07-derived M_{d} is shown in Figure 1.11. The suggested effects contributing

to the difference in the dust mass estimates include the underlying single-temperature MBB model assumptions, the adopted κ_ν, and β (if fixed), which can change M_d by a factor of $\sim 3-5\times$ (Berta et al. 2016).

Evolution of T_d and $\langle U \rangle$ with redshift: For normal star-forming galaxies, several studies have reported an increase of the dust temperature (or mean intensity of the radiation field) with redshift when adopting either optically thin MBB or DL07 models (Magnelli et al. 2014; Béthermin et al. 2015; Magdis et al. 2017; Schreiber et al. 2018; Jin et al. 2019). As an example, Schreiber et al. (2018) report the following relation for MS galaxies at $z = 0-4$:

$$T_\mathrm{d}^{\prime\,\mathrm{MS}} = (32.9 \pm 2.4) + (4.60 \pm 0.35) \times (z-2)\,, \tag{1.15}$$

where the authors use Wien's law for the elementary SED templates, which is then weighted by the associated dust mass. This SED-fitting procedure is consistent with the optically thin MBB (Schreiber et al. 2018), and in agreement with previous findings (e.g., Béthermin et al. 2015). Moreover, a rising $T_\mathrm{d}^\prime$ is reported to exist with increasing distance from the MS (Magnelli et al. 2014; Schreiber et al. 2018). Assuming that the $T_\mathrm{d}^\prime - \mathrm{SFR/SFR_{MS}}$ relation is independent of redshift, then the mass-weighted dust temperature has been reported to evolve with redshift as (e.g., Schreiber et al. 2018):

$$T_\mathrm{d}^\prime = T_\mathrm{d}^{\prime\,\mathrm{MS}} - (0.77 \pm 0.04) + (10.1 \pm 0.6) \times \log_{10}(\mathrm{SFR/SFR_{MS}})\,, \tag{1.16}$$

suggesting that starburst galaxies at any redshift have warmer dust temperatures than that of MS galaxies. On the other hand, no $\langle U \rangle$ (hence $T_\mathrm{d}^\prime$) evolution is reported for starburst galaxies lying well above the MS ($\mathrm{SFR/SFR_{MS}} > 10$ Béthermin et al. 2015), where the mean radiation field of SB galaxies are reported to be lower than that of the MS galaxies at $z > 2.5$. However, as several works imply that the dust emission in starburst galaxies may be optically thick out to rest-frame $\lambda_0 = 100-200\,\mu\mathrm{m}$ (Blain, Barnard & Chapman 2003; Huang & Kauffmann 2014; Lutz 2014; Lutz et al. 2016; Spilker et al. 2016; Riechers et al. 2013; Hodge et al. 2016; Simpson et al. 2017), the lack of a $T_\mathrm{d}^\prime$ or $\langle U \rangle$ evolution can arise due to the assumption of optically thin dust emission.

1.5 THESIS OUTLINE

In the previous sections, a concise, but informative, description of the current status of the investigation of the galaxy formation and evolution from a

standpoint of their ISM content and properties was presented. The main focus of this thesis is the characterization of the ISM properties and quantity in nearby and distant galaxies, by exploiting the wealth of information enclosed in the multiple gas and dust tracers described in the above sections, spanning the mid-infrared to sub-millimeter and radio wavelengths. The following two chapters enclose an article and a letter appeared in peer-reviewed journals in the past years and months.

In Chapter 2, I will present a comparison of the emission from PAHs with common tracers of the SFR and the molecular gas in star-forming galaxies, including the CO and sub-mm emission and total IR luminosity. I will include new IRAM 30m single-dish CO(1 – 0) observations of star-forming galaxies at $0.01 < z < 0.30$ with well-detected PAH emission based on existing *Spitzer* IRS spectra. Complementing this sample with existing literature studies, I will examine the scaling relations between the emission from the 6.2 and 7.7 µm PAH features and CO emission for main-sequence and starburst galaxies at the redshifts probed so far. Moreover, trends between the PAHs and dust emission at different IR wavelengths will be explored. I will present how PAHs can be used as a molecular gas (rather than SFR) tracer, and its implications for future studies with the *James Webb Space Telescope* (*JWST*). This will bring together and simultaneously analyze most of the ISM tracers described above, and more in the immediate future (see below).

In Chapter 3, I will shift the focus on the dust properties of distant galaxies and how modeling and assumptions can deeply affect the physical conclusions we draw from observations. In particular, I will revisit one of the brightest and most distant starburst galaxies in the GOODS-N field, GN20 at $z = 4.055$. This prototypical starburst galaxy displays a surprisingly low dust temperature when derived assuming optically thin dust prescriptions, which is similar to that of main-sequence galaxies at $z \sim 1.4$. On the other hand, a general opacity model favors a larger dust temperature and suggests that the dust emission is optically thick up to FIR wavelengths. Assuming the typically adopted optically thin assumption would drive us to the conclusion that such an extreme system is colder than an average main-sequence galaxy at $z \sim 1.4$, and to unphysically high dust-to-stellar mass ratios, that are incompatible with the current limits on the history of dust production in galaxies. Intriguingly, these

inconsistencies are greatly alleviated, if not removed, when using the general opacity model. However, as high-redshift galaxies typically lack sufficient photometric coverage at these wavelengths compared to that of local galaxies, the optically thin and thick dust solutions in such cases become degenerate. In an attempt to overcome this issue, I will investigate a recent reported correlation between the dust temperature and the excitation temperature derived from [C I]. I will report novel NOEMA observations and detections of both the [C I] line transitions in GN20, and show how the derived gas temperature can potentially help distinguishing between an optically thin or thick dust solution.

Finally, Chapter 4 briefly describes future developments based on these two works. In this Chapter, I will also present the introduction and main motivation, in addition to the preliminary analysis, of a parallel project about the radio emission in massive quiescent galaxies at $z \sim 2$.

CHAPTER 2

A new molecular gas tracer for star-forming galaxies

This chapter contains the following article:
"PAHs as tracers of the molecular gas in star-forming galaxies"

Published in the Monthly Notices of Royal Astronomy (MNRAS): Vol. 482, pp. 1618–1633, 2019.

Authors: Isabella Cortzen, John Garrett, Georgios E. Magdis, Dimitra Rigopoulou, Francesco Valentino, Miguel Pereira-Santaella, Francoise Combes, Almudena Alonso-Herrero, Sune Toft, Emanuele Daddi, David Elbaz, Carlos Gómez-Guijarro, Mikkel Stockmann, Jiasheng Huang & Carsten Kramer.

ABSTRACT

We combine new CO(1 – 0) line observations of 24 intermediate redshift galaxies ($0.03 < z < 0.28$) along with literature data of galaxies at $0 < z < 4$ to explore scaling relations between the dust and gas content using polycyclic aromatic hydrocarbon (PAH) 6.2 µm ($L_{6.2}$), CO ($L'_{\rm CO}$), and infrared ($L_{\rm IR}$) luminosities for a wide range of redshifts and physical environments. Our analysis confirms the existence of a universal $L_{6.2}$–$L'_{\rm CO}$ correlation followed by normal star-forming galaxies (SFGs) and starbursts (SBs) at all redshifts. This relation is also followed by local ultraluminous infrared galaxies that appear as outliers in the $L_{6.2}$–$L_{\rm IR}$ and $L_{\rm IR}$–$L'_{\rm CO}$ relations defined by normal SFGs. The emerging tight ($\sigma \approx 0.26$ dex) and linear ($\alpha = 1.03$) relation between $L_{6.2}$ and $L'_{\rm CO}$ indicates a $L_{6.2}$ to molecular gas ($M_{\rm H_2}$) conversion factor of $\alpha_{6.2} = M_{\rm H_2}/L_{6.2} = (2.7 \pm 1.3) \times \alpha_{\rm CO}$, where $\alpha_{\rm CO}$ is the $L'_{\rm CO}$ to $M_{\rm H_2}$ conversion factor. We also find that on galaxy integrated scales, PAH emission is better correlated with cold rather than with warm dust emission, suggesting that PAHs are associated with the diffuse cold dust, which is another proxy for $M_{\rm H_2}$. Focusing on normal SFGs among our sample, we employ the dust continuum emission to derive $M_{\rm H_2}$ estimates and find a constant $M_{\rm H_2}/L_{6.2}$ ratio of $\alpha_{6.2} = 12.3\ {\rm M_\odot/L_\odot}$ ($\sigma \approx 0.3$ dex). This ratio is in excellent agreement with the $L'_{\rm CO}$-based $M_{\rm H_2}/L_{6.2}$ values for $\alpha_{\rm CO} = 4.5\ {\rm M_\odot\,(K\,km\,s^{-1}\,pc^2)^{-1}}$ which is typical of normal SFGs. We propose that the presented $L_{6.2}$–$L'_{\rm CO}$ and $L_{6.2}$–$M_{\rm H_2}$ relations will serve as useful tools for the determination of the physical properties of high-z SFGs, for which PAH emission will be routinely detected by the *James Webb Space Telescope*.

2.1 INTRODUCTION

The mid-infrared (MIR; 3–25 µm) spectrum of star-forming galaxies (SFGs) is dominated by strong emission features generally attributed to polycyclic aromatic hydrocarbons (PAHs) (Sellgren 1984; Puget & Leger 1989; Helou et al. 2001; Pahre et al. 2004; Tielens 2008). The extensive observations of PAH emission in galaxies at both low and high redshifts from either the *Infrared Space Observatory* (Genzel et al. 1998; Lutz et al. 1998; Rigopoulou et al. 1999) or the InfraRed Spectrograph (IRS) on the *Spitzer Space Telescope* (Armus et al. 2007; Houck et al. 2007; Spoon et al. 2007; Valiante et al. 2007; Yan et al. 2007; Farrah et al. 2008; Sajina et al. 2008; Murphy et al. 2009;

O'Dowd et al. 2009; Veilleux et al. 2009; Fadda et al. 2010; Pereira-Santaella et al. 2010; Riechers et al. 2014) indicate that they are ubiquitous and an important tracer of the interstellar medium (ISM). PAH molecules, which are stochastically heated by optical and UV photons, dominate the photoelectric heating rates of the neutral gas and the ionization balance within molecular clouds (Bakes & Tielens 1994). The emission arising from these abundant species can contribute up to 20 per cent of the total infrared (IR) emission in galaxies depending on the physical conditions (Smith et al. 2007; Dale et al. 2009). Hard UV photon fields are thought to destroy, fragment or ionize the PAH molecules (Boulanger et al. 1988; Boulanger et al. 1990; Helou, Ryter & Soifer 1991; Pety et al. 2005), whereas low-metallicity systems reveal suppressed PAH emission (Engelbracht et al. 2005; Hunt et al. 2010). The origin of PAHs has been widely discussed in previous studies suggesting that they can be formed in either the envelopes or outflows of carbon-rich AGB stars (Latter 1991; Cherchneff, Barker & Tielens 1992), massive red supergiants (Melbourne & Boyer 2013) or in the ISM itself (Tielens et al. 1987; Puget & Leger 1989; Herbst 1991; Sandstrom et al. 2010; Sandstrom et al. 2012; Sandstrom et al. 2013).

In the local Universe, PAH emission and its link to star formation has been thoroughly studied within the Milky Way and in nearby galaxies through various star formation tracers: individual observations of [H II] regions revealed that the PAH emission is found in shell-like structures around the star-forming regions (Churchwell et al. 2006; Rho et al. 2006), with a notable decrease of their strength within the [H II] regions (Helou et al. 2004; Calzetti et al. 2005; Calzetti et al. 2007; Lebouteiller et al. 2007; Povich et al. 2007; Thilker et al. 2007). On larger scales, previous studies have found that SFGs at both low and high redshifts follow a linear relation between the integrated luminosity of the PAH 6.2 μm feature ($L_{6.2}$) and the total infrared luminosity ($L_{\rm IR}$), where the latter is the sum of the re-radiated emission from dust grains and a commonly used tracer for the star formation rate (SFR) (Schmidt 1959; Kennicutt 1998; Roussel et al. 2001; Förster Schreiber et al. 2004; Armus et al. 2007; Huang et al. 2009; Menéndez-Delmestre et al. 2009; Rujopakarn et al. 2013). PAH emission has also been observed in both ultra-luminous infrared galaxies (ULIRGs: $L_{\rm IR} > 10^{12}$ L$_\odot$) (Genzel et al. 1998; Armus et al. 2007; Desai et al. 2007) and galaxies with the presence of an active galactic nucleus (AGN) (Moorwood 1986; Roche et al. 1991; Weedman et al. 2005; Smith et al.

2007; Alonso-Herrero et al. 2016; Kirkpatrick et al. 2017; Jensen et al. 2017), however with an on average smaller PAH equivalent. As such the equivalent width of the PAH features can be used to distinguish between AGN and/or strong starbursting galaxies from normal, star-formation dominated systems (Laurent et al. 2000; Brandl et al. 2006; Sajina et al. 2007; Spoon et al. 2007; Pope et al. 2008a; Shipley et al. 2013; Esquej et al. 2014). For AGN-dominated galaxies, the total IR emission may also arise from dust heated by the AGN rather than star formation activity, especially in wavelengths shorter than the peak of the FIR SED (e.g., Smith et al. 2007; Wu et al. 2010; Shipley et al. 2013; Mullaney et al. 2013). Lower $L_{\rm PAH}/L_{\rm IR}$ ratios have previously been observed in AGN-dominated sources with respect to SFGs (Armus et al. 2007; Sajina et al. 2008; Valiante et al. 2007) suggesting that PAHs at 6.2, 7.7, and 8.6 μm are suppressed due to the presence of an AGN (Diamond-Stanic & Rieke 2010). Interestingly though, recent works in the local Universe report strong PAH 11.3 μm emission from the nuclear regions of Seyfert galaxies and QSOs (Hönig et al. 2010; Alonso-Herrero et al. 2014; Esquej et al. 2014; Alonso-Herrero et al. 2016), indicating that PAH molecules could be excited, rather than destroyed, by the AGN itself (Jensen et al. 2017).

A similar trend to $L_{\rm PAH}$–$L_{\rm IR}$ has been observed between the luminosity of the CO(1 – 0) transition line ($L'_{\rm CO}$), a common tracer of molecular gas, and the $L_{\rm IR}$. The majority of SFGs follow a tight relation between the SFR (traced by $L_{\rm IR}$) and the cold molecular gas (traced by $L'_{\rm CO}$) or the total gas content ($M_{\rm gas}$), which is known as the Kennicutt–Schmidt (KS) law spanning a large dynamical range (Schmidt 1959; Kennicutt 1998). Similar to the $L_{\rm IR}$–$L_{6.2}$ relation starbursting systems also appear as outliers in $L_{\rm IR}$–$L'_{\rm CO}$ relation, exhibiting an enhanced star formation efficiency (SFE=$L_{\rm IR}/L'_{\rm CO}$) possibly driven by a major merger event, as supported by observations of local ULIRGs and a fraction of submillimeter galaxies (SMGs) at high redshift (Rigopoulou et al. 1999; Pope et al. 2013). The weaker PAH and CO emission (for a fixed $L_{\rm IR}$) in these star formation dominated galaxies can be explained by compact star forming regions and high SFEs due to a larger fraction of dense molecular gas (Tacconi et al. 2008; Daddi et al. 2010a; Daddi et al. 2010b; Díaz-Santos et al. 2011; Pope et al. 2013; Kirkpatrick et al. 2014). To this direction, Elbaz et al. (2011) found that the IR8=$L_{\rm IR}/L_8$[1] ratio can be used to separate normal

[1] L_8 is the monochromatic luminosity at rest-frame 8 μm as traced by the IRAC 8.0 μm band, which covers both the PAH 6.2, 7.7, and 8.6 μm complex at low redshift.

SFGs with extended star-formation activity that also lay predominantly on the so-called "main-sequence" (MS) of galaxies (Elbaz et al. 2007; Magdis et al. 2010; Schreiber et al. 2015) from compact starbursts (SBs). Also, for star-formation dominated galaxies, Magdis et al. (2013) reported that IR8 variations are driven mainly by the strength of the PAH features rather than continuum variations, again indicative of more compact star formation for sources with weaker PAH features.

Finally, several studies have revealed a connection between PAHs and the molecular gas ($M_{\mathrm{H_2}}$) as traced by CO emission. Analyses of the observed radial profiles of PAH and CO emission in local galaxies indicate that PAHs can be used as a proxy for the molecular ISM in galaxies (Regan et al. 2006). The link between PAHs and molecular gas is further supported not only by the observed correlations between PAHs and CO emission on galaxy integrated scales (Pope et al. 2013), but also between between PAHs and cold dust emission at $\geqslant 160$ μm (e.g.. Haas, Klaas & Bianchi 2002; Bendo et al. 2008; Jones et al. 2015).

In this work, we further explore the connection between the PAHs and the molecular gas of galaxies, with new single-dish CO(1 – 0) line observations of 34 IR-bright PAH-emitting SFGs across the MS selected from the 5MUSES survey (Wu et al. 2010), increasing the existing sample of PAH-, IR-, and CO-detected galaxies at intermediate redshifts ($0.03 < z < 0.28$) by a factor of 2.4 (Section 2.2). We complement our sample with existing CO(1 – 0) and PAH observations from the literature in order to determine the scatter of the scaling relations between IR, PAH, and CO data spanning two orders of magnitude in luminosity and covering a broad range of redshifts ($0 < z < 4$). In Section 2.3.1, we present the $L_{6.2}$–L_{IR} for normal SFGs and identify local ULIRGs and high-z SBs as clear outliers characterised by lower $L_{6.2}/L_{\mathrm{IR}}$ ratios. In section 2.3.2, we show that these outliers also exhibit lower $L'_{\mathrm{CO}}/L_{\mathrm{IR}}$ ratios compared to the L'_{CO}–L_{IR} relation defined by the general population of normal galaxies. On the other hand, in Section 2.3.3 we present a universal $L_{6.2}$–L'_{CO} relation followed by both normal SFGs and SBs at all redshifts. This, along with the strong correlation between the PAH and cold dust emission ($\lambda \geqslant 160$ μm) presented in Section 2.3.4, motivates us to explore PAHs as a proxy for the molecular gas in Section 2.3.5.

Throughout this paper we adopt a standard cosmology with $H_0 = 70$ $\mathrm{km\,s^{-1}\,Mpc^{-1}}$, $\Omega_{\mathrm{M}} = 0.30$, and $\Omega_{\Lambda} = 0.70$.

2.2 DATA SAMPLE

We have selected 34 star-forming targets from the 5 mJy Unbiased *Spitzer* Extragalactic Survey (5MUSES; Wu et al. 2010), in order to examine the gas and ISM properties of star-formation dominated galaxies at intermediate redshift ($0.03 < z < 0.28$) by detecting CO(1 – 0) emission and using existing observations. 5MUSES is a 24 µm flux-limited ($f_{24\mu m} > 5$ mJy) spectroscopic survey with *Spitzer* IRS, containing 330 galaxies with $L_{IR} \sim 10^{10} - 10^{12}$ $L_{\odot}$ located in the SWIRE (Lonsdale et al. 2003) and Extragalactic First Look Survey (XFLS) fields (Fadda et al. 2006). The sample fills out the gap between local SFGs (Kennicutt et al. 2003; Smith et al. 2007; Dale et al. 2009), low-z ULIRGs (Armus et al. 2007; Desai et al. 2007; Veilleux et al. 2009), and more distant galaxies with available spectroscopy data (Houck et al. 2005; Yan et al. 2007). In addition, the full sample has *Spitzer* Infrared Array Camera observations (IRAC; Fazio et al. 2004) at 3.6 – 8 µm and Multiband Imaging Photometer (MIPS; Rieke et al. 2004) at 70 – 160 µm (Wu et al. 2010), where 90% and 54% of the galaxies are detected at 70 and 160 µm, respectively.

From the 5MUSES sample, 280 galaxies have spectroscopically confirmed redshifts with low-resolution ($R = 64 - 128$) MIR spectra which were collected using the short-low (SL: 5.5 – 14.5 µm) and long-low (LL: 14 – 35 µm) spectral modules of the *Spitzer* InfraRed Spectrograph (Houck et al. 2004, IRS) as described in Wu et al. (2010). In addition to *Spitzer* IRAC, MIPS, and IRS observations, a subsample of 188 galaxies (with spectroscopically confirmed redshifts) have FIR photometric coverage at 250, 350, and 500 µm obtained with the *Herschel Space Observatory* (Griffin et al. 2010) through SPIRE observations as part of the *Herschel* Multi-tiered Extragalactic Survey (HerMES; Oliver et al. 2010; Oliver et al. 2012). Out of the 188 sources, a flux density limit of $S_{\nu} > 15$ mJy in the *Herschel* SPIRE bands yields a detection for 154 (82 per cent), 108 (57 per cent), and 50 (27 per cent) sources at 250 µm, 350 µm and 500 µm, respectively (Magdis et al. 2013). Stellar masses of the full 5MUSES sample have been estimated by Shi et al. (2011) using the Bruzual & Charlot (2003) population synthesis model to fit optical and IR photometry assuming a Chabrier (2003) IMF.

In Figure 2.1, we present the equivalent width of the PAH 6.2 µm ($EW_{6.2}$) versus distance from the MS for the full 5MUSES sample. The offset from the MS, $SFR/SFR_{MS}(z, M_*)$, is determined by adopting equation 9 in Schreiber et al. (2015) after converting our stellar masses from a Chabrier (2003) IMF

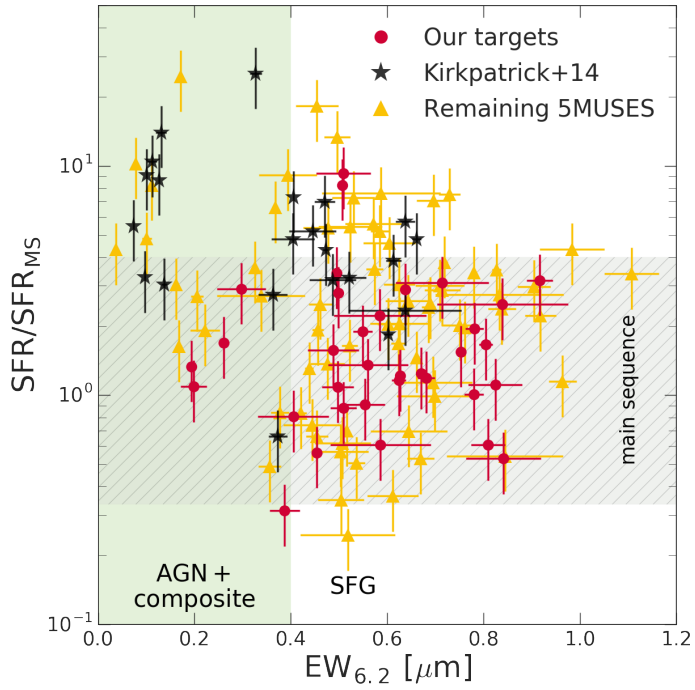

Figure 2.1: The equivalent width of the PAH 6.2 µm feature ($EW_{6.2}$) versus offset from the MS (grey shaded region). Red points depict galaxies selected for CO(1−0) line observations presented in this study. Previously CO-detected 5MUSES galaxies from Kirkpatrick et al. (2014) are shown in black, whereas the rest of the 5MUSES sources are shown in yellow. Galaxies with $EW_{6.2} \leq 0.4$ µm are classified as AGN-dominated or composite sources (green region).

to a Salpeter (1955) IMF using $M_*^S = 1.70 \times M_*^C$ (Speagle et al. 2014). SFRs are derived using L_{IR} estimates (Section 2.2.3). We use optical spectroscopy and/or the $EW_{6.2}$ to identify AGN-dominated sources in the sample. In the absence of optical spectroscopy, we classify sources with $EW_{6.2} \leq 0.4$ µm as AGN and composite sources (see Wu et al. 2010; Magdis et al. 2013, for a detailed AGN characterization of the 5MUSES sample). Since we aim at examining the ISM properties of normal galaxies at intermediate redshifts, we primarily selected targets with $EW_{6.2} > 0.4$ µm across the MS ($SFR/SFR_{MS} < 4$) for follow-up CO(1 − 0) line observations. Moreover, all of our targets have *Spitzer* and *Herschel* observations, $L_{IR} = 10^{9.2} - 10^{11.8}$ $L_\odot$, and stellar masses of $\langle M_* \rangle = 10^{10}$ $M_\odot$.

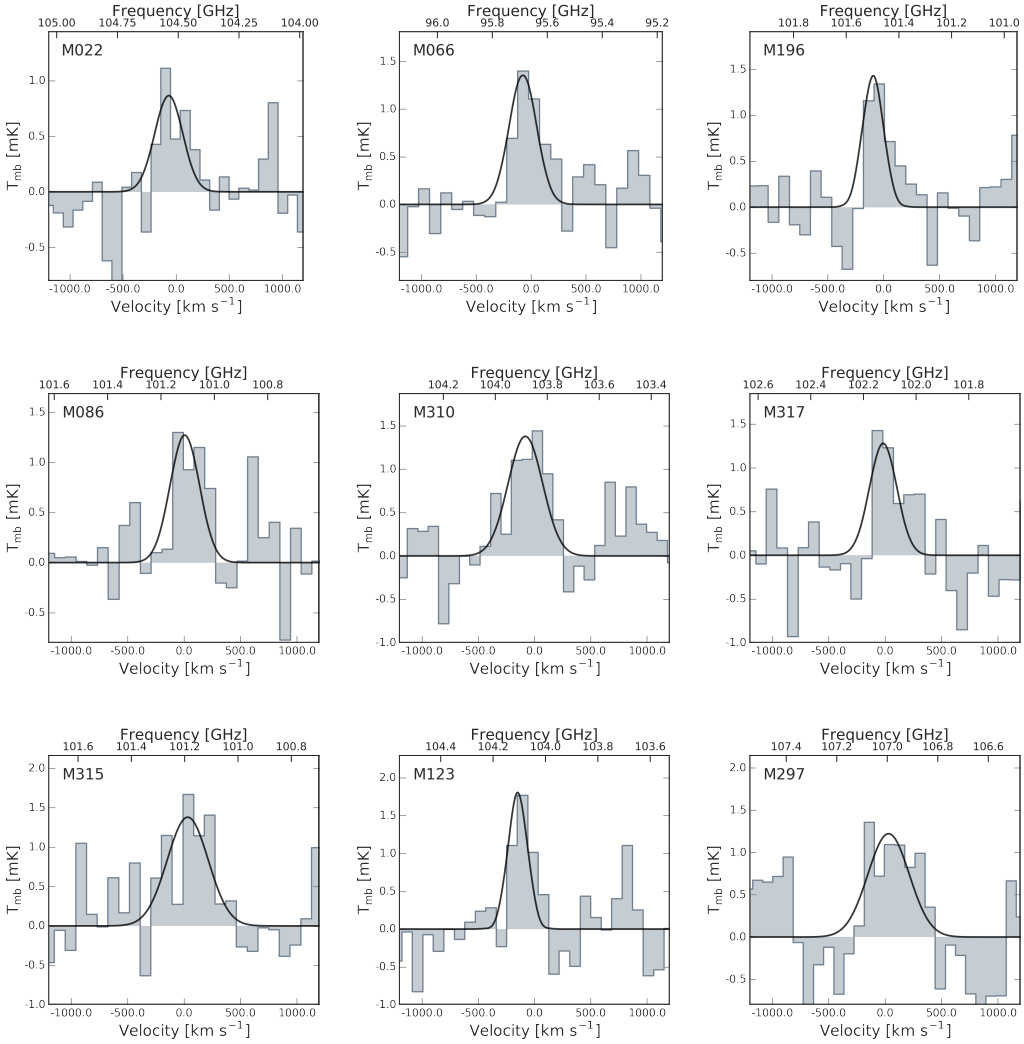

Figure 2.2: CO(1 – 0) spectra with antenna temperature [mK] as a function of velocity [km s^{-1}] of CO-detected 5MUSES galaxies followed-up with IRAM/EMIR. All spectra are smoothed to a velocity resolution of ~ 70 km s^{-1}. A line is considered detected if the integrated signal is above 3σ. The black line shows the best-fitting Gaussian profile to the observed CO line.

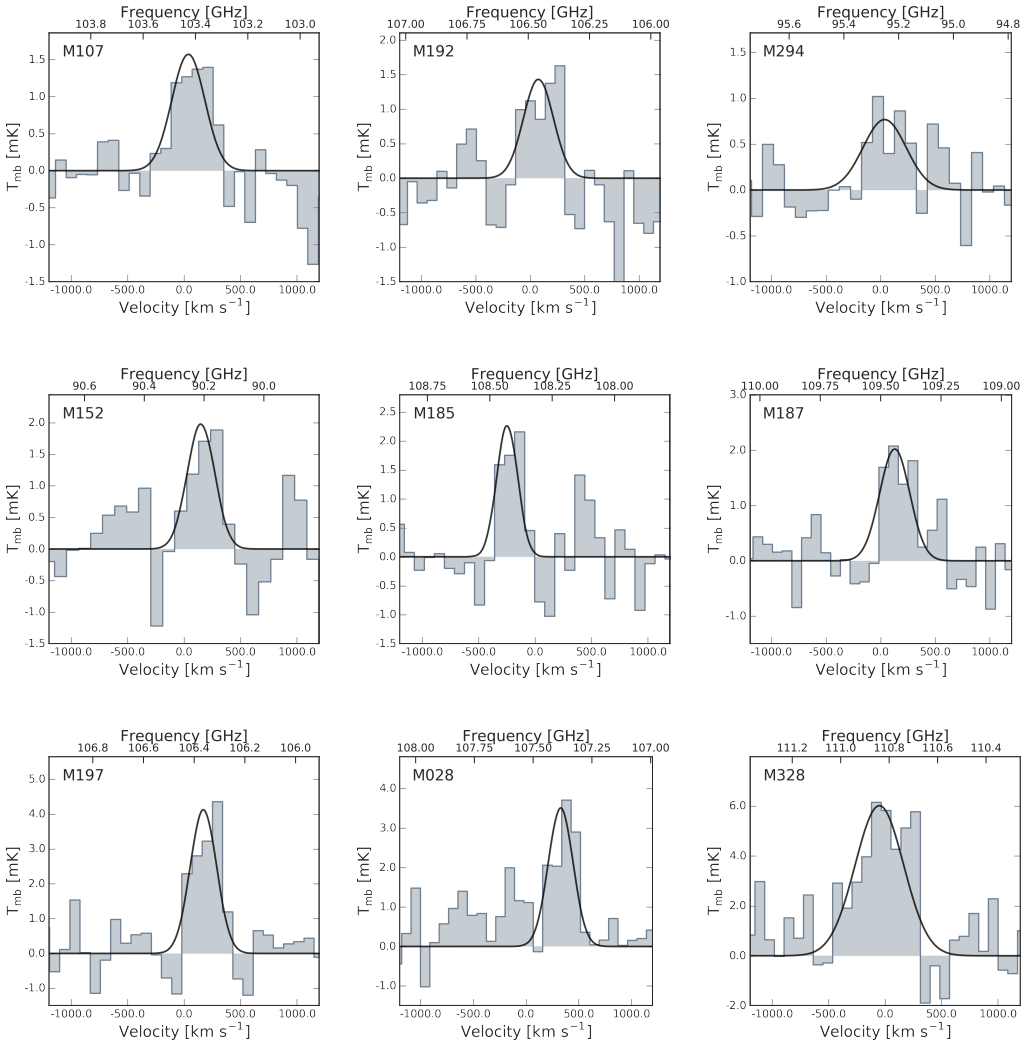

Figure 2.2: *–Continued*

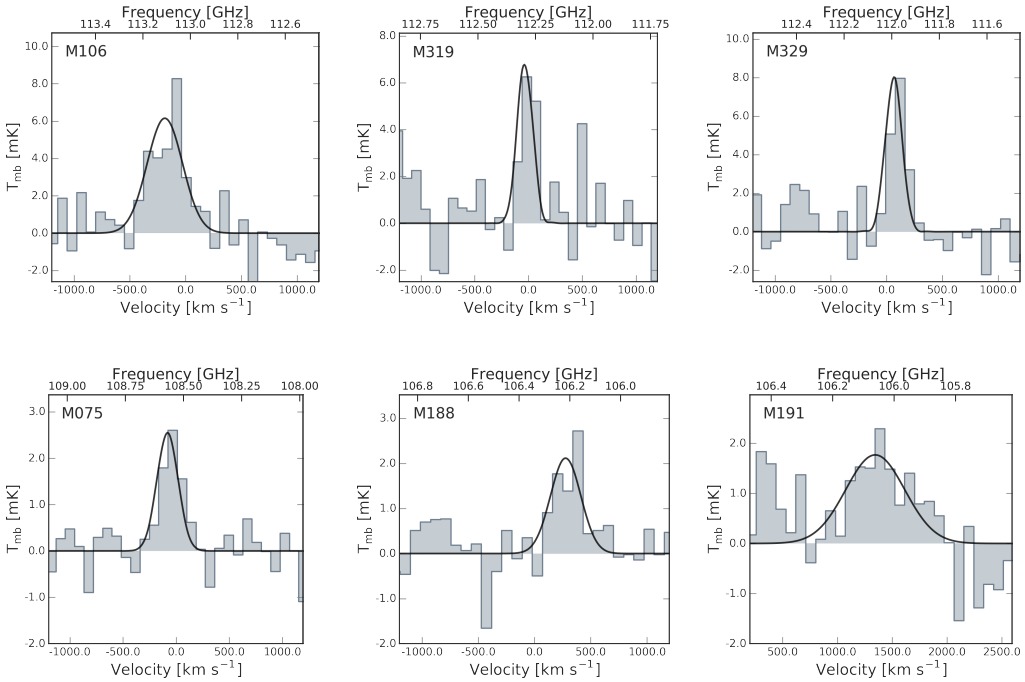

Figure 2.2: –*Continued*

2.2.1 *New CO*(1 – 0) *line observations*

The single-dish observations were carried out with the IRAM 30 m telescope at Pico Veleta, Spain, in 2015 July, 2015 June, and 2016 September. All galaxies were observed at 3 mm using the spectral line receiver band E0 of EMIR with WILMA as backends in order to observe the CO(1 – 0) emission line. The receiver was tuned to the expected frequency of the targets (in the range 95 GHz $< \nu <$ 107 GHz) and the wobbler switching mode was used. We spent one to height hours on each galaxy. During observations the pointing of the telescope was checked every two hours using a bright nearby source. The velocity-integrated CO line intensities were converted from antenna temperature scale (T_a^*) to Jy using $S/T_a^* = 6.2\,\mathrm{Jy\,K^{-1}}$. The CO(1 – 0) line luminosities were estimated in units of [$\mathrm{K\,km\,s^{-1}\,pc^2}$] using the following equation from Solomon & Vanden Bout (2005):

$$L'_{\mathrm{CO}} = 3.25\times10^7 S_{\mathrm{CO}}\Delta v\ \nu_{\mathrm{obs}}^{-2}\ D_{\mathrm{L}}^2(1+z)^3 \qquad (2.1)$$

where $S_{\mathrm{CO}}\Delta v$ [$\mathrm{Jy\,km\,s^{-1}}$] is the velocity integrated flux, ν_{obs} [GHz] is the observed CO(1 – 0) frequency, and D_{L} [Mpc] is the luminosity distance.

Spectra were reduced using the CLASS/GILDAS[2] software, where each galaxy spectrum was averaged and smoothed to a velocity resolution of 70 – 100 $\mathrm{km\,s^{-1}}$. Linear baselines were assumed for all targets. The spectra of galaxies with detected CO(1 – 0) line emission are shown in Figure 2.2. A detected CO line is considered when the integrated signal is above 3σ. We detect significant CO line emission in 24 galaxies, whereas upper limits are determined for the remaining targets assuming a CO(1 – 0) line width of 300 $\mathrm{km\,s^{-1}}$. The CO luminosities and the observed properties of each galaxy from our observing runs are listed in Table 2.1.

[2] http://www.iram.fr/IRAMFR/GILDAS

Table 2.1: CO(1 – 0) line observations of the 5MUSES targets from our programs.

ID[a]	R.A. [hh:mm:ss]	Decl. [dd:mm:ss]	z_{co}	FWHM[e] [km s^{-1}]	$S_{CO}\Delta v$ [Jy km s^{-1}]	$\log(L'_{CO}{}^{d})$	rms[f] [mK]
20	02 : 19 : 09.6	−05 : 25 : 12.9	0.098[b]	–	<0.16	<7.87	0.94
22	02 : 19 : 16.1	−05 : 57 : 27.0	0.103	311 ± 84	1.79 ± 0.47	8.95 ± 0.11	0.30
28	02 : 19 : 53.0	−05 : 18 : 24.2	0.073	261 ± 73	5.94 ± 1.40	9.16 ± 0.10	0.61
36	02 : 21 : 47.9	−04 : 46 : 13.5	0.025[b]	–	<0.65	<7.27	0.57
64	02 : 25 : 48.2	−05 : 00 : 51.5	0.150[c]	–	<0.31	<8.52	0.29
66	02 : 26 : 00.0	−05 : 01 : 45.3	0.205	274 ± 59	2.37 ± 0.45	9.69 ± 0.08	0.16
75	02 : 27 : 41.6	−04 : 56 : 50.6	0.055	173 ± 61	3.27 ± 0.85	8.66 ± 0.11	0.07
86	10 : 36 : 46.4	+58 : 43 : 30.6	0.140	307 ± 80	2.58 ± 0.71	9.38 ± 0.12	0.28
106	10 : 44 : 38.2	+56 : 22 : 10.8	0.024	375 ± 68	15.22 ± 2.38	8.64 ± 0.07	1.31
107	10 : 44 : 54.1	+57 : 44 : 25.8	0.118	345 ± 74	3.59 ± 0.79	9.37 ± 0.10	0.21
118	10 : 49 : 07.2	+56 : 57 : 15.4	0.071	–	<3.55	<8.93	0.80
123	10 : 50 : 06.0	+56 : 15 : 00.0	0.118	215 ± 56	2.65 ± 0.63	9.25 ± 0.10	0.21
146	10 : 59 : 03.5	+57 : 21 : 55.1	0.117[b]	–	<0.87	<8.76	0.51
152	11 : 01 : 33.8	+57 : 52 : 06.6	0.275	285 ± 89	3.71 ± 1.15	10.15 ± 0.13	0.24
185	16 : 08 : 58.4	+55 : 30 : 10.3	0.065	221 ± 38	3.40 ± 0.66	8.84 ± 0.08	0.37
187	16 : 09 : 07.6	+55 : 24 : 28.4	0.065	396 ± 300	5.28 ± 1.07	9.01 ± 0.09	0.39
188	16 : 09 : 08.3	+55 : 22 : 41.5	0.085	313 ± 73	5.28 ± 1.07	9.01 ± 0.09	0.54
191	16 : 09 : 31.6	+54 : 18 : 27.4	0.086	645 ± 165	7.58 ± 1.67	9.38 ± 0.10	0.36
192	16 : 09 : 37.5	+54 : 12 : 59.3	0.086	294 ± 136	3.28 ± 0.64	9.06 ± 0.08	0.13
196	16 : 12 : 23.4	+54 : 03 : 39.2	0.138	210 ± 65	1.93 ± 0.53	9.24 ± 0.12	0.18
197	16 : 12 : 33.4	+54 : 56 : 30.5	0.084	279 ± 38	7.76 ± 1.13	9.40 ± 0.06	0.88
198	16 : 12 : 41.1	+54 : 39 : 56.8	0.035[b]	–	<1.23	<7.84	0.61
200	16 : 12 : 50.9	+53 : 23 : 05.0	0.047	–	<5.50	<8.77	0.85
202	16 : 12 : 54.2	+54 : 55 : 25.4	0.065	–	<5.48	<9.03	0.99
294	17 : 12 : 32.4	+59 : 21 : 26.2	0.210	307 ± 55	2.00 ± 0.26	9.64 ± 0.06	0.03
297	17 : 13 : 16.6	+58 : 32 : 34.9	0.079	437 ± 101	3.62 ± 0.97	9.02 ± 0.12	0.33
302	17 : 14 : 46.4	+59 : 33 : 59.8	0.131	–	<3.49	<9.44	0.75
310	17 : 17 : 11.1	+60 : 27 : 10.0	0.110	350 ± 99	3.15 ± 0.79	9.26 ± 0.11	0.17
315	17 : 19 : 33.3	+59 : 27 : 42.7	0.139	423 ± 131	3.85 ± 1.05	9.55 ± 0.12	0.42
316	17 : 19 : 44.9	+59 : 57 : 07.1	0.069	–	<2.15	<9.03	1.36
317	17 : 20 : 43.3	+58 : 40 : 26.9	0.125	329 ± 152	2.81 ± 0.73	9.32 ± 0.11	0.11
319	17 : 21 : 59.3	+59 : 50 : 34.2	0.028	168 ± 46	7.67 ± 1.96	8.44 ± 0.11	0.51
328	17 : 25 : 46.8	+59 : 36 : 55.3	0.035	393 ± 137	13.89 ± 2.53	8.89 ± 0.08	0.24
329	17 : 25 : 51.3	+60 : 11 : 38.9	0.029	171 ± 35	9.10 ± 1.67	8.54 ± 0.08	0.04

Notes. [a] 5MUSES ID name.
[b] b The NASA/IPAC Extragalactic Data base (NED) is operated by the Jet Propulsion Laboratory, California Institute of Technology, under contract with the National Aeronautics and Space Administration.
[c] For sources with CO(1 – 0) 3σ upper limits, the redshift is derived from the IRS spectra (b) or obtained from the NASA/IPAC Extragalactic Database (c) as listed in Wu et al. (2010).
[d] L'_{CO} luminosities are in units of [K km s^{-1} pc^2].
[e] The CO line width is estimated by measuring the full width at half-maximum (FWHM) of the Gaussian profile.
[f] For galaxies with > 3σ CO detection and upper limits, we list the RMS of the CO line and the baseline, respectively.

Table 2.2: Data sample overview.

Sample	N	z	$\log(L_{\rm IR}/{\rm L}_\odot)$	PAH feature	CO line	References [PAH, CO]
SINGS	36	0.001 – 0.007	7.31 – 10.60	6.2 µm	(3 – 2)	S07, W12
Local ULIRGs	9, (9)	0.018 – 0.191	11.99 – 12.42	6.2 µm, 7.7 µm	(1 – 0)	P13
5MUSES	22, (24)	0.025 – 0.277	9.23 – 11.81	6.2 µm, 7.7 µm	(1 – 0)	W10, this paper
5MUSES	14, (15)	0.053 – 0.360	10.35 – 12.10	6.2 µm, 7.7 µm	(1 – 0)	W10, K14
high-z SFGs	4, (3)	1.016 – 1.523	11.86 – 12.66	6.2 µm, 7.7 µm	(1 – 0), (2 – 1)	P13
SMGs	6, (8)	1.562 – 4.055	12.30 – 13.08	6.2 µm, 7.7 µm	(1 – 0), (2 – 1), (3 – 2), (4 – 3)	P13
High-z SBs	(6)	1.562 – 2.470	12.55 – 12.93	6.2 µm, 7.7 µm	(2 – 1), (3 – 2)	Sa07, Y07

Notes. The table includes all galaxies with at $3 \geqslant \sigma$ CO and PAH detections.
Column (1): Galaxy sample; column (2): Number of galaxies with PAH 6.2 µm (and 7.7 µm) detections; column (3): Redshift range; column (4): IR luminosity range; column (5): Detected PAH feature; column (6): Observed CO transition line; column (7): References: S07: Smith et al. (2007), W12: Wilson et al. (2012), P13: Pope et al. (2013) and references therein, W10: Wu et al. (2010), K14: Kirkpatrick et al. (2014), Sa07: Sajina et al. (2007), Y07: Yan et al. (2007).

2.2.2 *Literature data*

To expand our data sample, we include published observations of galaxies at all redshifts with both CO, IR, and PAH detection from the literature. General properties of the data compilation are listed in Table 2.2.

2.2.2.1 5MUSES galaxies

In a recent study, Kirkpatrick et al. (2014) carried out CO(1 – 0) line observations of 24 intermediate redshift galaxies ($z = 0.04 – 0.36$), also selected from the 5MUSES sample, with the Redshift Search Receiver (RSR) on the Large Millimetre Telescope (LMT). Their sample covers a broader range of $L_{\rm IR}$ ($10^{10.4} – 10^{12.1}$ $L_\odot$) and $EW_{6.2}$ (0.07 – 0.70 µm) as opposed to our targets. They detected CO(1 – 0) emission in 17 of the 24 sources which we combine with our sample for the analysis (14 of these have 3σ PAH 6.2 µm detection). For consistency, we derive CO line luminosities using the velocity-integrated line flux reported in Kirkpatrick et al. (2014). The final sample of intermediate redshift galaxies with both CO and PAH 6.2 µm detections in our study consists of 36 targets, all drawn from the 5MUSES compilation, of which 24 are from our new IRAM survey and 14 from Kirkpatrick et al. (2014).

2.2.2.2 SINGS

The *Spitzer* Infrared Nearby Galaxy Survey (SINGS; Kennicutt et al. 2003) is an imaging and low-resolution ($R \sim 50 – 100$) spectroscopic survey of 75 local galaxies with 5 – 38 µm spectral mapping with *Spitzer* IRS. The low-resolution 5 – 15 µm spectral map (55 arcsec × 34 arcsec) is centred on the nucleus of each galaxy. From the SINGS sample, Smith et al. (2007) selected 59 galaxies with spectral coverage between 5 and 38 µm from both SL and LL in order to detect PAH emission within the central regions of each galaxy. PAH features were derived using PAHFIT and fitted with Drude profiles. A subsample of 57 SINGS galaxies have both PAH emission and FIR coverage based on *Herschel* PACS and SPIRE observations as presented in Dale et al. (2012).

From the SINGS survey, Wilson et al. (2012) selected 47 galaxies (NGLS: Nearby Galaxies Legacy Survey) to carry out CO(3 – 2) line observations with the James Clerk Maxwell Telescope (JCMT). To correct the CO(3 – 2) emission to CO(1 – 0) we adopt a CO(3 – 2)/CO(1 – 0) line ratio of $r_{32/10} = 0.18 \pm 0.02$ based on a comparison study by Wilson et al. (2012). They estimate an average

CO(3 – 2) and CO(1 – 0) line ratio using 11 nearby galaxies from the NGLS sample that overlap with CO(2 – 1) observations carried out by Kuno et al. (2007). We apply an aperture correction ($f_{\rm TIR}$) listed in Smith et al. (2007) to the IR and CO(1 – 0) luminosities and increase the uncertainties of the aperture-corrected luminosities by a factor of 2, in order to compare these with the PAH emission arising from the central part of the galaxy.

Given the different physical scales probed by the available PAH, CO, and dust emission observations of the SINGS galaxies, we choose to exclude them from our statistical analysis to avoid biases in our regression models due to possible systematics and uncertainties introduced by the aperture corrections. However, since the SINGS sample consists of representative, normal PAH emitting SFGs in the local Universe, for the sake of completeness we choose to overplot them in the various luminosity scaling relations presented in this study.

Table 2.3: General properties of the 5MUSES sample.

ID[a]	R.A.	Decl.	z	$\log(L_{6.2})^b$	$EW_{6.2}$	$\log(L_{7.7})^b$	$\log(M_*)^c$	$\log(L_{\rm IR})$	$\log(M_{\rm d})$	$\log(M_{\rm H_2})$
	[hh:mm:ss]	[dd:mm:ss]		[$L_\odot$]	[μm]	[$L_\odot$]	[$M_\odot$]	[$L_\odot$]	[$M_\odot$]	[$M_\odot$]
2	02 : 15 : 03.5	−04 : 24 : 21.7	0.137	8.58 ± 0.19	0.78 ± 0.01	9.19 ± 0.14	10.51	10.86 ± 0.04	8.01 ± 0.28	10.01
4	02 : 15 : 57.1	−03 : 37 : 29.1	0.032	7.59 ± 0.08	0.50 ± 0.05	8.09 ± 0.09	9.97	9.83 ± 0.02	7.18 ± 0.29	9.18
5	02 : 16 : 38.2	−04 : 22 : 50.9	0.304	9.06 ± 0.24	<0.09	9.48 ± 0.11	10.80	11.54 ± 0.02^d	–	–
6	02 : 16 : 40.7	−04 : 44 : 05.1	0.870	9.13 ± 1.62	<0.05	–	11.82	12.70 ± 0.01^d	–	–
8	02 : 16 : 49.7	−04 : 25 : 54.8	0.143	9.01 ± 0.09	1.11 ± 0.06	9.48 ± 0.08	10.06	10.99 ± 0.01	7.29 ± 0.42	9.29
...	...	...	...	...	...	...	...	...	...	...

Notes. Column (1): Source name; column (2): Right ascension in units of hours, minutes, and seconds; column (3): Declination in units of degrees, arcminutes, and arcseconds; column (4): Redshift; column (5): PAH 6.2 μm luminosity; column (6): Equivalent width of the PAH 6.2 μm feature; column (7): PAH 7.7 μm luminosity; column (8): Stellar mass; column (9): Infrared luminosity (integrated from 8 – 1000 μm); column (10): Dust mass; column (11): Molecular gas mass derived using the $M_{\rm d}$–$\delta_{\rm GDR}$ method.
[a] 5MUSES ID name.
[b] PAH luminosity from Magdis et al. (2013).
[c] Stellar masses from Shi et al. (2011).
[d] $L_{\rm IR}$ from Shi et al. (2011).

Table 2.4: Galaxies from the literature with PAH, IR and/or CO.

Name	R.A. [hh:mm:ss]	Decl. [dd:mm:ss]	Sample	z	$\log(L_{6.2}/\mathrm{L}_\odot)$	$\mathrm{EW}_{6.2}$ [µm]	$\log(L_{7.7}/\mathrm{L}_\odot)$	$\log(L_{\mathrm{IR}}/\mathrm{L}_\odot)$	Line	$\log(L'_{\mathrm{CO}}/\mathrm{L}_\odot)$
NGC 3049	09 : 54 : 49.59	+09 : 16 : 18.1	SINGS	0.006	7.81 ± 0.02^a	–	–	9.65 ± 0.02	CO(3 – 2)	7.68 ± 0.21
IRAS 10565 + 2448	10 : 59 : 18.1	+24 : 32 : 34	local ULIRGs	0.043	9.57 ± 0.01	–	–	12.04 ± 0.02^c	CO(1 – 0)	9.72 ± 0.03^c
GN26	12 : 36 : 34.51	+62 : 12 : 40.9	SMGs	1.223	10.48 ± 0.02	0.38 ± 0.04	11.01 ± 0.10	12.66 ± 0.17^c	CO(2 – 1)	10.92 ± 0.12^c
GN70.211	12 : 37 : 10.60	+62 : 22 : 34.5	High-z SFGs	1.523	10.39 ± 0.10	–	10.84 ± 0.12	11.94 ± 0.17^c	CO(1 – 0)	10.20 ± 0.12^c
MIPS506	17 : 11 : 38.59	+58 : 38 : 38.58	High-z SBs	2.470	–	0.30 ± 0.14^d	11.11 ± 0.13	12.93 ± 0.09^e	CO(3 – 2)	10.52 ± 0.09^e
...	...	...	...	...	...	...	...	...	...	

Notes. Column (1): Source name; column (2): Right ascension in units of hours, minutes, and seconds; column (3): Declination in units of degrees, arcminutes, and arcseconds; column (4): Galaxy sample or selection; column (5): Redshift; column (6): PAH 6.2 µm luminosity; column (7): Equivalent width of the PAH 6.2 µm feature; column (8): Infrared luminosity (integrated from 8 – 1000 µm); column (9): Observed CO line; column (10): CO(1 – 0) luminosity.

[a] From Smith et al. (2007).

[b] From Wilson et al. (2012). Converted to CO(1 – 0) using $r_{32/10} = 0.18 \pm 0.02$.

[c] From Pope et al. (2013). For the CO luminosities, we corrected higher-J transitions using the conversion scheme listed in Bothwell et al. (2013): $r_{21/10} = 0.84 \pm 0.13$, $r_{32/10} = 0.52 \pm 0.09$, $r_{43/10} = 0.41 \pm 0.07$.

[d] From Sajina et al. (2007).

[e] From Yan et al. (2010).

[f] From Pope et al. (2008a).

[g] From Kirkpatrick et al. (2014).

2.2.2.3 Local ULIRGs and high-z galaxies

Pope et al. (2013) carried out CO(2 – 1) observations using IRAM PdBI and *Spitzer* MIR spectroscopy of six 70 µm selected galaxies from the *Spitzer* Far-Infrared Deep Extragalactic Legacy survey (Dickinson & FIDEL Team 2007) of GOODS-N with optical spectroscopic redshift at $z = 1 - 1.5$. The sample has *Spitzer* IRS observations and photometric coverage from *Spitzer* MIPS (24 and 70 µm) and *Herschel* PACS (100 and 160 µm) and SPIRE (250, 350, and 500 µm) observations from the GOODS-*Herschel* survey (Elbaz et al. 2011). As in Pope et al. (2013), we complement our sample with galaxies from the literature containing detected CO and PAH emission at all redshifts. These include 12 high-z galaxies (SMGs, BzKs, and 70 µm selected galaxies) from various studies at $1.1 < z < 4.1$ (Pope et al. 2008a; Frayer et al. 2008; Aravena et al. 2010; Carilli et al. 2010; Casey et al. 2011; Ivison et al. 2011; Magnelli et al. 2012a; Bothwell et al. 2013; Riechers et al. 2013). Stellar masses from Pope et al. (2013) are available for the 70 µm selected galaxies. Based on the offset from the MS, we classify the 70 µm as high-z SFGs galaxies whereas the remaining galaxies at $z > 1$ are labelled as SMGs. Similarly, we include the 24 µm selected sample ($S_{24} > 0.9$ mJy) of nine $z \sim 1 - 2$ ULIRGs in the *Spitzer* XFLS field with CO(2 – 1) or CO(3 – 2) observations from Yan et al. (2010) that also has existing *Spitzer* MIR spectra published in Yan et al. (2007) and Sajina et al. (2007).

For galaxies with only high-J CO line observations, we convert the CO luminosities to $L'_{\rm CO}$ by adopting the conversion factors listed in Bothwell et al. (2013): $r_{21/10} = 0.84 \pm 0.13$, $r_{32/10} = 0.52 \pm 0.09$, $r_{43/10} = 0.41 \pm 0.07$. At lower redshift, we also include 13 local ULIRGs with *Spitzer* IRS MIR spectra from Armus et al. (2007) and Desai et al. (2007) with existing CO observations and IR luminosities (Sanders, Scoville & Soifer 1991; Solomon et al. 1997; Kim, Veilleux & Sanders 1998; Farrah et al. 2003; Gao & Solomon 2004; Chung et al. 2009). The CO, IR, and PAH luminosities of the literature compilation are available in the online version (See Table 2.4).

2.2.3 *Derivation of MIR and FIR dust properties*

We combine the existing multi-wavelength photometry from *Spitzer* (MIPS: 24, 160 µm) and *Herschel* (SPIRE: 250, 350, 500 µm) in order to estimate IR luminosities and dust masses ($M_{\rm d}$) by modeling the FIR part of the spectral

energy distribution (SED) for each galaxy in the 5MUSES sample. We use silicate-graphite-PAH models from Draine & Li (2007) (DL07) including diffuse ISM and photodissociation region (PDR) components. The best-fitting parameters and results are listed in the online version (see Table 2.3). $L_{\rm IR}$ is derived by integrating the SED model between rest-frame 8 – 1000 μm. The SFR for each galaxy is estimated using the $L_{\rm IR}$–SFR conversion in Kennicutt (1998) assuming a Salpeter (1955) IMF: SFR [$M_\odot$ yr^{-1}]= 1.72×10^{-10} $L_{\rm IR}$. This technique of FIR SED modeling is applied to the 5MUSES sample including 165 galaxies. In addition, we estimate monochromatic dust luminosities using the *Spitzer* MIPS (24 and 160 μm) and *Herschel* SPIRE photometric bands (250, 350, and 500 μm). We derive PAH luminosities from the *Spitzer* IRS data using PAHFIT (Smith et al. 2007). For galaxies in the literature where the PAH luminosities have been estimated using the spline method, we derive the PAH luminosities using PAHFIT to ensure that the PAH 6.2 and 7.7 μm emissions have been estimated in a consistent way for both our targets and the literature compilation.

To summarize, the full sample with both detected CO, PAH 6.2 μm, and IR emission contains 36 5MUSES galaxies (including 5 AGNs and composite sources), 36 SINGS galaxies, 9 local ULIRGs, 4 high-z SFGs, and 6 SMGs (See Table 2.2).

2.3 RESULTS

Previous works have studied scaling relations between the $L_{\rm IR}$, $L_{\rm PAH}$, and $L'_{\rm CO}$ of various galaxy populations across a wide range of redshifts (e.g. Calzetti et al. 2005; Smith et al. 2007; Bendo et al. 2008; Pope et al. 2013; Rujopakarn et al. 2013; Kirkpatrick et al. 2014). In this section, we will revisit these relations for our sample, attempting to identify outliers and investigate them not only as a function of lookback time but also as a function of physical conditions (AGN, SBs, normal galaxies, etc).

2.3.1 *The relation between IR and PAH luminosity*

As discussed in the Introduction, $L_{\rm PAH}/L_{\rm IR}$ variations may not only be driven by the presence of an AGN and the geometry of the star formation but also by the metallicity and the hardness of the radiation field. To investigate the $L_{\rm PAH}/L_{\rm IR}$ variations in different galaxy populations across a wide range of

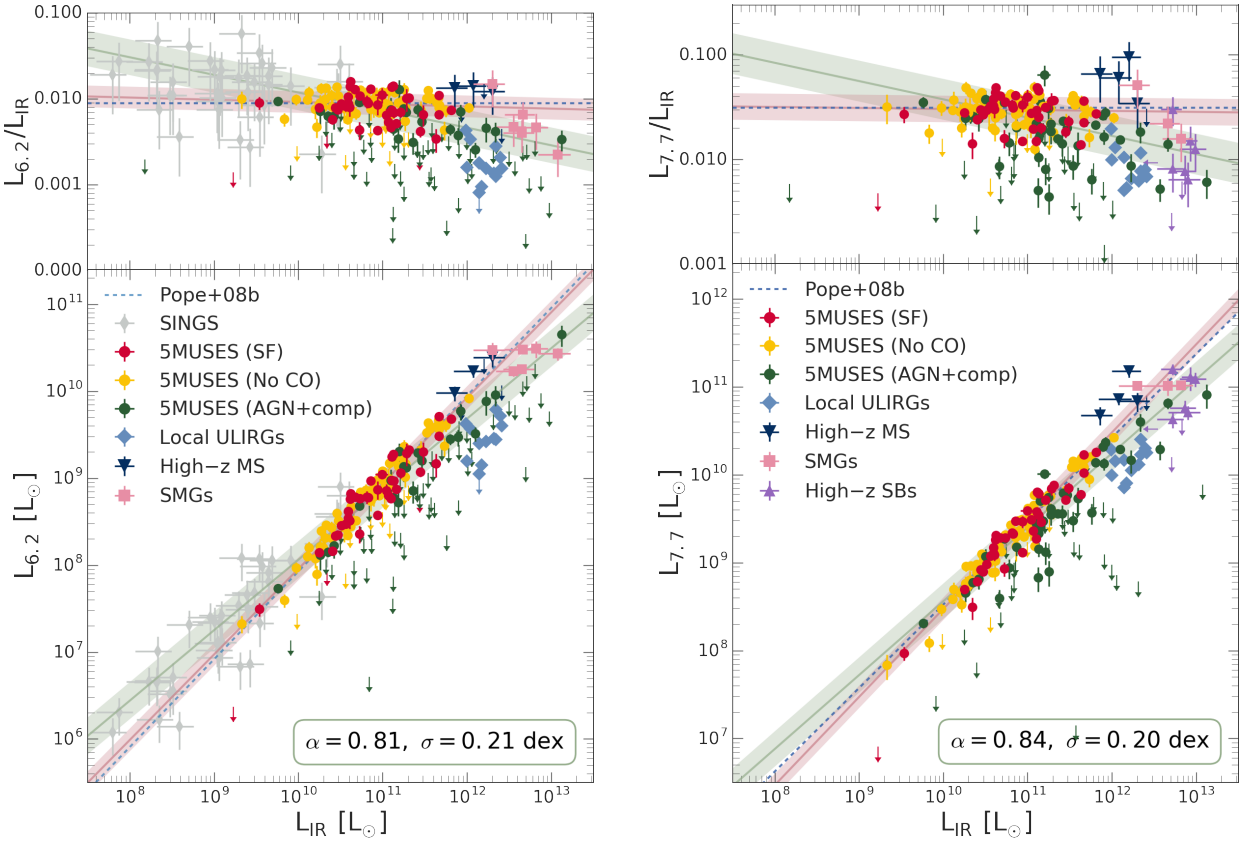

Figure 2.3: Correlation between the total infrared luminosity (L_{IR}) versus PAH 6.2 µm luminosity ($L_{6.2}$) (*left*) and PAH 7.7 µm luminosity ($L_{7.7}$) (*right*). For the 5MUSES sample, we include CO-detected SFGs (red), AGNs and composite sources (green), and the remaining sample of SFGs (yellow). $L_{6.2}$ and $L_{7.7}$ upper limits are shown as arrows. We also include SINGS galaxies (grey, only for $L_{6.2}$), local ULIRGs (light blue), high-z SFGs (dark blue), SMGs (pink), and high-z SBs (purple, only for $L_{7.7}$). The green and pink lines depict the L_{PAH}–L_{IR} linear regression models of the SFGs (5MUSES and high-z SFGs) and the full sample, respectively, excluding the SINGS sources as described in Section 2.2.2.2. The same method is applied to the L_{PAH}/L_{IR} versus L_{IR} relations presented in the upper panels. The shaded regions present the intrinsic scatter of the best fits. The blue dashed lines show the best-fitting relations from Pope et al. (2008a) of local SBs and SMGs. For the upper panels, the dashed lines are the median value of the L_{PAH}/L_{IR} assuming L_{PAH}-L_{IR} slopes of unity.

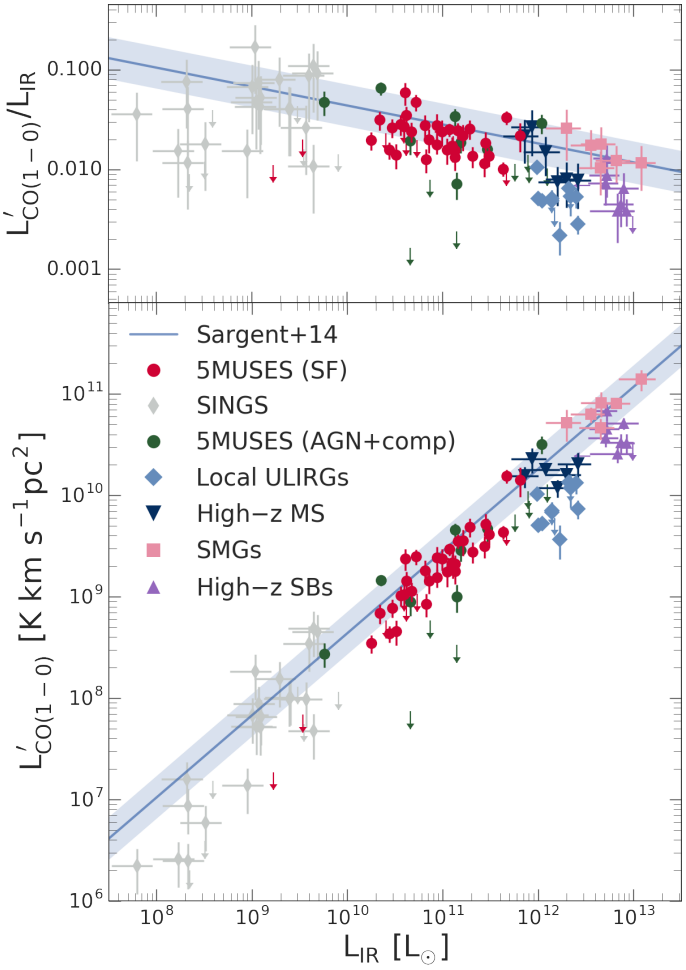

Figure 2.4: Correlation between CO(1 – 0) line luminosity (L'_{CO}) and L_{IR}. Colour coding and symbols follow Figure 2.3. Higher-J CO transitions from the literature are corrected to CO(1 – 0) using Wilson et al. (2012) for the SINGS galaxies and Bothwell et al. (2013) are adopted for the remaining sample. The blue lines shows the L'_{CO}–L_{IR} relation from Sargent et al. (2014). The top panel shows the L'_{CO}/L_{IR} ratio in units of [(K km s^{-1} pc^2)/L$_\odot$] as a function of L_{IR} along with the Sargent et al. (2014) relation. The blue shaded regions depict the observed dispersion of 0.21 dex.

redshifts, we consider the $L_{6.2}$, $L_{7.7}$, and $L_{\rm IR}$ measurements for the 5MUSES sample as well as for other galaxies in the literature for which such measurements are available, including local ULIRGs (Armus et al. 2007; Desai et al. 2007), high-z ($1 < z < 4$) SMGs, BzKs and 70 μm selected galaxies (Pope et al. 2008a; Pope et al. 2013, and references therein), and 24 μm selected SBs at $z \sim 2$ (Yan et al. 2010). Due to possible biases introduced from the aperture correction applied to the SINGS galaxies (Kennicutt et al. 2003), we omit them from the best-fitting regression models.

In Figure 2.3, we plot the PAH 6.2 μm and 7.7 μm luminosities as a function $L_{\rm IR}$ for our full sample of galaxies and model the data in the logarithmic space using the Bayesian linear regression analysis as described in Kelly (2007). This method accounts for measurement errors of both the dependent and independent variables and it returns posterior distributions of the best-fitting parameters, including the intrinsic scatter. All the best-fitting parameters of the regression model: $\log y = \alpha \times \log x + \beta$ are listed in Table 2.5. Focusing only on local/intermediate redshift star-formation dominated sources and high-z SFGs that are part of the MS of star formation, we find a tight, linear correlation, with a slope of $\alpha = 0.98 \pm 0.03$ and intrinsic scatter of $\sigma = 0.13$ dex for the $L_{6.2}$–$L_{\rm IR}$ relation, while $\alpha = 1.00 \pm 0.03$ and $\sigma = 0.13$ dex for $L_{7.7}$–$L_{\rm IR}$, in agreement with the best-fitting relations reported in Pope et al. (2008a) and similar studies (e.g.. Sajina et al. 2008; Rujopakarn et al. 2013; Shipley et al. 2016). The dispersion of the $L_{\rm PAH}/L_{\rm IR}$ ratios as a function of $L_{\rm IR}$ and galaxy type is shown in the top panels of Figure 2.3. From these relations, local ULIRGs (and high-z SBs with available $L_{7.7}$ estimates) exhibit systematically lower PAH/IR luminosity ratios. We quantify these galaxies as outliers lying 3.2σ from the best-fitting relations (2.5σ for $L_{7.7}$–$L_{\rm IR}$). Fitting the full sample (excluding upper limits), yields a shallower slope but also an increased intrinsic scatter of $\sigma = 0.21$ dex and $\sigma = 0.20$ dex for the $L_{6.2}$–$L_{\rm IR}$ and $L_{7.7}$–$L_{\rm IR}$ relations, respectively. We note though, that a considerable fraction of local ULIRGs and high-z SBs are still outliers, even when attempting to fit the whole sample, in agreement with Shipley et al. (2016). It is thus evident that a universal $L_{\rm IR}$–$L_{6.2}$ relation, accommodating the various physical conditions of different galaxy populations, cannot be established.

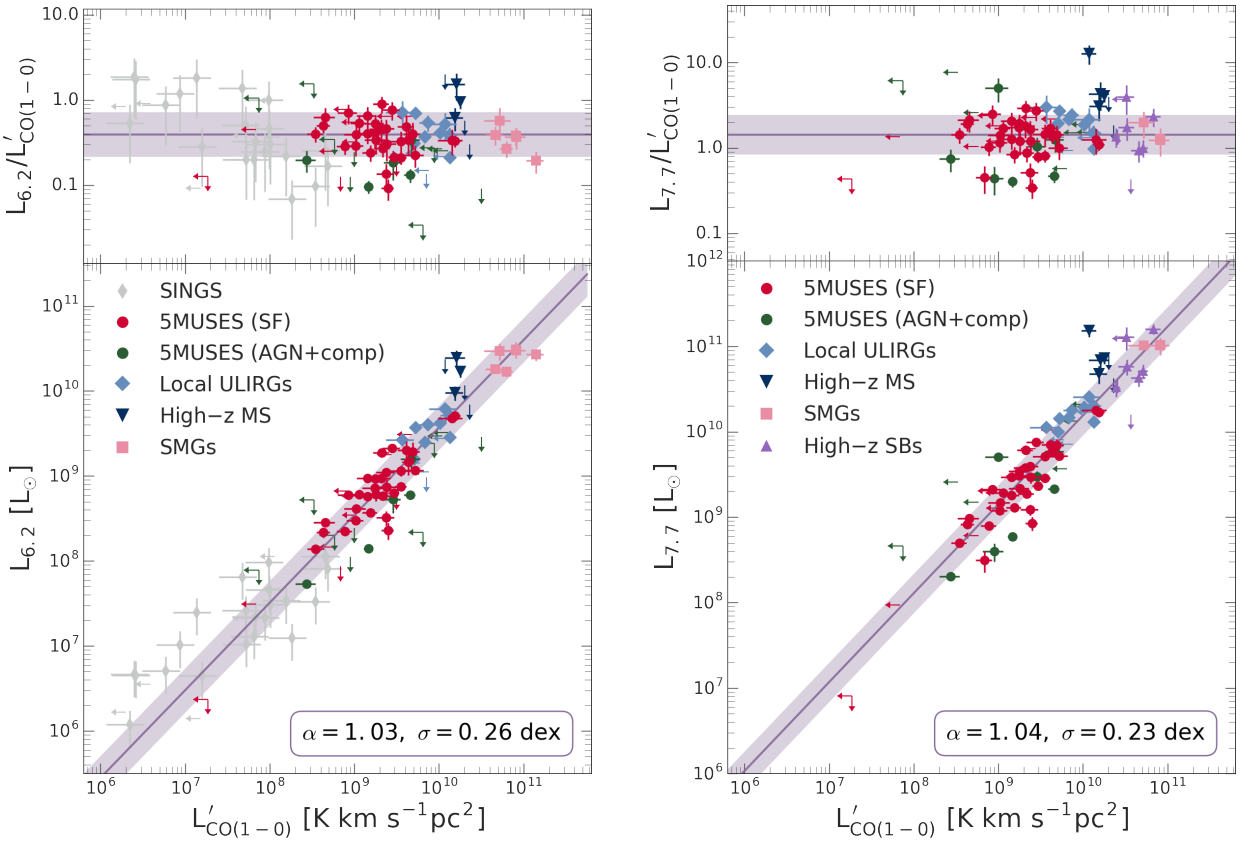

Figure 2.5: Correlation between $L_{6.2}$ versus L'_{CO}(*left*) and $L_{7.7}$ versus L'_{CO} (*right*). Colour coding and symbols follow Figure 2.3. The top panels show the PAH and CO luminosity ratios in units of $[L_\odot/(K\,km\,s^{-1}\,pc^2)]$ and as a function of L'_{CO}. SINGS galaxies (grey) are excluded from the fitting procedure due to possible systematics introduced from the applied aperture correction (See Section 2.2.2.2). The purple lines and shaded regions depict the best-fitting linear regression and its intrinsic scatter for all the galaxies. For the upper panels, we show the observed dispersion assuming a L_{PAH}–L'_{CO} slope of unity. The fit parameters of the CO–PAH luminosity relations are listed in Table 2.5.

2.3.2 *The CO–IR luminosity relation*

The use of $L_{\rm IR}$ as a SFR tracer and the fact that CO emission is directly associated with the molecular gas reservoir of a galaxy, has motivated several studies to investigate the $L'_{\rm CO}$–$L_{\rm IR}$ relation as a proxy of the star formation law that links the SFR to the molecular gas of galaxies (KS law). The existence of a universal $L'_{\rm CO}$–$L_{\rm IR}$ (and thus of a universal $M_{\rm gas}$–SFR) relation has been challenged by recent observations of different galaxy populations at various redshifts (e.g.. Bouché et al. 2007; Daddi et al. 2010b; Genzel et al. 2010; Krumholz, Dekel & McKee 2012; Silverman et al. 2015). Although the debate is still open, there are claims that MS galaxies at all redshifts tend to follow a unique $L'_{\rm CO}$–$L_{\rm IR}$ relation from which local ULIRGs and high-z SBs are outliers exhibiting lower $L'_{\rm CO}/L_{\rm IR}$ ratios, indicative of higher SFEs (e.g.. Daddi et al. 2010b; Genzel et al. 2010). Addressing the question of this possible bimodality is beyond the scope of our work. Instead, we wish to investigate how the galaxies at different redshifts and with different physical conditions populate the $L'_{\rm CO}$–$L_{\rm IR}$ parameter space and explore how the global $L'_{\rm CO}$–$L_{\rm IR}$ relation behaves with respect to the observed trends between $L_{\rm PAH}$–$L_{\rm IR}$ and $L_{\rm PAH}$–$L'_{\rm CO}$.

In Figure 2.4, we present the $L_{\rm IR}$–$L'_{\rm CO}$ relation for the 5MUSES sample along with the literature compilation included in Figure 2.3 (See Table 2.2). We also consider the $L_{\rm IR}$–$L'_{\rm CO}$ relation of Sargent et al. (2014) calibrated on MS galaxies with $M_*\geqslant 10^{10}$ M$_\odot$ at $0<z<3.2$ with a slope of 0.81 and a dispersion of 0.21 dex. The vast majority of SFGs, including our 5MUSES sample and the high-z SFGs appear to follow the Sargent relation. On the other hand, local ULIRGs and high-z SBs are outliers, a situation that resembles the $L_{6.2}$–$L_{\rm IR}$ and $L_{7.7}$–$L_{\rm IR}$ relations (Figure 2.3). In other words, sources exhibiting lower $L'_{\rm CO}/L_{\rm IR}$ ratios with respect to the general population of normal galaxies tend to also exhibit lower $L_{\rm PAH}/L_{\rm IR}$ ratios. In the next subsection, we bring these two together by exploring the relations between PAH and CO luminosities.

2.3.3 *The relations between CO and PAH emission*

In Figure 2.5, we plot the $L_{6.2}$ versus $L'_{\rm CO}$ (*left*) and $L_{7.7}$ versus $L'_{\rm CO}$ (*right*) luminosity relations for the 5MUSES sample as well as for the whole data set confirming the observed correlation between the PAH 6.2 µm and CO emission (Pope et al. 2013). The various populations appear to follow a unique relation, with a slope of unity within the uncertainties ($L_{6.2}$–$L'_{\rm CO}$: $\alpha = 1.03\pm0.06$ and $L_{7.7}$–$L'_{\rm CO}$: $\alpha = 1.04\pm0.08$), in agreement with the slightly

sub-linear slope ($\alpha = 0.9 \pm 0.01$) reported in Pope et al. (2013). The $L_{6.2}$–$L'_{\rm CO}$ and $L_{7.7}$–$L'_{\rm CO}$ relations have an intrinsic scatter of $\sigma = 0.26$ dex and $\sigma = 0.23$ dex respectively, without any specific SFG population standing out as prominent outliers. The shaded regions in the upper panels of Figure 2.5 depict the intrinsic scatter of $L_{6.2}$–$L'_{\rm CO}$ and $L_{7.7}$–$L'_{\rm CO}$ correlations assuming a slope of unity. In order to ensure that the linear slopes of the $L_{\rm PAH}$–$L'_{\rm CO}$ correlations are not affected by corrections applied to galaxies with higher-J CO observations, we fit only those galaxies with CO$(1-0)$ emission yielding a slope of $\alpha = 0.99 \pm 0.07$ consistent with the best fit of the full sample. The global PAH-CO luminosity relation for $L_{6.2}$ is parametrized as:

$$L_{6.2}\ [\mathrm{L}_\odot] = (0.39 \pm 0.18) \times \mathrm{L}'_{\rm CO}\ [\mathrm{K\ km\ s^{-1}\ pc^2}] \tag{2.2}$$

The universal $L_{6.2}$–$L'_{\rm CO}$ and $L_{7.7}$–$L'_{\rm CO}$ relations as indicated by our data suggest a link between the PAH and CO emission that appears unaffected by the physical conditions of the galaxies. Since the CO emission is a tracer of the gas mass and thus of the cold dust emission, a natural consequence of the $L_{\rm PAH}$–$L'_{\rm CO}$ is a link between the PAH and the cold dust emission of a galaxy. This is explored in detail in the following section.

2.3.4 *The relation between PAH and dust emission*

In the previous section, we showed that the emission from PAHs on global scales correlate with CO$(1-0)$ luminosity over a wide range of redshifts and various galaxy types. This result suggests a link between the PAH emission and the $M_{\rm gas}$ of a galaxy. Since $M_{\rm gas}$ is a derived physical parameter rather than a direct observable, before exploring a possible $L_{\rm PAH}$–$M_{\rm gas}$ relation, it is informative to investigate the scaling relations and the scatter between $L_{\rm PAH}$ and the warm and the cold dust emission through MIR and FIR photometric bands. The motivation behind this exercise is that $M_{\rm gas}$ is known to be directly associated with the cold dust emission of galaxies (Leroy et al. 2011; Eales et al. 2012; Magdis et al. 2012b; Magdis et al. 2013; Scoville et al. 2017a), whereas the warm dust emission is linked to star formation. For the sake of brevity and clarity, we only present the results for the PAH 6.2 μm feature which is least affected by silicate absorption and extinction (Peeters, Spoon & Tielens 2004). However, the same applies to the PAH 7.7 μm feature due to the linear correlation between these two in logarithmic scales ($L_{6.2}$–$L_{7.7}$: $\alpha = 1.02 \pm 0.02$, see Table 2.5).

Using *Spitzer* and *Herschel* photometric observations of the 5MUSES sample, we derive monochromatic luminosities at 24, 160, 250, 350, and 500 µm (see Section 2.2.3) and plot them against $L_{6.2}$ in Figure 2.6 and 2.7, including galaxies with secure dust luminosities ($>3\sigma$). To minimize the effects of K-correction, we restrict our sample to a redshift range of $0.1 < z < 0.3$ ($\langle z \rangle = 0.12 \pm 0.05$). While $L_{6.2}$ is found to correlate with both the warm dust emission as traced by L_{24} as well as with the colder dust emission (at L_{160}, L_{250}, L_{350}, and L_{500}), we obtain a lower scatter for the latter, even when AGNs are excluded from the fit. We note that quite naturally galaxies with the presence of an AGN appear as prominent outliers only in the $L_{6.2}$–L_{24} relation due to the intrinsic AGN dust emission that peaks between rest frame 15 and 60 µm (Mullaney et al. 2011), boosting the L_{24} (for fixed $L_{\rm IR}$) with respect to star-formation dominated galaxies.

The correlation between the cold dust and PAH emission has been supported by various spatially resolved observations of local galaxies. For example, using *Spitzer* observations of local normal galaxies, Bendo et al. (2008) find the PAH emission to be well correlated with the 160 µm emission on spatial scales of $\sim$ 2 kpc, and a significant scatter in the relation between PAH and 24 µm emission, concluding that the PAHs are associated with the diffuse, cold dust. Similar results, based on SMC observations, were reached by Sandstrom et al. (2010) and Sandstrom et al. (2012), who also reported a strong correlation between the PAH and CO(1 – 0) emission. Furthermore, Haas, Klaas & Bianchi (2002), find a good spatial coincidence between the 850 µm continuum emission and the strength of the PAH 7.7 µm line, suggesting again that the PAH carriers are preferentially related to the regions dominated by cold dust and molecular clouds, where they are excited mainly by the interstellar radiation field.

These findings are also in agreement with recent modelling studies of the various dust components within [H II] regions and their surrounding envelopes (Pavlyuchenkov et al. submitted; see also Akimkin et al. 2015; Akimkin et al. 2017). They argue for a lower correlation between PAHs and graphite grains, responsible for the majority of the dust emission at 24 µm, due to possible destruction of PAHs within the [H II] regions. By modelling the intensity distributions of the different dust components, they find similar intensity distributions between PAHs and silicates that are the dominant dust component at $\sim 100 - 500$ µm. This could indicate that PAHs located in the

molecular clouds are excited by escaping UV photons from the [H II] regions (Pavlyuchenkov et al. submitted).

Put together, our analysis suggests that on global integrated scales PAH emission is linked to the cold dust and the CO emission in our sample, both of which are tracers of the molecular gas.

2.3.5 *The $L_{6.2}$–M_{H_2} relation in MS galaxies*

The total molecular gas mass can be estimated from the observed CO luminosity, assuming a CO–H_2 conversion factor, α_{CO}: $M_{H_2}[M_\odot]=\alpha_{CO}\times L'_{CO}$. Corollary, the linear relation between $L_{6.2}$ and L'_{CO} ratio presented in the previous section, can be used to convert $L_{6.2}$ to molecular gas masses. Using the median $L_{6.2}/L'_{CO}$ ratio of $(0.37 \pm 0.18)\ L_\odot/(K\,km\,s^{-1}\,pc^2)$ as indicated by our data, we define:

$$M_{H_2}\ [M_\odot] = \alpha_{CO} \times (2.7 \pm 1.3) \times L_{6.2} \tag{2.3}$$

However, both observational and theoretical studies suggest that α_{CO} varies with specific properties of the ISM, including metallicity and galaxy

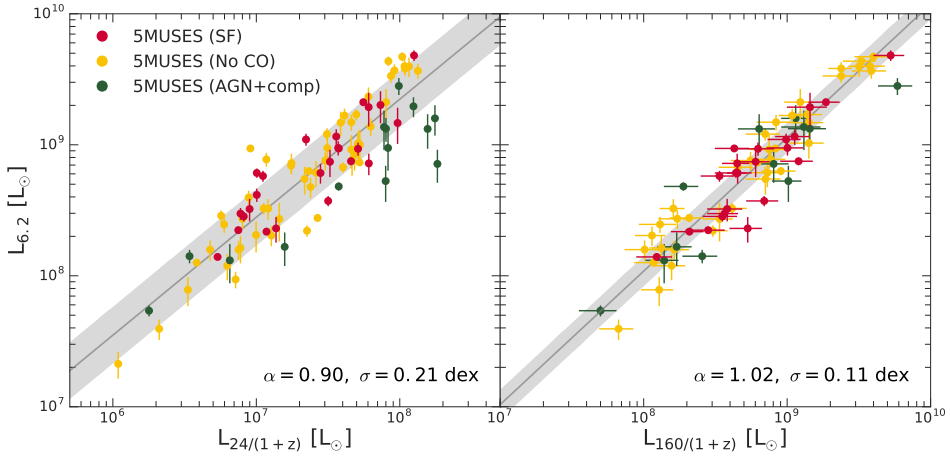

Figure 2.6: Correlation between $L_{6.2}$ and the 24 µm (*left*) and 160 µm luminosity (*right*) for the 5MUSES sample. Colour coding follow Figure 2.3. The dark grey line depicts the best linear regression fit to the 5MUSES sample and the 1σ dispersion of the correlation presented as the shaded region. Note the reduced intrinsic scatter of the $L_{6.2}$–L_{160} relation as opposed to $L_{6.2}$–L_{24} and the fact that AGN/composite sources are clear outliers in the $L_{6.2}$–L_{24} relation. The fit parameters are listed in Table 2.5.

Table 2.5: Linear scaling relations between the emission from PAHs, IR, and CO, and various galaxy properties.

$\log x$	$\log y$	α	β	σ	Sample
$L_{\rm IR}$ [$L_\odot$]	$L_{6.2}$ [$L_\odot$]	0.98 ± 0.03	-1.89 ± 0.30	0.13	SFGs
$L_{\rm IR}$ [$L_\odot$]	$L_{6.2}$ [$L_\odot$]	0.81 ± 0.03	-0.04 ± 0.29	0.21	All
$L_{\rm IR}$ [$L_\odot$]	$L_{7.7}$ [$L_\odot$]	1.00 ± 0.03	-1.53 ± 0.28	0.13	SFGs
$L_{\rm IR}$ [$L_\odot$]	$L_{7.7}$ [$L_\odot$]	0.84 ± 0.02	-0.15 ± 0.26	0.20	All
$L'_{\rm CO}$ [$\rm K\,km\,s^{-1}\,pc^2$]	$L_{6.2}$ [$L_\odot$]	1.02 ± 0.06	-0.65 ± 0.31	0.24	SFGs
$L'_{\rm CO}$ [$\rm K\,km\,s^{-1}\,pc^2$]	$L_{6.2}$ [$L_\odot$]	1.03 ± 0.06	-0.73 ± 0.38	0.26	All
$L'_{\rm CO}$ [$\rm K\,km\,s^{-1}\,pc^2$]	$L_{6.2}$ [$L_\odot$]	0.99 ± 0.07	-0.37 ± 0.70	0.24	With CO(1 – 0)
$L'_{\rm CO}$ [$\rm K\,km\,s^{-1}\,pc^2$]	$L_{7.7}$ [$L_\odot$]	1.03 ± 0.08	-0.13 ± 0.19	0.21	SFGs
$L'_{\rm CO}$ [$\rm K\,km\,s^{-1}\,pc^2$]	$L_{7.7}$ [$L_\odot$]	1.04 ± 0.08	-0.21 ± 0.20	0.23	All
L_{24} [$L_\odot$]	$L_{6.2}$ [$L_\odot$]	0.99 ± 0.05	1.51 ± 0.37	0.20	5MUSES SFGs
L_{24} [$L_\odot$]	$L_{6.2}$ [$L_\odot$]	0.90 ± 0.05	2.14 ± 0.35	0.21	5MUSES
L_{160} [$L_\odot$]	$L_{6.2}$ [$L_\odot$]	1.02 ± 0.04	-0.11 ± 0.37	0.11	5MUSES
L_{250} [$L_\odot$]	$L_{6.2}$ [$L_\odot$]	0.87 ± 0.04	1.48 ± 0.31	0.17	5MUSES
L_{350} [$L_\odot$]	$L_{6.2}$ [$L_\odot$]	0.87 ± 0.05	1.83 ± 0.38	0.19	5MUSES
L_{500} [$L_\odot$]	$L_{6.2}$ [$L_\odot$]	0.83 ± 0.06	2.34 ± 0.42	0.17	5MUSES
$L_{6.2}$ [$L_\odot$]	$L_{7.7}$ [$L_\odot$]	1.00 ± 0.02	0.62 ± 0.13	0.01	5MUSES
L_{24} [$L_\odot$]	$L_{7.7}$ [$L_\odot$]	0.97 ± 0.05	2.15 ± 0.37	0.21	5MUSES SFGs
L_{24} [$L_\odot$]	$L_{7.7}$ [$L_\odot$]	0.79 ± 0.05	3.46 ± 0.40	0.28	5MUSES
L_{160} [$L_\odot$]	$L_{7.7}$ [$L_\odot$]	1.04 ± 0.04	0.23 ± 0.37	0.12	5MUSES
L_{250} [$L_\odot$]	$L_{7.7}$ [$L_\odot$]	0.87 ± 0.04	2.03 ± 0.3	0.19	5MUSES
L_{350} [$L_\odot$]	$L_{7.7}$ [$L_\odot$]	0.85 ± 0.05	2.45 ± 0.40	0.22	5MUSES
L_{500} [$L_\odot$]	$L_{7.7}$ [$L_\odot$]	0.82 ± 0.06	3.00 ± 0.48	0.22	5MUSES
$L_{6.2}$ [$L_\odot$]	$L_{7.7}$ [$L_\odot$]	1.00 ± 0.02	0.62 ± 0.13	0.01	5MUSES
$L_{6.2}$ [$L_\odot$]	$L_{7.7}$ [$L_\odot$]	1.02 ± 0.02	0.36 ± 0.19	0.06	All
$L_{6.2}$ [$L_\odot$]	$M_{\rm H_2}$[a] [$M_\odot$]	1.00 (fixed)	1.10 ± 0.01	0.28	5MUSES MS SFGs[b]
$L_{7.7}$ [$L_\odot$]	$M_{\rm H_2}$[a] [$M_\odot$]	1.00 (fixed)	0.55 ± 0.02	0.28	5MUSES MS SFGs[b]

Notes. The linear fits are obtained in the logarithmic space : $\log y = \alpha \times \log x + \beta$. The best-fitting parameters and the intrinsic scatter are estimated from the Bayesian linear regression method described in Kelly (2007).
[a]Dust-derived molecular gas masses assuming solar metallicity.
[b]With $\log(M_*/M_\odot) > 10$.

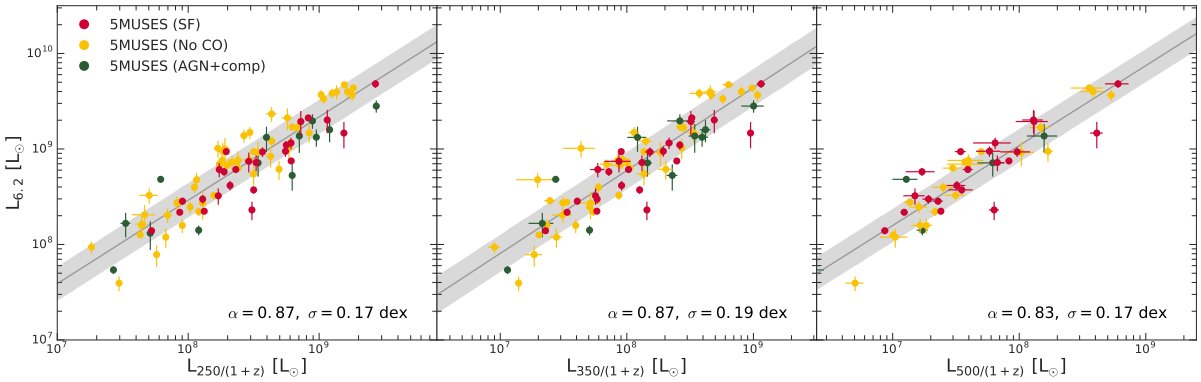

Figure 2.7: Correlation between $L_{6.2}$ and the 250 µm (*left*), 350 µm (*middle*), and 500 µm luminosity (*right*) for the 5MUSES sample. The fit parameters are listed in Table 2.5.

morphology (e.g. Leroy et al. 2011; Narayanan et al. 2012; Papadopoulos et al. 2012; Sandstrom et al. 2013), ranging between $\langle\alpha_{\rm CO}\rangle \approx 4.5\,{\rm M}_\odot\,({\rm K\,km\,s^{-1}\,pc^2})^{-1}$ for normal MS galaxies and $\langle\alpha_{\rm CO}\rangle \approx 0.8\,{\rm M}_\odot\,({\rm K\,km\,s^{-1}\,pc^2})^{-1}$ for local ULIRGs and high-z SBs (e.g.. Solomon et al. 1987; Tacconi et al. 2006; Tacconi et al. 2008; Daddi et al. 2010b; Leroy et al. 2011; Magdis et al. 2011; Magdis et al. 2012b; Casey, Narayanan & Cooray 2014).

To avoid the dependency on $\alpha_{\rm CO}$, we derive molecular gas mass estimates using the FIR dust continuum observations. This method relies on the fact that $M_{\rm gas}$ can be derived from the dust mass by exploiting the well-calibrated gas-to-dust mass ratio ($\delta_{\rm GDR}(Z)$) (e.g. Leroy et al. 2011; Magdis et al. 2012b; Berta et al. 2016; Tacconi et al. 2018):

$$\delta_{\rm GDR} \times M_{\rm dust} \equiv M_{\rm gas} = M_{\rm H_I} + M_{\rm H_2} \tag{2.4}$$

where $M_{\rm H_I}$ is the atomic gas mass. Although the atomic-to-molecular gas ratio is not known at high redshift, current models suggest $M_{\rm H_2}$ dominates over $M_{\rm H_I}$ at high-z and high stellar surface densities (e.g. Blitz & Rosolowsky 2006; Obreschkow et al. 2009) and thus $M_{\rm gas}{\approx}M_{\rm H_2}$. Since the method is metallicity dependent, and in the absence of direct metallicity estimates, we choose to restrict our sample to massive galaxies with $\log(M_*/{\rm M}_\odot)> 10$ that are known to follow the mass-metallicity relation as well as the FMR relation (e.g.. Mannucci et al. 2010) at least out to $z \sim 2$. Moreover, whether SB systems, like local ULIRGs, follow the FMR relation or whether they are more metal-rich with respect to normal galaxies at fixed stellar mass is still

an open debate (e.g.. Magdis et al. 2011; Magdis et al. 2012b; Silverman et al. 2015; Pereira-Santaella et al. 2017; Rigopoulou et al. 2018). To avoid the uncertainties and systematics introduced by the metallicity of SB galaxies, we choose to omit them from our analysis in this section. Instead, we focus on massive MS galaxies from the 5MUSES sample with sufficient FIR coverage (out to $\lambda_{\rm rest} > 250$ μm to ensure robust $M_{\rm d}$ estimates).

Molecular gas masses are then inferred using the $\delta_{\rm GDR} - Z$ metallicity relation: $\log \delta_{\rm GDR} = (10.54 \pm 1.0) - (0.99 \pm 0.12) \times (12 + \log({\rm O/H}))$ from Magdis et al. (2012b). The resulting $M_{\rm H_2}$ estimates versus $L_{6.2}$ are presented in 2.8, yielding:

$$\log\left(\frac{\rm M_{H_2}}{\rm M_\odot}\right) = \log\left(\frac{\rm L_{6.2}}{\rm L_\odot}\right) + (1.10 \pm 0.02) \tag{2.5}$$

with an intrinsic scatter of $\sigma = 0.28$ dex. As a sanity check, we also overplot the $M_{\rm H_2}$–$L_{6.2}$ relation using equation 3, adopting $\alpha_{\rm CO}$= 4.5 $\rm M_\odot\,(K\,km\,s^{-1}\,pc^2)^{-1}$, a typical value for normal SFGs. Indeed, we see that this relation is in excellent agreement with our data, reassuring that both the dust-based $M_{\rm H_2}$ estimates and the $L'_{\rm CO}$-based $M_{\rm H_2}$ estimates with $\alpha_{\rm CO}$= 4.5 $\rm M_\odot\,(K\,km\,s^{-1}\,pc^2)^{-1}$ are consistent. Finally, we overplot equation 3 assuming $\alpha_{\rm CO}$= 0.8 $\rm M_\odot\,(K\,km\,s^{-1}\,pc^2)^{-1}$ to indicate the expected location of SBs in Figure 2.8. An attempt to explain the physical origin of the derived $L_{6.2}$–$M_{\rm H_2}$ relation and a discussion of its importance and limitations are presented in the following section.

2.4 DISCUSSION

In the previous sections, we have explored the global scaling laws between $L_{6.2}$, $L'_{\rm CO}$, and $L_{\rm IR}$ for a large compilation of different galaxy populations at various redshifts. We have seen that variations in the $L_{6.2}/L_{\rm IR}$ and $L'_{\rm CO}/L_{\rm IR}$ ratios among different galaxy populations are not permeated in their $L_{6.2}/L'_{\rm CO}$ ratios that instead appear to be rather constant through a universal $L_{6.2}$–$L'_{\rm CO}$ relation with a slope of unity.

This is further demonstrated in Figure 2.9. While the distribution of the $\log(L_{6.2}/L'_{\rm CO})$ ratios is symmetric around the central value, we find a negatively skewed distribution of the $\log(L_{6.2}/L_{\rm IR})$ ratios. This skewness is driven by systematically lower $\log(L_{6.2}/L_{\rm IR})$ ratios of local ULIRGs. In fact, we find a 8.70σ significant difference between the mean values of $\log(L_{6.2}/L_{\rm IR})$

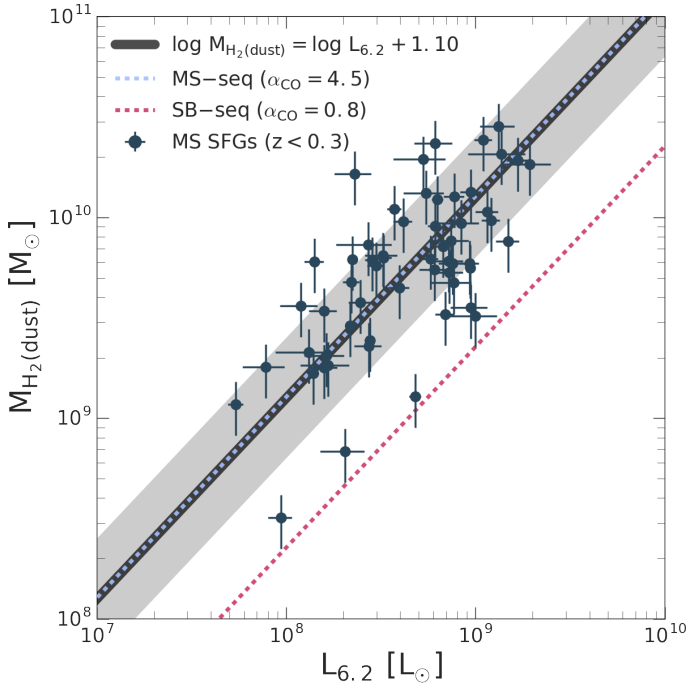

Figure 2.8: Correlation between $L_{6.2}$ and dust-derived molecular gas mass (M_{H_2}) for normal galaxies assuming solar metallicity. The sample includes 5MUSES MS galaxies at $z < 0.3$ with $\log(M_*/M_\odot) > 10$. The black line corresponds to the best fit with a fixed slope of 1 with an intrinsic scatter of 0.30 dex (grey shaded region). Light blue and red dashed lines are the M_{H_2}–L'_{CO} relation for MS and SB galaxies adopting $\alpha_{CO} = 4.5\ M_\odot\,(K\,km\,s^{-1}\,pc^2)^{-1}$ and $\alpha_{CO} = 0.8\ M_\odot\,(K\,km\,s^{-1}\,pc^2)^{-1}$, respectively.

for the local ULIRGs (-2.68 ± 0.06) and the 5MUSES SFGs (-2.11 ± 0.03). On the other hand, we do not find any significant systematic variations in the $\log(L_{6.2}/L'_{CO})$ ratios (ULIRGs: 0.36 ± 0.06, 5MUSES SFGs: 0.44 ± 0.04). This suggests that $L_{6.2}$ is, in fact, a better tracer of CO (and thus of M_{H_2}) than the total IR emission.

While the emerging PAH–CO luminosity relation has also been reported in spatially resolved observation of local galaxies, its physical origin (if any) is still debated. Bendo et al. (2010) suggest that the correlation between PAH and CO emission observed in NGC 2403 on large scales can be explained if they share similar excitation mechanisms, or if the molecular cloud formation is triggered in regions with stellar potential wells as described in Leroy et al. (2008). For the latter, CO emission could then arise from newly formed molec-

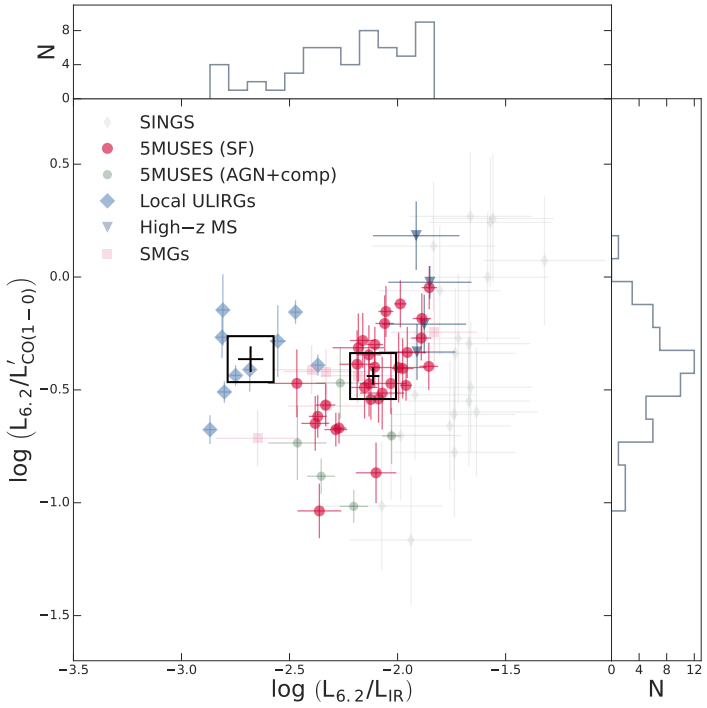

Figure 2.9: $\log(L_{6.2}/L'_{\rm CO})$ versus $\log(L_{6.2}/L_{\rm IR})$ for the full sample with both PAH and CO emission. Colour coding and symbols follow Figure 2.3. The black open squares correspond to the median values for the 5MUSES SFGs and the local ULIRGs. The top and right panels show the distribution of $L_{6.2}/L_{\rm IR}$ and $L_{6.2}/L'_{\rm CO}$, respectively.

ular clouds, while starlight in the potential wells would heat surrounding regions enhancing the PAH emission. This scenario would also explain the variations between PAH and CO emission on sub-kpc scales and the similar radial profiles on larger spatial scales (Regan et al. 2006). Finally, recent studies have suggested that in dense PDRs, PAHs may be responsible for a significant fraction of the H_2 formation at a rate comparable to that of H_2 formation on dust grains (Castellanos et al. 2018b; Castellanos et al. 2018a). If so, a correlation between PAHs and $M_{\rm H_2}$ could thus be expected.

The CO–PAH luminosity relation is not the only piece of evidence for a potential link between $L_{6.2}$ and $M_{\rm H_2}$. In Section 2.3.5, we used CO-independent $M_{\rm H_2}$ estimates through the $\delta_{\rm GDR} - Z$ technique and found a linear $L_{6.2}$–$M_{\rm H_2}$ relation for normal SFGs. The relation in eq. 2.5 can then be used to define: $M_{\rm H_2}$=$\alpha_{6.2}$×$L_{6.2}$ where $\alpha_{6.2}$ is the parameter converting $L_{6.2}$ to $M_{\rm H_2}$. The in-

ferred $\alpha_{6.2}$ conversion factor of our sample of MS galaxies are shown in Figure 2.10 (*left*). It appears that $\alpha_{6.2}$ is independent of redshift for MS galaxies with an average value of $\langle \log(\alpha_{6.2}) \rangle = 1.09$ and a standard deviation of 0.30 (Figure 2.10 *right*). An obvious caveat for the derivation of $M_{\rm H_2}$ from $L_{6.2}$ similar to the $\delta_{\rm GDR}$ and CO technique, is the dependence on metallicity which becomes challenging especially for SB systems and low-mass galaxies. For speculation, we overplot local ULIRGs in Figure 2.10 (*left*) inferring their $M_{\rm H_2}$ estimates from $L'_{\rm CO}$ and assuming the commonly adopted $\alpha_{\rm CO}$= 0.8 $\rm M_\odot (K\,km\,s^{-1}\,pc^2)^{-1}$. Naturally, lower $\alpha_{\rm CO}$ values lead to lower $\alpha_{6.2}$ values for SB systems.

With the upcoming launch of the *James Webb Space Telescope* (*JWST*), PAH features will be detected and spatially resolved with MIRI out to $z \sim 3.5$. Our analysis suggests that PAHs can be used as a tool to infer the total amount and the spatial distribution of the molecular gas in systems that will probably be too faint to be detected by *Herschel* and thus lack any FIR photometric coverage. Since the most prominent and bright PAH feature is the one at 7.7 μm, it is worth to present its scaling relation with $M_{\rm H_2}$ as well. Repeating our analysis using $L_{7.7}$, we then find:

$$\log\left(\frac{M_{\rm H_2}}{M_\odot}\right) = \log\left(\frac{\rm L_{7.7}}{\rm L_\odot}\right) + (0.55 \pm 0.02) \tag{2.6}$$

with an intrinsic dispersion of 0.28 dex.

2.5 CONCLUSIONS

We have presented 24 new CO(1−0) observations of intermediate redshift ($0.03 < z < 0.30$) SFGs drawn from the 5MUSES sample that also benefits from existing *Spitzer* IRS spectroscopy and FIR photometry observations from *Spitzer* and *Herschel*. Complementing our study with literature CO, PAH, and dust observations, we investigate scaling relations between the various components of the ISM of galaxies covering a wide range of redshifts and physical conditions. We summarize our conclusions as follows:

(i) We confirm the existence of a correlation between the PAH and CO emission on global integrated scales and for the first time determine its slope and scatter in a robust statistical way. The linear and tight $L_{6.2}$–$L'_{\rm CO}$ correlation (slope of ~ 1.0 and intrinsic scatter $\sigma = 0.26$ dex) is followed by the majority of galaxies at all redshifts, independent of the galaxy type.

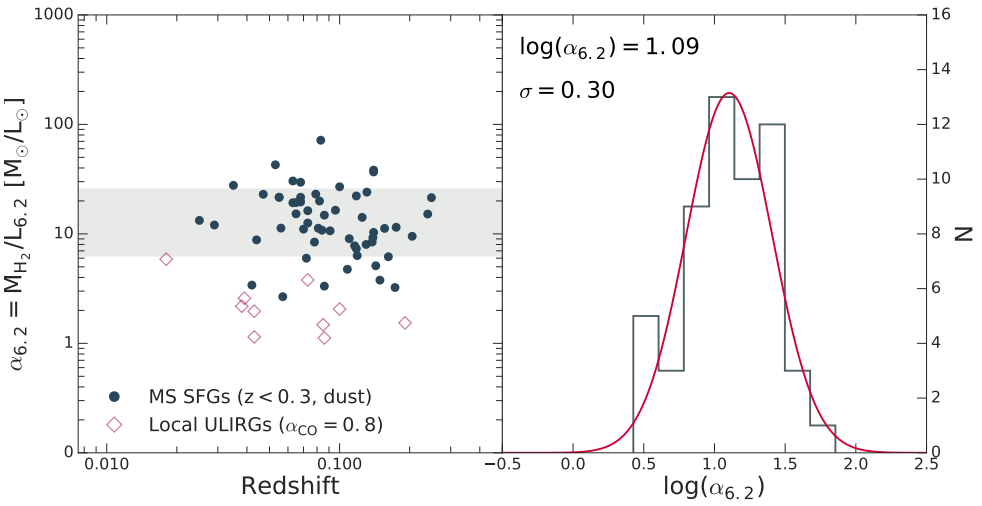

Figure 2.10: *Left*: Correlation between the $\alpha_{6.2}$ conversion factor versus redshift. The sample includes dust-derived $M_{\rm gas}$ estimates of 5MUSES MS galaxies at $z < 0.3$ (dark blue). The grey region depicts the average $\alpha_{6.2}$ value of the sample and the 1σ dispersion. We overplot local ULIRGs (red) assuming $\alpha_{\rm CO}$= 0.8 $\rm M_\odot (K\,km\,s^{-1}\,pc^2)^{-1}$. *Right*: Distribution of $\log(\alpha_{6.2})$ for the 5MUSES MS galaxies. The red line corresponds to the best-fitting Gaussian profile to the data with a mean value of 1.09 and a standard deviation σ = 0.30.

(ii) We find evidence that on galaxy integrated scales, $L_{6.2}$ traces better the cold dust ($\lambda > 100$ µm) rather than the warm dust emission ($\lambda = 24$ µm). This is in agreement with spatially resolved observations of local galaxies. The fact that both CO and cold dust emission are tracing molecular gas, motivates us to propose that PAHs may serve as a gas tracer in SFGs.

(iii) We define a $\alpha_{6.2} = M_{\rm H_2}/L_{6.2}$ conversion factor of 2.7× $\alpha_{\rm CO}$, where $\alpha_{\rm CO}$ is the $L'_{\rm CO}$ to $M_{\rm H_2}$ conversion factor. For normal SFGs we find $\alpha_{6.2} = 12.30\,\rm M_\odot/L_\odot$ (σ = 0.30 dex), which is consistent with $\alpha_{\rm CO} \approx 4.5\ \rm M_\odot (K\,km\,s^{-1}\,pc^2)^{-1}$, typical of normal SFGs.

We conclude that $L_{6.2}$ can effectively probe the molecular gas mass in galaxies within a factor of ~ 2 and propose that with the launch of *JWST*, PAHs could serve as a useful tool to trace the ISM properties in SFGs up to $z \sim 3.5$.

ACKNOWLEDGEMENTS

IC acknowledges support from Villum Fonden research grant (13160). GEM acknowledges support from the Carlsberg Foundation and a research grant (13160) from Villum Fonden. GEM, ST, CGC, and MS acknowledge support from the ERC Consolidator Grant funding scheme (project ConTExt, grant number No. 648179. This work includes observations carried with the IRAM 30m telescope, which is supported by INSU/CNRS (France), MPG (Germany) and IGN (Spain). The Cosmic Dawn Center is funded by the Danish National Research Foundation.

SUPPORTING INFORMATION

Supplementary data are available at MNRAS online.

Table 3. General properties of the 5MUSES sample (available in the appendix A.1).
Table 4. Galaxies from the literature with PAH, IR, and/or CO emission (available in the appendix A.2).

Please note: Oxford University Press is not responsible for the content or functionality of any supporting materials supplied by the authors. Any queries (other than missing material) should be directed to the corresponding author for the article.

CHAPTER 3

Are high-redshift starbursts cold?

This chapter contains the following article:
"Deceptively cold dust in the massive starburst galaxy GN20 at $z \sim 4$"

Published as a letter in Astronomy & Astrophysics (A&A): Vol. 634, L14, 2020.

Authors: Isabella Cortzen, Georgios E. Magdis, Francesco Valentino, Emanuele Daddi, Daizhong Liu, Dimitra Rigopoulou, Mark Sargent, Dominik Riechers, Diane Cormier, Jacqueline A. Hodge, Fabian Walter, David Elbaz, Matthieu Bethermin, Thomas R. Greve, Vasily Kokorev & Sune Toft.

ABSTRACT

We present new observations, carried out with IRAM NOEMA, of the atomic neutral carbon transitions [C I]($^3P_1$–$^3P_0$) at 492 GHz and [C I]($^3P_2$–$^3P_1$) at 809 GHz of GN20, a well-studied star-bursting galaxy at $z = 4.05$. The high luminosity line ratio [C I]($^3P_2$–$^3P_1$) /[C I]($^3P_1$–$^3P_0$) implies an excitation temperature of 48^{+14}_{-9} K, which is significantly higher than the apparent dust temperature of $T_{\rm d}$=33 ± 2 K (β = 1.9) derived under the common assumption of an optically thin far-infrared dust emission, but fully consistent with $T_{\rm d}$= 52 ± 5 K of a general opacity model where the optical depth (τ) reaches unity at a wavelength of λ_0 = 170 ± 23 µm. Moreover, the general opacity solution returns a factor of ∼ 2× lower dust mass and, hence, a lower molecular gas mass for a fixed gas-to-dust ratio, than with the optically thin dust model. The derived properties of GN20 thus provide an appealing solution to the puzzling discovery of starbursts appearing colder than main-sequence galaxies above $z > 2.5$, in addition to a lower dust-to-stellar mass ratio that approaches the physical value predicted for starburst galaxies.

3.1 INTRODUCTION

Over the last decade, it has been established that the majority of star-forming galaxies (SFGs) fall into a tight correlation between the star formation rate (SFR) and the stellar mass (M_*), forming a "main-sequence" (MS) with a normalization that increases with redshift (e.g., Brinchmann et al. 2004; Daddi et al. 2007; Noeske et al. 2007; Elbaz et al. 2007; Magdis et al. 2010). Outliers of this relation are defined as starburst galaxies (SBs), existing at all redshifts. While the star formation in MS galaxies is governed by secular processes, merger-induced events or galaxy interactions are thought to trigger it in SBs (e.g., Cibinel et al. 2019).

In the interstellar medium (ISM), the thermal emission from dust grains heated by UV photons originating from newly formed stars dominates the spectral energy distribution (SED) of galaxies (at ∼ 8 – 1000 µm, Sanders & Mirabel 1996). Modeling of the rest-frame far-infrared (FIR) and the Rayleigh-Jeans (RJ) tail of the SED can be used to derive properties including the dust mass ($M_{\rm d}$), the infrared luminosity ($L_{\rm IR}$), the intensity of the radiation field ($\langle {\rm U} \rangle \propto L_{\rm IR}/\ M_{\rm d}$: Draine & Li 2007), and the mass-weighted dust temperature ($T_{\rm d}$) where $\langle {\rm U} \rangle = (T_{\rm d}/18.9)^{6.04}$ (Magdis et al. 2012b; Magdis et al. 2017).

With the ever-increasing number of galaxy populations with well-studied infrared properties, several puzzling findings have started to emerge, especially for high-redshift SBs. First, their dust-to-stellar mass ratios ($M_{\rm d}/M_*$) are found to be extremely large (reaching 0.1: Tan et al. 2014), with a stellar mass budget that is unable to account for the inferred dust production (Béthermin et al. 2015). Second, while the intensity of the radiation field in MS galaxies rises with increasing redshift up to $z \sim 4$ (Magdis et al. 2017; Jin et al. 2019), mirroring the increase in the specific star formation rate (sSFR=SFR/M_*) in the same time interval (Béthermin et al. 2015 for $T_{\rm d}$: Schreiber et al. 2018), the evolution is less clear for SBs. While Schreiber et al. (2018) report a trend of increasing $T_{\rm d}$ with both redshift and offset from the MS, the latter, independently of redshift, Béthermin et al. (2015) observe no evolution of the mean radiation field (hence, dust temperature) with redshift for strong SBs with sSFR $> 10 \times$ sSFR$_{\rm MS}$, which become apparently colder than MS galaxies at $z > 2.5$, which is at odds with the expectations. A possible solution to the latter could be offered by a more general treatment of the modeling of the FIR emission that in the vast majority of the literature. Also, due to the limited sampling of the SEDs in the FIR to RJ regime, such modeling is performed under the assumption of optically thin FIR emission for both MS and SB galaxies. Indeed, observational studies of local ultra-luminous infrared galaxies (ULIRGs) and high-redshift massive SBs indicate that the dust could remain optically thick out to rest-frame $\lambda_0 = 100 - 200\,\mu$m (e.g., Blain, Barnard & Chapman 2003; Huang et al. 2014; Lutz et al. 2016; Spilker et al. 2016; Riechers et al. 2013; Hodge et al. 2016; Simpson et al. 2017) and, in the most extreme case, out to millimeter wavelengths as reported for the star-bursting nucleus of Arp 220 (Scoville et al. 2017b). If the FIR dust emission is optically thick, the suppressed continuum emission in the Wien's part of the IR emission shifts the peak of the SED to longer wavelengths, mimicking apparently cold $T_{\rm d}$, while, in fact, the actual luminosity-weighted $T_{\rm d}$ of the sources would be considerably warmer. The main difficulty is that the optically thin or thick solutions are heavily degenerate; the same SED could arise from either cold and optically thin or a warm and optically thick FIR dust emission with no robust way to discriminate between the two by simply using continuum observations. An independent proxy for $T_{\rm d}$ is, thus, required to break this degeneracy.

In this work, we present new Northern Extended Millimeter Array (NOEMA)

observations of GN20, a well-known massive (stellar mass of $M_*\sim 10^{11}\,M_\odot$: Tan et al. 2014) starburst galaxy at $z = 4.0553$ (Pope et al. 2006; Daddi et al. 2009), targeting both atomic neutral carbon lines, [C I]($^3P_1 - {}^3P_0$) and [C I]($^3P_2 - {}^3P_1$). The simple three-level structure of the atom allows us to use the [C I] line luminosity ratio to derive the excitation temperature (T_{ex}), which was recently reported to correlate with T_d derived assuming optically thin FIR dust emission on sub-galactic scales for nearby (U)LIRGs (Jiao et al. 2019b; Jiao et al. 2019a), suggesting that the gas probed by [C I] and the dust are correlated on kpc scales. The [C I] line ratio might thus be used as an independent empirical indicator of the dust temperature, potentially breaking the degeneracy between an optically thick and thin case for the FIR dust emission.

Throughout the paper, we adopt $H_0 = 70\,\mathrm{km\,s^{-1}\,Mpc^{-1}}$, $\Omega_M = 0.30$, $\Omega_\Lambda = 0.70$, and a Chabrier (2003) initial mass function (IMF).

3.2 OBSERVATIONS AND DATA REDUCTION

We used IRAM NOEMA to observe the [C I]($^3P_1 - {}^3P_0$), [C I]($^3P_2 - {}^3P_1$), and CO(7 – 6) line transitions in the GN20 protocluster (Daddi et al. 2009). The observations took place in March 2017 using the D configuration for a total on-source time of 7.6 hours (program W16DZ, PI: G. Magdis). The [C I]($^3P_1 - {}^3P_0$) line (rest frequency: $\nu_{rest} = 492.161$ GHz) is redshifted to $\nu = 97.355$ GHz at $z = 4.0553$ with a primary beam of 51.8″. We set our pointing center to the coordinates of GN20 (RA: 12h37m11.89s, DEC: +62d22m12.1s) to detect the [C I] and CO lines in this galaxy. Although the D-configuration leads to a relatively low spatial resolution (~3–6″), it is the most suitable configuration for a detection experiment as ours. As the observations of the two other GN20 protocluster members, GN20.2a and GN20.2b, are affected by a primary beam attenuation of about 0.2 – 0.7, no lines were detected and we could not derive any constraining measurements for these galaxies.

The data were reduced using the GILDAS software packages CLIC and MAPPING. The pipeline-derived flux for our flux calibrator LKHA101 is 0.24 Jy at 97.4 GHz, and 0851 + 202 7.24 Jy at 160.1 GHz, with about 20% absolute calibration uncertainty. We produced *uv* tables with channel widths of $26\,\mathrm{km\,s^{-1}}$, achieving an rms of 0.77 and $1.35\,\mathrm{mJy\,beam^{-1}}$ at 3 mm and 1.86 mm, respectively. We then estimated the continuum emission by averaging the line-free channels. Finally, we subtracted the continuum to produce the line *uv* tables. The spectra were then extracted using the GILDAS *UV_FIT* task by

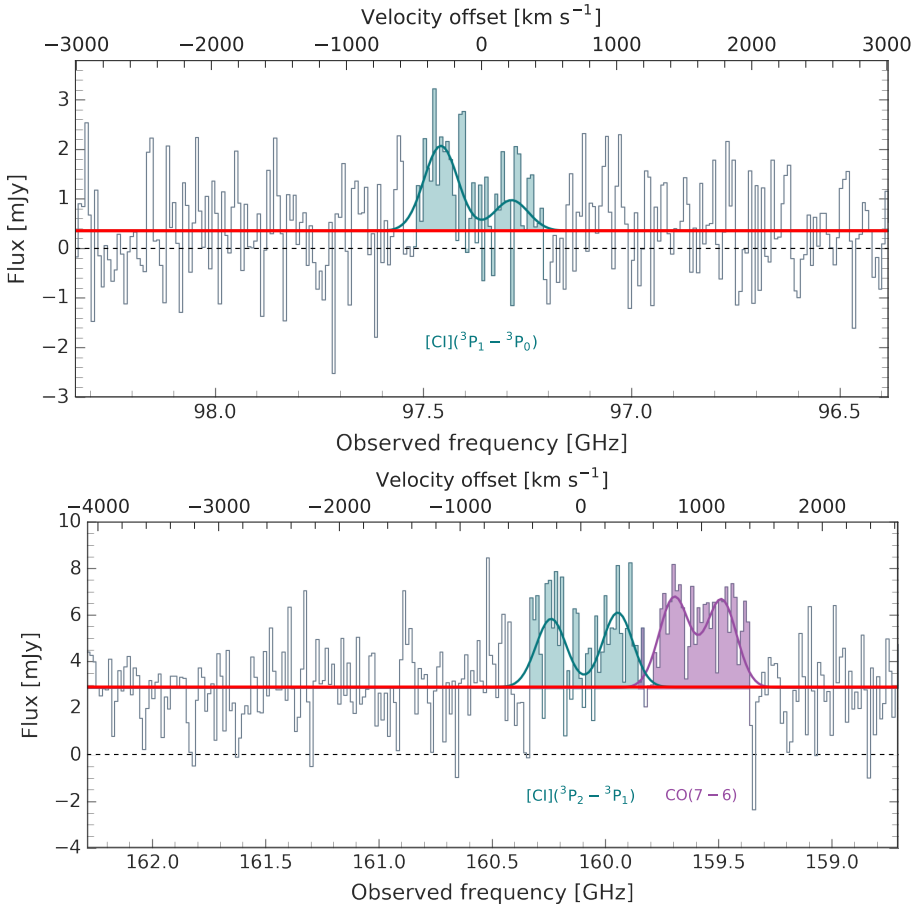

Figure 3.1: Extracted spectra of the [C I]($^3P_1 - {}^3P_0$) line (*left*) and the [C I]($^3P_2 - {}^3P_1$) and CO(7 – 6) lines (*right*). Both spectra are binned in steps of 26 km s^{-1}. The colored areas indicate that the velocity ranges corresponding to detected line emission as labeled, which were used to obtain the velocity-integrated fluxes. Blue and purple solid lines show the best-fit double Gaussians, whereas the red line in each panel shows the continuum level. The velocity offset in both panels is relative to the expected frequency of the [C I] lines at $z = 4.0553$.

assuming an intrinsic source size of 0.72″ (circular Gaussian FWHM), the size of the CO(4 – 3) line derived from the higher-resolution and signal-to-noise (S/N) data from Tan et al. (2014). The beam sizes at 3 mm and 1.86 mm are 6.72″ × 3.42″ and 2.51″ × 1.72″, respectively. The CO and [C I] line intensity maps were produced by collapsing the *uv* space cube according to the line widths followed by an imaging process (dirty image). We extracted all information directly in the *uv* plane to avoid introducing any artifacts during the

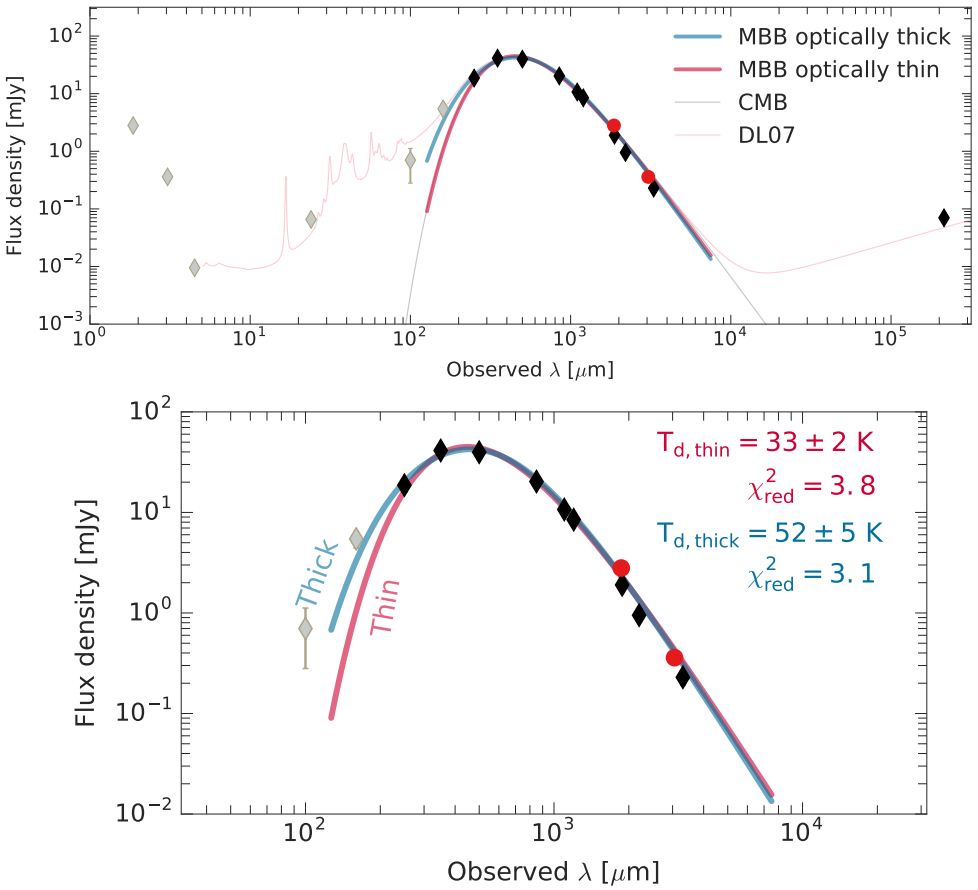

Figure 3.2: Mid-IR to millimeter SED of GN20 in observed wavelength. *Upper*: we complement our new continuum measurements at 1.86 and 3.05 mm (red points) with existing photometry observations at observed and $\lambda > 160\,\mu$m and $\lambda \leq 160\,\mu$m (black and grey points, respectively), where the latter is omitted from the MBB modeling. Blue and red lines show the best-fit single-temperature MBB prescription assuming an optically thick ($\lambda_0 = 170 \pm 23$ μm) and thin dust emission, respectively. We also present the best-fit MBB model when accounting for the effect of the CMB (grey curve). The solid pink line shows the best-fit using the DL07 dust models, containing a diffuse ISM component and dust in PDR regions. The best-fit MBB parameters are listed in Table 3.1. *Lower*: A zoom-in of the rest-frame FIR part of the SED of GN20 when including the optically thick and thin MBB prescriptions. We note that the optically thick MBB model is a better macth to the photometry observations at $\lambda \leq 160$ μm.

imaging process. We note that assuming an unresolved point-like source in

the fitting leads to ∼ 20% lower line fluxes and 50% worse residuals [1].

We searched for emission lines by scanning the S/N spectra as detailed in Daddi et al. (2015). The estimated continuum at 1.86 mm of GN20 is 2.80 ± 0.13 mJy and 0.36±0.04 mJy at 3.05 mm. The 1.86 mm continuum flux is larger than the existing measurements reported in Casey et al. (2009) ($S_{1.86\mathrm{mm}} = 1.9\pm 0.2$ mJy), for which the actual noise may have been underestimated. On the other hand, the 3.05 mm continuum flux (central frequency 98.16 GHz) is fully consistent with the flux reported in Tan et al. (2014) ($S_{3.3\mathrm{mm}} = 0.23 \pm 0.04$ mJy, central frequency 91.34 GHz) when taking into account the difference in frequency and assuming the dust continuum decreases as $\sim \lambda^{-3.8}$.

Figure 3.1 (*left*) shows the [C I]($^3P_1 - {}^3P_0$) spectrum with an indication of a double-peaked structure which is more prominent in the [C I]($^3P_2 - {}^3P_1$) and CO(7 – 6) lines (Figure 3.1, *right*). We fixed the line width as derived from the brighter [C I]($^3P_2 - {}^3P_1$) line (see Table 3.1) to estimate the [C I]($^3P_1 - {}^3P_0$) line flux. This is done for the purpose of including the fainter component of the [C I]($^3P_1 - {}^3P_0$) line feature which, due to the low S/N, would otherwise be overlooked. We detected the line with a 6.40σ significance, retrieving a total velocity-integrated flux of 0.70 ± 0.11 Jy km s^{-1}.

Existing [C I]($^3P_2 - {}^3P_1$) and CO(7 – 6) line observations of this target were previously reported as upper limits with line intensities of < 1.2 Jy km s^{-1} (Casey et al. 2009). However, our observations reveal 8.5σ and 11.0σ detections for the [C I]($^3P_2 - {}^3P_1$) and CO(7 – 6) emission, respectively. This could indicate that the previous [C I]($^3P_2 - {}^3P_1$) and CO(7 – 6) upper limits may have been underestimated, similarly to the continuum measurement at 1.86 mm. Figure 3.1 (*right*) shows the spectrum of [C I]($^3P_2 - {}^3P_1$) and CO(7 – 6), where the velocity offset is relative to the expected frequency at $z = 4.0553$. Both lines are detected and reveal a double-peaked structure. The total velocity-integrated flux density of the [C I]($^3P_2 - {}^3P_1$) line is 1.80 ± 0.22 Jy km s^{-1} with a line width of 949 km s^{-1}. The observed lines indicate a redshift of 4.0536 ± 0.0080 , which is consistent with previous redshift determinations from CO line measurements (Daddi et al. 2009; Carilli et al. 2010; Carilli et al. 2011; Hodge et al. 2012; Tan et al. 2014). The CO(7 – 6) flux measurements, along with a detailed study of the CO spectral line energy distribution (SLED), will be presented in a dedicated, forthcoming paper.

[1] This is estimated by examining the total flux within one beam size aperture at the position of GN20 in the dirty image of the line-channel-collapsed residual data. The residual *uv* data are produced by the GILDAS *UV_FIT* task.

The total integrated flux density of each line was estimated by taking the product of the averaged flux density in the channels, maximizing the S/N and the velocity width of these channels (see Daddi et al. 2015; Whitaker et al. 2014). We checked these non-parametric estimates against Gaussian modeling, retrieving fully consistent results. We proceeded with the scanning method based on the first approach to derive the line luminosities throughout the paper. The line fluxes were converted to luminosities (listed in Table 3.1) following the conversions in Solomon & Vanden Bout (2005).

3.3 ANALYSIS

3.3.1 *The excitation temperature of neutral atomic carbon*

Our new NOEMA observations allow us to derive the excitation temperature ($T_{\rm ex}$), under the assumption of local thermodynamical equilibrium (LTE) and given that both carbon lines are optically thin. To test the validity of the latter assumption, we derived the optical depth of each [C I] line following Schneider et al. (2003) (equation A.6 and A.7) by using the intrinsic brightness temperature of the [C I] lines. We used the optically thick FIR dust results ($\tau = 1$, $\lambda_0 = 170\,\mu$m, and $\log(M_{\rm d}/M_\odot) = 9.31$) to derive the source solid angle assuming $\kappa_{850} = 0.43\,{\rm cm^2\,g^{-1}}$ at $\lambda = 850\,\mu$m yielding $\Omega_{\rm source} = 2.36 \times 10^{-12}\,{\rm sr}$ or an effective radius of $R_{\rm e} = 1.2\,{\rm kpc}$, consistent with the reported size of the rest-frame 170 µm observations (Hodge et al. 2015). For the [C I]($^3P_1$ – $^3P_0$) and [C I]($^3P_2$ – $^3P_1$) lines, we measured brightness temperatures of $T_{\rm b} = 5.43$ and 5.15 K, respectively. As the equations include the excitation temperature, we assumed for the first iteration that $T_{\rm ex}$ is equal to $T_{\rm d} = 33{-}52\,{\rm K}$, the derived dust temperature assuming optically thin and thick dust MBB prescriptions, respectively (see Section 3.3.2). This yields optical depths of $\tau_{\rm [CI]} = 0.1 - 0.3$ for both [C I] lines, comparable with other high-redshift galaxies (Walter et al. 2011; Alaghband-Zadeh et al. 2013; Nesvadba et al. 2019). The excitation temperature can be derived via the formula under the assumption that [C I] is thermalized, meaning that it shares the same $T_{\rm ex}$ for both levels of [C I] (Stutzki et al. 1997):

$$T_{\rm ex} = 38.8 \times \ln\left(\frac{2.11}{R}\right)^{-1}, \tag{3.1}$$

where $R = L'_{\rm [CI](^3P_2-^3P_1)} \,/\, L'_{\rm [CI](^3P_1-^3P_0)}$. We find $R = 0.9{\pm}0.2$ and $T_{\rm ex} = 48.2{\pm}11.6$ K. We bootstrapped the [C I]($^3P_1$ – $^3P_0$) and [C I]($^3P_2$ – $^3P_1$) luminosities, assuming normally distributed values with the observed error as the standard

deviation. This Monte Carlo (MC) test yields a median of $T_{\rm ex} = 48.2^{+15.1}_{-9.2}$ K (the upper and lower values are the 16th and 84th percentiles). Lastly, re-deriving the optical depths using the final excitation temperature yields $\tau_{\rm [CI](1-0)} = 0.2$ and $\tau_{\rm [CI](2-1)} = 0.1$, confirming that both [C I] lines are optically thin[2].

3.3.2 *Modeling of the FIR and millimeter emission*

To further constrain the FIR and millimeter properties of GN20, we complement the literature observations with our new continuum flux measurements at 1.86 and 3.05 mm. Existing photometry and millimeter measurements have already been presented in detail (see Magdis et al. 2012b; Tan et al. 2014) including photometry observations from *Herschel* (PACS: 100, 160 µm; SPIRE: 250, 350, 500 µm) and the AzTEC 1.1 mm map (Perera et al. 2008). We also include continuum measurements at 2.2, 3.3, and 6.6 mm (Carilli et al. 2011), and 870 µm observations (Hodge et al. 2015).

We adopted three different methods to infer the FIR properties of GN20. First, we used the silicate-graphite-PAH models from Draine & Li (2007, hereafter DL07), including diffuse ISM and photodissociation region (PDR) components to estimate the $L_{\rm IR}$ (at 8–1000 µm), the $M_{\rm d}$, and the $\langle {\rm U} \rangle$ by fitting the available mid-IR to millimeter photometry (Figure 3.2, *left*). Since the DL07 dust models inherently assume that the dust emission is optically thin and do not determine a luminosity-weighted $T_{\rm d}$ that is commonly used in the literature, we also considered optically thin and general opacity single-temperature modified blackbody (MBB) prescriptions (Berta et al. 2016).

For the general opacity MBB model, we fit the observed FIR and millimeter photometry at $\lambda_{\rm rest} > 50$ µm of GN20 (to avoid contamination from warm dust):

$$S_\nu \propto (1 - e^{-\tau_\nu}) \times B(\nu, T), \tag{3.2}$$

where $B(\nu, T)$ is the Planck function, $\tau_\nu = (\frac{\nu}{\nu_0})^\beta$ is the frequency-dependent optical depth of the dust, ν_0 is the frequency at which the optical depth reaches unity, and β is the dust emissivity. To estimate $M_{\rm d}$, we assume a dust opacity at 850 µm of $\kappa_{850} = 0.43\,{\rm cm^2\,g^{-1}}$ (Li & Draine 2001). In the optically

[2] Adopting a larger size similar to that measured of the CO(2 – 1) emission ($R_{\rm e} \sim 4$ kpc: Carilli et al. 2010; Hodge et al. 2015) yields a $T_{\rm b}$ and $\tau_{\rm [CI]}$ that is ∼ 9.5% of values derived for the $R_{\rm e} = 1.2$ kpc case.

Table 3.1: Derived properties of GN20.

NOEMA observations	
$I_{[CI](^3P_1-^3P_0)}$ [Jy km s^{-1}]	0.70 ± 0.11[a]
$L'_{[CI](^3P_1-^3P_0)}$ [10^{10} K km s^{-1} pc^{-2}]	2.48 ± 0.38
$I_{[CI](^3P_2-^3P_1)}$ [Jy km s^{-1}]	1.80 ± 0.21
$L'_{[CI](^3P_2-^3P_1)}$ [10^{10} K km s^{-1} pc^{-2}]	2.33 ± 0.27
$S_{3.05mm}$ [mJy]	0.36 ± 0.04
$S_{1.86mm}$ [mJy]	2.80 ± 0.13
MBB best-fit solutions	
$T_{d,thick}$ [K]	52 ± 5
β_{thick}	2.00 ± 0.15
$\log(M_{d,thick}/M_\odot)$	9.31 ± 0.16
$\log(L_{IR,thick}/L_\odot)$	13.20 ± 0.03
λ_0 [μm]	170 ± 23
$T_{d,thin}$ [K]	33 ± 2
β_{thin}	1.95 ± 0.11
$\log(M_{d,thin}/M_\odot)$	9.59 ± 0.10
$\log(L_{IR,thin}/L_\odot)$	13.15 ± 0.04

[a] The [C I]($^3P_1 - {}^3P_0$) line width was fixed to the best-fit of the [C I]($^3P_2 - {}^3P_1$) line emission, FWHM$_{[CI](2-1)}$ = 949 km s^{-1}.

thin case ($\nu_0 \ll \nu$), the MBB prescription is reduced to:

$$S_\nu \propto \nu^\beta \times B(\nu, T). \tag{3.3}$$

The SED of GN20 and the best-fit prescriptions are presented in Figure 3.2 and the results are listed in Table 3.1. For the optically thin case, the SED fitting yields $T_d = 33 \pm 2$ K and $\beta = 1.9 \pm 0.1$, which is consistent with the result reported in Magdis et al. (2011) but considerably smaller than the T_{ex} derived from the [C I] luminosity ratio (Section 3.3.1). Accounting for the effect of the cosmic microwave background (CMB) on the (sub-)millimeter dust continuum emission, as detailed in da Cunha et al. (2013), results in consistent best-fit parameters within the uncertainties (Figure 3.2, left). On the other hand, when fitting the FIR SED using a general opacity dust model (equation 3.2), the optical depth reaches unity at a wavelength of $\lambda_0 = c/\nu_0 = 170 \pm 23$ μm with a dust temperature of $T_d = 52 \pm 5$ K, which is fully consistent with T_{ex}, while recovering the same β value as for the optically thin case.

3.4 RESULTS AND DISCUSSION

Recent works have reported a correlation between the T_{ex} derived from [C I] line ratio and the apparent luminosity-weighted T_d derived assuming optically thin MBB prescription with $\beta = 2$ from resolved observations of nearby star-forming galaxies and (U)LIRGs (Jiao et al. 2019b; Jiao et al. 2019a). For galaxies at high-redshift, when T_d is derived using the same MBB prescription, the existence of a $T_{ex} - T_d$ correlation is less clear. Although this is possibly due to the small sample size and lower S/N temperature estimates, which both cause significant scatter, the high-redshift galaxies give, on average, $T_d \geq T_{ex}$, which is consistent with the local systems (Jiao et al. 2019b; Jiao et al. 2019a; Valentino et al. 2020a).

Following the same prescriptions to derive T_{ex} and T_d as proposed in these studies leads to the observation of several curious properties for GN20. The large [C I] line ratio yields $T_{ex} = 48.2^{+15.1}_{-9.2}$ K, which is significantly warmer than the apparent dust temperature of $T_d = 33 \pm 2$ K, opposing to the general trend in the empirical $T_{ex} - T_d$ relation when assuming optically thin FIR dust emission. In fact, the [C I] MC test predicts a 97.5% probability of obtaining a T_{ex} above 33 K. In Figure 3.3, we show the cosmic evolution of the luminosity-weighted dust temperature when including MS, SBs, and dusty SFGs at $z = 0 - 6$ (Béthermin et al. 2015; Schreiber et al. 2018; Jin et al. 2019). The included T_d values from the literature are all consistent with those derived using an optically thin MBB prescription. We convert the mass- to luminosity-weighted T_d measurements using Eq. 6 in Schreiber et al. (2018). The apparent luminosity-weighted dust temperature of GN20 is similar to the average of main-sequence galaxies at $z \sim 1.4$ (Schreiber et al. 2018), despite GN20 being a strong starburst galaxy (SFR $= 1860 \pm 90\,M_\odot\,yr^{-1}$) and exhibiting a factor of $\sim 6\times$ larger specific star formation rate (sSFR $= 16.9\,Gyr^{-1}$) than $z = 4$ MS galaxies (Tan et al. 2014; Sargent et al. 2014; Jin et al. 2019).

Likewise, the optically thin DL07 models (assuming multi-component dust distribution) provide similar results, yielding $\langle U \rangle = 27.2^{+2.6}_{-2.2}$ for GN20 (Magdis et al. 2011; Magdis et al. 2012b; Tan et al. 2014), placing it at a factor of ~ 2.5 times below the $\langle U \rangle - z$ relation for MS galaxies (Béthermin et al. 2015; Magdis et al. 2017). As a sanity check, we also converted $\langle U \rangle$ to T_d following $\langle U \rangle = (T_d/18.9\ \mathrm{K})^{6.04}$ (Magdis et al. 2017; Schreiber et al. 2018; Jin et al. 2019) and used the aforementioned conversion to obtain the luminosity-weighted dust temperature (Schreiber et al. 2018). The inferred

$T_{\rm d,DL07} = 33 \pm 1$ K for GN20 is fully consistent with the dust temperature derived from the optically thin MBB prescription. Lastly, the dust masses derived from the optically thin MBB and the DL07 prescriptions both lead to unphysically large $M_{\rm d}/M_* = 0.04 \pm 0.02$ and $M_{\rm d}/M_* = 0.05 \pm 0.02$, respectively, which is a factor of $\sim 5\times$ higher than the predicted ratios for SBs based on semi-analytical models (Lagos et al. 2012; Béthermin et al. 2015). Although the spatial offset between the optical/UV and the CO+FIR emission could indicate that the stellar mass is underestimated due to dust extinction, the reported dynamical mass analysis of GN20 (Hodge et al. 2012) suggests that only a modest (if any) increase of the stellar mass can be allowed while still being consistent with the dynamical constraints.

Accounting for the effects of the optical depth in the SED modeling (Section 3.3.2) alleviates or even removes all these tensions at once. A free opacity MBB prescription for GN20 indicates that the FIR dust emission is optically thick up to $\lambda_0 = 170 \pm 23$ µm with an actual luminosity-weighted $T_{\rm d} = 52 \pm 5$ K that is similar to the $T_{\rm ex}$ from [C I] (Figure 3.3), which is consistent with the expected dust temperature of a starburst galaxy at $z = 4.05$ with an offset from the MS similar to GN20 (Eq. 18 in Schreiber et al. 2018). The optically thick FIR dust temperature is also in agreement with the observed $T_{\rm ex} - T_{\rm d}$ relation (Jiao et al. 2019a) of $T_{\rm ex} < T_{\rm d}$ (Valentino et al. 2020a). For a comparison with other high-z starbursts, Spilker et al. (2016) report a $\lambda_0 - T_{\rm d}$ correlation based on lensed starburst galaxies at $z = 1.9 - 5.7$ with $\langle \lambda_0 \rangle = 140 \pm 40$ µm, derived using free opacity MBB prescription, yielding consistent results with our derived FIR properties of GN20. Moreover, for a subsample of these galaxies, Bothwell et al. (2017) report larger $T_{\rm d}$ than that of the kinetic temperature ($T_{\rm kin}$) of the molecular gas based on [C I] and CO molecular lines. Under the assumption of LTE, $T_{\rm kin} = T_{\rm ex}$, which results in $T_{\rm d} > T_{\rm ex}$, which is in agreement with previous findings.

As a simple check, we calculated the optical depth of the FIR dust emission similar to the approach described in Jin et al. (2019), using: $\tau = \kappa \times \Sigma_{\rm dust}$ where κ is the dust mass absorption coefficient from Li & Draine (2001) and $\Sigma_{\rm dust}$ is the dust mass surface density. We derive $\Sigma_{\rm dust} \sim 500\,{\rm M}_\odot\,{\rm pc}^{-2}$ assuming $R_{\rm e} \sim 1.2$ kpc (Section 3.3.1) where $\tau \sim 1$ at ~ 170 µm, suggesting that the dust emission is optically thick up to FIR wavelengths [3]. If, indeed, the dust

[3] Large dust optical depths at FIR and submillimeter wavelengths can suppress the [C I] lines yielding fainter line emission as reported for CO line transitions of local ULIRGs (Papadopoulos, Isaak & van der Werf 2010; Papadopoulos et al. 2012). To account for this

emission in SBs is affected by opacity effects with $\lambda_0 > 100\,\mu$m, as it appears for local and high-redshift SB galaxies (e.g., Blain, Barnard & Chapman 2003; Conley et al. 2011; Cox et al. 2011; Riechers et al. 2013; Simpson et al. 2017), the inferred T_d would systematically increase. This would place the SB systems above the T_d–z relation of MS galaxies at all redshifts, solving the puzzling observation of strong SBs being colder (or having lower $\langle U \rangle$) than MS galaxies beyond $z > 2.5$ (Béthermin et al. 2015), as inferred by the optical thin dust models.

An optically thick FIR dust emission will also naturally lead to lower dust masses. For GN20, the free opacity SED modeling results in a M_d/M_* ratio of 0.02 ± 0.01, approaching the predicted ratios of $M_d/M_* < 0.01$ for SBs at $z \sim 4$ (Lagos et al. 2012). The effect of the T_d in the determination of the M_d (and thus of the M_{gas} for a fixed δ_{GDR}) as a function of the rest-frame wavelength used to anchor the M_d estimate is shown in Figure 3.4. In the RJ tail ($\lambda_{rest} \geq 500\,\mu$m), a factor of 2× difference in T_d results in a factor of $\sim 2\times$ difference in M_d, reflecting the well-known dependence of $M_d \propto T_d^{-1}$ in the optically thin limit. However, at shorter rest-frame wavelengths, the discrepancy between the M_d estimates becomes considerably larger, reaching a factor of $\sim 5\times$ at $\lambda_{rest} \sim 200\,\mu$m.

This is a matter of caution with regard to the common approach for inferring the ISM mass (proportional to the M_d and hence the M_{gas}) of high-z galaxies from single-band ALMA continuum observations at observed wavelengths $850 - 1200\,\mu$m (e.g., Scoville et al. 2017a; Liu et al. 2019), under the assumption of a fixed δ_{GDR} and mass-weighted T_d of ~ 25 K. At $z > 3$, such observations probe $\lambda_{rest} < 300\ \mu$m, where moderate deviations from $T_d = 25$ K result in significant changes in M_d (and thus in M_{gas}). Moreover, they trace a regime where the FIR dust emission could be optically thick. In particular, for high-z SBs similar to GN20, an observed $850\,\mu$m measurement probes $\lambda_{rest} \sim 160\,\mu$m, where the dust is likely affected by opacity effects. For reference, a $T_d = 25$ K versus 50 K overestimates M_d (and thus M_{gas}) by a factor of $\sim 7\times$. We stress that the $T_d = 50$ K measured here is luminosity-weighted and

effect, we calculate the intrinsic [C I] line luminosity ratio assuming an isothermal mixture of line-emitting gas and dust. We compute the dust optical depth at the observed frequencies of the [C I] line transitions based on the best-fit model with the opacity free to vary (Section 3.3.2) yielding $\tau_{d,[CI](1-0)} = 0.1$ and $\tau_{d,[CI](2-1)} = 0.2$. Adopting Eq. 4 in Papadopoulos, Isaak & van der Werf (2010), the [C I] luminosity line ratio and excitation temperature would increase to $R = 1.0 \pm 0.2$ and $T_{ex} = 54.1 \pm 13.4$ K, respectively. This does not affect the substance of our results.

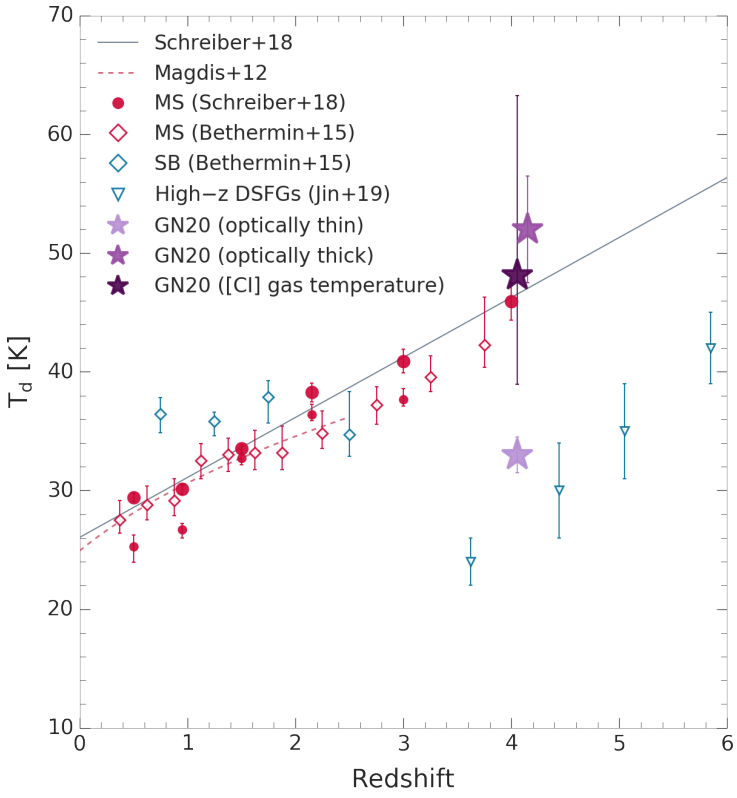

Figure 3.3: Evolution of $T_{\rm d}$ as a function of redshift. We include stacked MS galaxies from Schreiber et al. (2018) (the small red circles present the stacked galaxies in the largest mass bin with $11.0 < \log(M_\star/M_\odot) < 11.5$ whereas large red filled circles are the weighted mean of all galaxies), stacked MS and SB galaxies from Béthermin et al. (2015) (open red and blue symbols, respectively). For the latter, we convert $\langle \mathrm{U} \rangle$ to $T_{\rm d}$ following Schreiber et al. (2018). We also include four dusty SFGs from Jin et al. (2019) (open blue triangles). Purple symbols depict the derived $T_{\rm ex}$ of GN20 from the [C I] luminosity ratio and from the MBB modeling assuming optically thin or thick FIR dust emission.

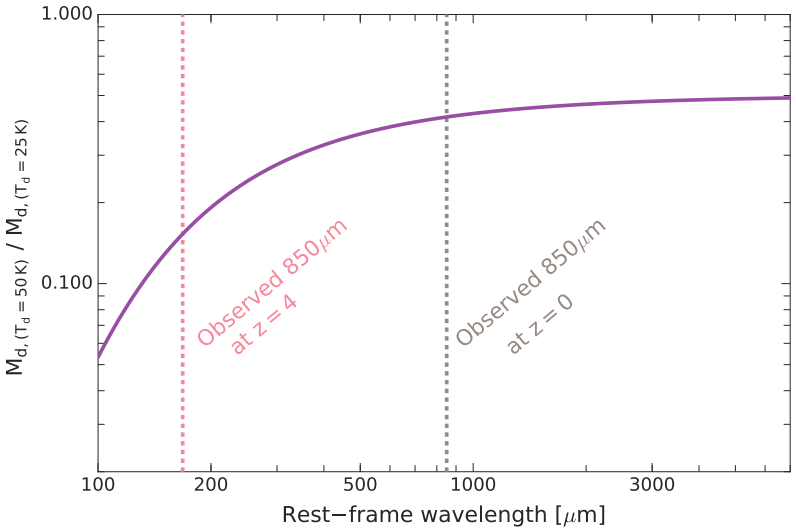

Figure 3.4: Comparison of the derived M_d ratio based on the MBB prescription assuming different dust temperatures (50 K compared to 25 K) as a function of rest-frame wavelength. The dust continuum emission at an observed 850 µm is commonly used to infer M_d.

is, thus, likely to be higher than the mass-weighted T_d.

Using the $T_{ex} - T_d$ correlation to identify possible critical effects of the optical depth on the dust emission in extreme starbursts is potentially useful for settling a few issues concerning GN20. However, this relies on several assumptions and caveats that should be borne in mind; and alternative scenarios explaining $T_{ex} > T_d$ in the optically thin case might be considered. If the [C I] line emission is subthermally excited, the excitation temperatures of the two [C I] line transitions might not be equal as assumed under LTE. In this case, using Eq. 3.1 would lead to a systematically overestimatedT_{ex} (Glover et al. 2015 but see Israel, Rosenberg & van der Werf 2015 about the phases traced by [C I] in extreme conditions of local starbursts).

Cosmic rays and turbulence could, in principle, lead to different gas and dust temperatures (Papadopoulos, Thi & Viti 2004; Bisbas et al. 2017), assuming that the cosmic ray energy density scales with the SFR density (Glover et al. 2015). Therefore, an enhancement of cosmic rays is expected in starbursty environments, increasing the average temperature of the molecular gas, while at the same time, leaving the dust unaffected. An increased rate of cosmic rays in SBs would also lead to enhanced [C I] emission throughout the cloud via CO destruction. However, in this case, models predict larger [C I] to CO lumi-

nosity ratios in SBs than MS galaxies, which is in disagreement with current observations which report that the [C I]/CO luminosity ratio remains roughly constant as a function of $L_{\rm IR}$ and sSFR, at least on global scales (Valentino et al. 2018). This might be due to the fact that the global SFR is not a good predictor of the gas conditions in clouds (Narayanan & Krumholz 2014). Alternatively, turbulence can distribute [C I] throughout the cloud, smoothing the [C I]/CO luminosity ratio (Papadopoulos, Thi & Viti 2004; Bisbas et al. 2017). As turbulence is expected to be dominant in regions with high cosmic ray ionization rates (i.e., in starburst or merger systems), it is plausible that both mechanisms are responsible for heating the molecular gas.

We stress that a scenario with $T_{\rm ex} > T_{\rm d}$ does not change the fact that the apparent dust temperature and the mean radiation field in a typical starburst galaxy at $z = 4$ is significantly lower than that of MS galaxies at similar redshifts and that it provides an apparent $T_{\rm d}$ that is in disagreement with the empirical $T_{\rm ex} - T_{\rm d}$ relation. As our study is based on a single galaxy, the method of using the [C I] line ratio to distinguish between an optically thick or thin FIR dust solution has to be tested for the general population of high-redshift starbursts. However, accounting for optical depth effects at FIR wavelengths in starbursts similar to GN20 can mitigate several observed tensions by providing larger dust temperatures, in addition to lower dust masses, easing the improbable large dust to stellar mass ratios.

3.5 ACKNOWLEDGEMENTS

We thank the anonymous referee for helpful and constructive comments which improved this paper. We also thank Padelis Papadopoulos for useful suggestions on the effect of dust opacity on emission lines. This work is based on observations carried out under project number W16DZ with the IRAM NOEMA Interferometer. IRAM is supported by INSU/CNRS (France), MPG (Germany) and IGN (Spain). IC acknowledges support from Villum Fonden research grant (13160). FV and GEM acknowledge the Villum Fonden research grant 13160 "Gas to stars, stars to dust: tracing star formation across cosmic time", and the Carlsberg Fonden research grant CF18-0388 "Galaxies: Rise And Death. DL acknowledges support and funding from the European Research Council (ERC) under the European Union's Horizon 2020 research and innovation programme (grant agreement No. 694343). GEM and ST acknowledge support from the ERC Consolidator Grant funding scheme

(project ConTExt, grant number No. 648179). The Cosmic Dawn Center is funded by the Danish National Research Foundation under grant No. 140.

CHAPTER 4

Ongoing and future projects

This thesis has so far focused on the characterization of the ISM properties of local and high-redshift galaxies. Specifically, I have studied the molecular gas content of star-forming galaxies using multiple gas tracers and proposed the emission from PAHs as a new proxy for the total molecular gas mass. Moreover, I have studied the dust and gas components in a high-redshift starburst galaxy and presented a method to break the degeneracy between the dust optical depth and temperature by exploiting the empirical correlation with the gas temperature derived from [C I] observations. In this chapter, I present the ongoing and future projects, including those that are built upon the results shown in Chapters 2 and 3.

4.1 How well do PAHs trace the molecular gas?

As presented in Chapter 2, my analysis suggests that PAHs can probe the molecular gas mass of galaxies within a factor of ×2. With the upcoming launch of *JWST*, PAHs will routinely be detected in galaxies up to $z \sim 3.5$. In 1 – 2 hours of observations, *JWST*/MIRI can detect PAHs in a normal main-sequence galaxy at $z \sim 2$, fully sampling the bulk of the star-forming

population. As PAHs are ubiquitous in the ISM of galaxies, targeting galaxies at $z = 0 - 3$ can be an alternative and powerful tool to observe the molecular gas content. Although promising, I believe that exploring PAHs and their dependencies of several galaxy properties is crucial to reach a full understanding of the mechanisms regulating this component of the ISM.

Metallicity of 5MUSES galaxies: Previous works report that the emission from PAHs is correlated with the metallicity and is suppressed in low-metallicity galaxies. Moreover, numerous studies find higher IR/MIR luminosity ratios (IR8 $\equiv L_{\rm IR}/L_8$, where L_8 is the luminosity at rest-frame 8 µm), weaker FIR atomic lines, and larger star formation efficiencies with increasing SFR/SFR$_{\rm MS}$ (Daddi et al. 2010a; Elbaz et al. 2011; Nordon et al. 2012; Magdis et al. 2014). These findings have been interpreted as due to more intense and compact star-forming regions in galaxies above the MS. Resolved observations of the Hα emission in star-forming galaxies at $z \sim 1$ have been used to determine the SFR surface density ($\Sigma_{\rm SFR}$), which is strongly correlated to the distance from the MS where galaxies offset from the MS tend to have denser star formation (Magdis et al. 2016). Moreover, these authors report metallicity gradients along the MS: $Z \propto ({\rm SFR/SFR_{MS}})^{-0.32}$, where galaxies above the MS have lower metallicities than those on the MS.

A future project will thus be dedicated to studying the dependence of the PAH abundance of the gas-phase metallicity. This will be done using the K-band Multi-Object Spectrograph (KMOS Sharples et al. 2013) integral field spectroscopy (IFS) of a subsample of 20 galaxies from the 5MUSES sample with PAH and CO detections. The metallicity will be derived from the Hα/[N II] emission line ratio (Kewley & Dopita 2002) and will thus allow one to investigate possible trends with PAHs, CO, SFR/SFR$_{\rm MS}$, and metallicity. The IFS observations will enable us to verify if the same trends are observed in SFGs at $z < 0.3$, in addition to determining if the emission from PAHs varies as a function of the distance from the MS and metallicity.

PAHs and [CI]: As the PAH–$M_{\rm gas}$ correlation includes CO- and dust-inferred gas masses with their respective conversion factors and uncertainties, additional gas proxies are important to properly test the use of PAHs as probes for the molecular gas mass in star-forming galaxies. Therefore, the next step forward is to connect the PAHs with [C I], which has been put forward as a

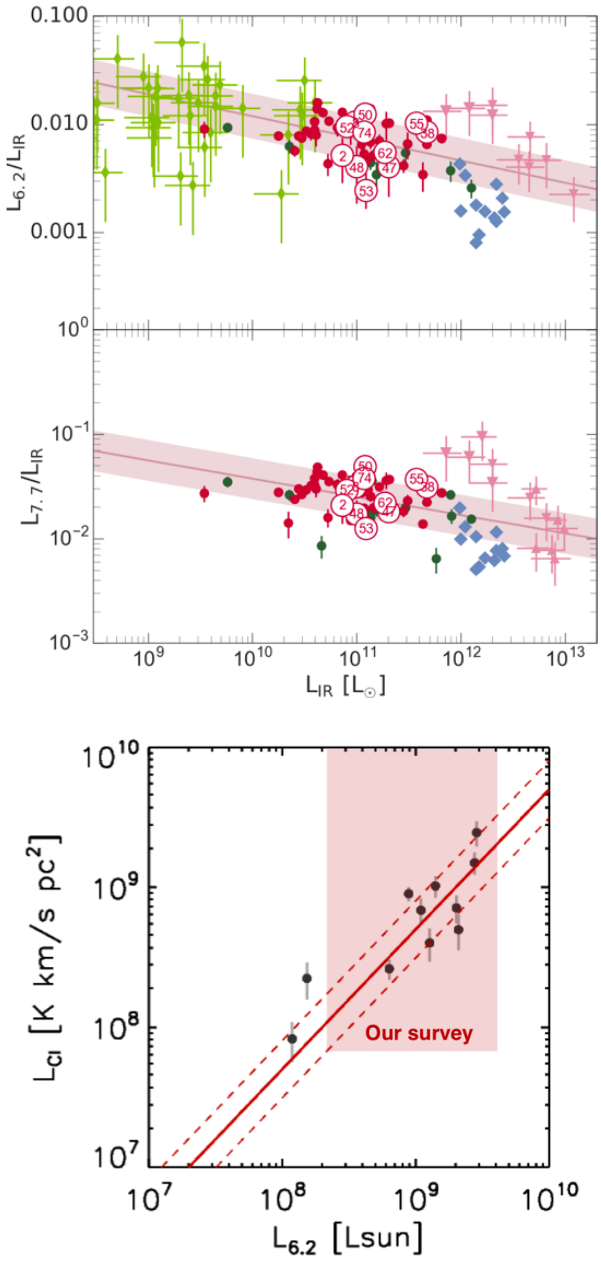

Figure 4.1: *Upper*: Correlation between 6.2 and 7.6 µm PAH/IR vs. IR luminosity. The selected galaxies (numbered symbols) are probing the upper part of the MS and above at $z < 0.3$. The figure also includes local SINGS galaxies (green), 5MUSES galaxies (red) with AGN (red), local ULIRGs (blue), and high-redshift SFGs (pink). *Lower*: An emerging trend between [C I] and $L_{6.2}$ for 11 starburst galaxies from the whole *Herschel*/FTS and *Spitzer*/IRS archives (Liu et al. 2015; Kamenetzky et al. 2016; Valentino et al. 2018). The solid and dashed lines depict a slope of 1 and a scatter of 0.20 dex, respectively. The targeted galaxies are expected to fall within the red region.

promising tracer of the molecular gas content in galaxies (e.g., Papadopoulos, Thi & Viti 2004; Valentino et al. 2018; Valentino et al. 2020a). Although an indication of a correlation between PAHs and [C I] appears to exist (Figure 4.1, *lower*), the current sample is limited to 11 objects that are dominated by bright starburst galaxies. Encouraged by the preliminary results, we have been granted time with the ALMA Atacama Compact Array (ACA) in Cycle 6 and 7 (PI: Cortzen) to observe the [C I]($^3P_1 - {}^3P_0$) line transition in a subsample of 12 PAH-detected MS and SB galaxies (Figure 4.1, *upper*) from the 5MUSES sample (Wu et al. 2010) at $z < 0.3$ with spectroscopic redshifts, and photometric coverage from UV to FIR wavelengths.

The observations will allow us to bridge the existing [C I] observations of SBs at $z \sim 0$ and $z = 2 - 4$ and $z \sim 1$ MS galaxies with a sample of both MS and SB galaxies at intermediate redshifts (Figure 4.2). Moreover, doubling the sample will allow us to reduce the statistical uncertainties and determine the slope and the scatter of the galaxy-integrated PAH–[C I] relation. We will infer molecular gas masses from the continuum measurement through the RJ method (Scoville et al. 2014) and compare them with those obtained from the $M_{\rm d} - \delta_{\rm GDR}$ approach. Lastly, we will derive SFEs and gas fractions of our targets to investigate possible variations at the upper edge of the MS at $\langle z \rangle = 0.2$.

Lastly, as the relation between PAHs, and the molecular gas mass as traced by CO and dust at $z = 0 - 4$ is currently reported on galaxy-integrated scales, synergies between facilities such as *JWST*, NOEMA, and ALMA will be required to obtain resolved observations of the emission from PAHs and molecular gas tracers (i.e., CO, dust, and [C I]), which can verify whether PAHs are spatially correlated with the molecular gas on sub-galactic scales.

4.2 THE ISM CONDITIONS AND THE GAS EXCITATION LADDER OF GN20

As the IRAM NOEMA observations of GN20 also provided a secure detection of the CO(7 – 6) line, in addition to the [C I] line observations, a future project will be dedicated to studying the CO+[C I] spectral line energy distribution (SLED) of the starburst galaxy to constrain the density and the kinetic temperature ($T_{\rm kin}$) of the gas (e.g., Meijerink, Glassgold & Najita 2008; Carilli & Walter 2013; Popping et al. 2019). Although a two-component

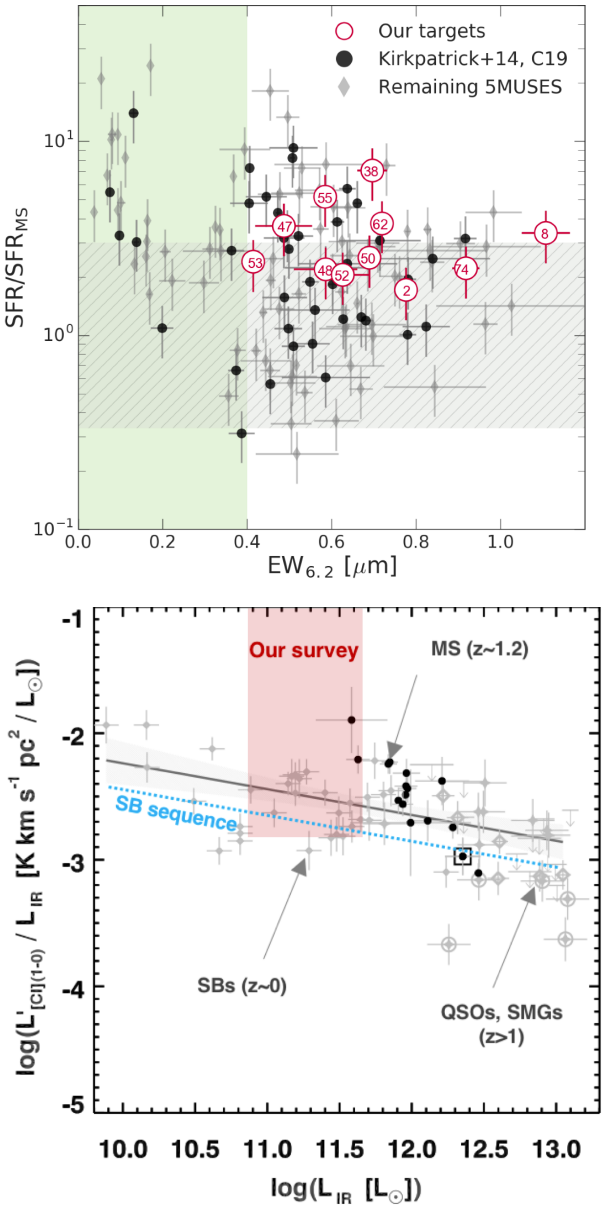

Figure 4.2: **[CI] observations using ACA**. *Upper*: The selected galaxies (numbered points) with respect to the main-sequence (grey region), where AGN-dominated galaxies (EW$_{6.2}$< 0.4 µm, green region) are excluded. Black and grey points are CO-detected and the remaining galaxies from 5MUSES, respectively (Wu et al. 2010; Kirkpatrick et al. 2014; Cortzen et al. 2019). *Lower*: Expected location of the targets of our ALMA Cycle 6 and 7 programs (red) in the $L'_{[CI]}/L_{IR}$ vs. L_{IR} parameter space. Black circles are $z \sim 1$ MS galaxies (Valentino et al. 2018), whereas grey points are SBs ($z \sim 0$, $z > 1$) from the literature (see references in Valentino et al. 2018).

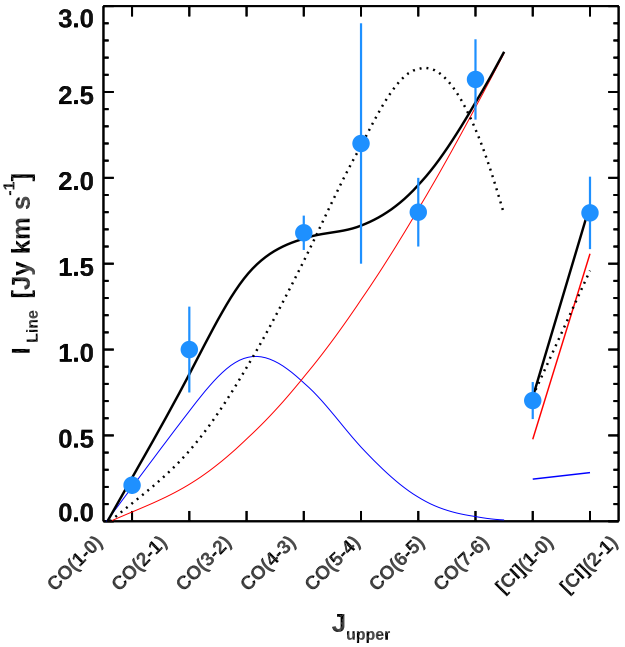

Figure 4.3: **CO+[CI] SLED of GN**20. Distribution of the observed velocity-integrated CO and [C I] line flux densities (blue points) versus the line transitions. The CO(7 – 6) and [C I] line fluxes are from Cortzen et al. (2020), while the remaining are from the literature (CO(1 – 0): Carilli et al. 2010; CO(2 – 1): Carilli et al. 2010; Carilli et al. 2011; Hodge et al. 2012; CO(4 – 3): Daddi et al. 2009; Tan et al. 2014; CO(5 – 4): Carilli et al. 2010; CO(6 – 5): Carilli et al. 2010). The double-component fit (black line) includes a low (blue line) and high excitation components (red line). The single-component fit is shown (black dashed line). Figure is provided by Francesco Valentino.

CO SLED has been presented in Carilli et al. (2010), the analysis included the upper limit on the CO(7 – 6) line reported by Casey et al. (2009). The two [C I] line transitions can in combination with the CO line measurements help to break the temperature-density degeneracy and be used to determine the excitation temperature from the ratio of the [C I] line luminosities (Weiß et al. 2003). The preliminary results of the CO and [C I] excitation ladder for GN20 is presented in Figure 4.3, following the large velocity gradient (LVG) fitting described in Liu et al. (2015) and Daddi et al. (2015). While a single-component model is unable to model the data observations, a fit including a low- and a high-excitation component yields H_2 gas densities

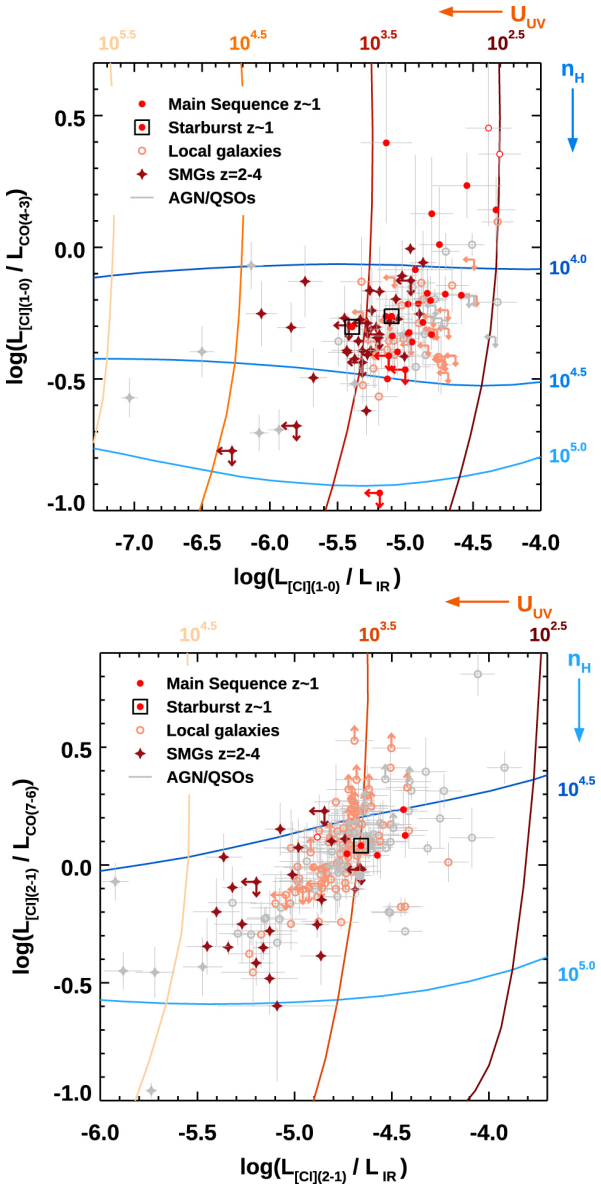

Figure 4.4: [C I]($^3P_1 - {}^3P_0$)/CO(mid-J) and [C I]($^3P_1 - {}^3P_0$)/IR luminosity line ratios (*upper*) and [C I]($^3P_2 - {}^3P_1$)/CO(7 – 6) and [C I]($^3P_2 - {}^3P_1$)/IR luminosity ratios (*lower*) in units of $L_\odot$ for the compilation of [C I]-detected galaxies reported in Valentino et al. (2020a). Both panels include main-sequence galaxies at $z \sim 1$ and one at $z = 2.2$ (red solid circles), starbursts at $z \sim 1.2$ (open black squares), local star-forming galaxies (open orange circles), local galaxies with AGN signatures (open gray circles), $z \sim 2 - 4$ SMGs (dark red stars), and QSO/AGN-dominated galaxies (gray symbols). The red and blue solid contours represent the UV radiation field (U_{UV}) and density (n_H) based on PDR modeling, respectively. Figures are from Valentino et al. (2020a).

of $\log(n_{H,low}/cm^{-3}) = 3.2 \pm 0.5$ and $\log(n_{H,high}/cm^{-3}) = 5.0 \pm 0.5$, respectively. On the other hand, the kinetic temperatures of $T_{kin,low} = 30 \pm 138$ K and $T_{kin,high} = 95 \pm 115$ K are unconstrained. Higher-J transitions of the CO transitions ($J_{upper} > 7$) of GN20 will be needed to constrain the second peak of its CO SLED, as shown for local ULIRGs and distant SMGs (Papadopoulos et al. 2012; Yang et al. 2017; Cañameras et al. 2018). In this regard, GN20 appears similar to other high-redshift star-bursting galaxies, hosting significant reservoirs of dense and highly-excited gas. Moreover, a similar CO+[C I] SLED analysis will be carried out for the two SMGs in the same field, GN20.2a, and GN20.2b, as they are both within the primary beam of the GN20 observations.

4.3 [CI] AND CO EMISSION IN A MASSIVE MS GALAXY $z = 3$

While recent works report [C I] emission in ~ 30 MS galaxies at low- and intermediate-z (Valentino et al. 2020a), at higher redshift only one MS galaxies has been detected at $z = 2$ (Popping et al. 2017) where the majority of the observations comprise of bright starbursts, quasars, and SMGs (Figure 4.4). Furthermore, out of the total MS galaxies, only 5 sources include observations of the two [C I] line transitions, which are required to constrain the excitation temperature, and the [C I] and H_2 masses.

In this direction, we observed [C I]($^3P_1 - {}^3P_0$), [C I]($^3P_2 - {}^3P_1$), and CO(7–6) with IRAM NOEMA (PI: Cortzen) in a well studied IR-luminous ($\log(L_{IR}/L_\odot) = 12.78 \pm 0.03$), massive ($\log(M_\star/M_\odot) = 11.28 \pm 0.12$) MS galaxy D49 from the optically selected sample of Lyman Break Galaxies (LBGs) in the Extended Groth Strip field (EGS) at $z = 3$ (Steidel et al. 2003; Shapley et al. 2003; Magdis et al. 2017). Existing observations of this galaxy include CO(3 – 2) obtained with the IRAM Plateau de Bure Interferometer (PdBI), Ly-α emission from rest-frame UV spectroscopy with the Keck telescope, and images from the Advanced Camera for Surveys (ACS) aboard the Hubble Space Telescope (*HST*). Moreover, photometric measurements of this galaxy have been obtained from optical to millimeter wavelengths using *Spitzer*, *Herschel*, and IRAM among others. Its well sampled SED allows us to determine the FIR properties, including the dust mass ($\log(M_d/M_\odot) = 9.12 \pm 0.12$) and dust temperature ($T_d = 41 \pm 2$ K).

The [C I] and CO(7 – 6) line observations will extend the redshift and IR luminosity range presented in Valentino et al. (2018) and Valentino et al. (2020a) to a regime that is currently dominated by starburst galaxies.

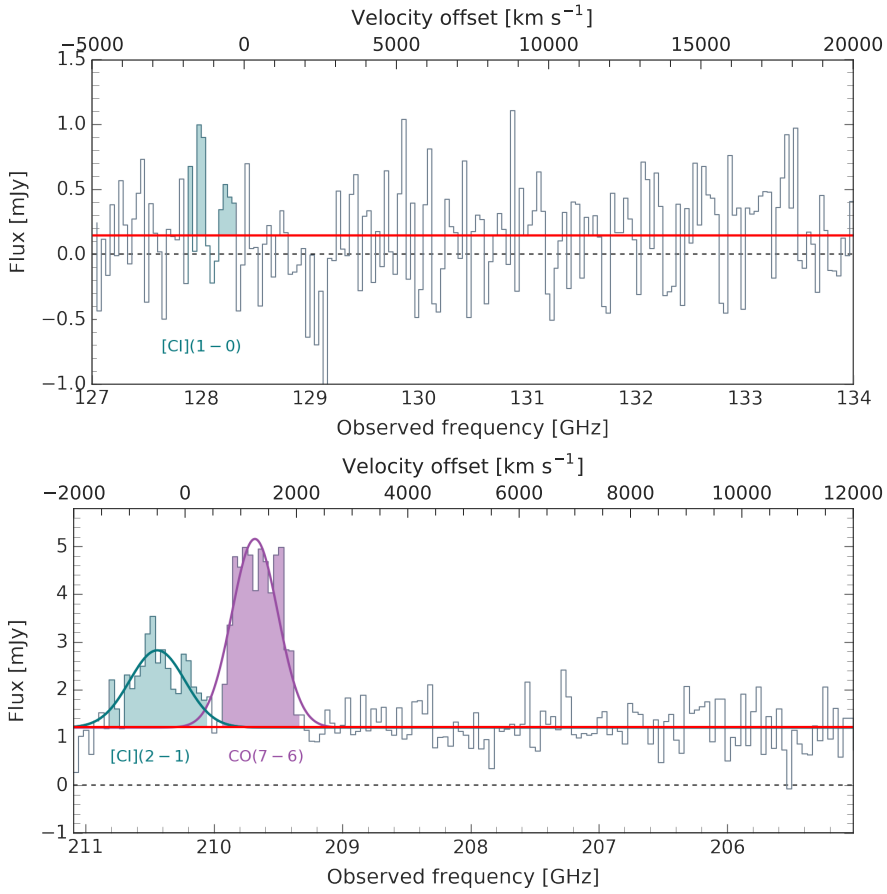

Figure 4.5: **D49**: The spectra of the [C I]($^3P_1$ – $^3P_0$) line (*upper*) and the [C I]($^3P_2$ – $^3P_1$) and CO(7 – 6) lines (*lower*). The colored areas show the detected line emission as labeled, the red lines show the continuum level, and the dashed lines indicate the zero flux-level. The velocity offset in both panels is relative to the expected frequency at $z = 2.85$.

Furthermore, the emission from the [C I] and CO lines can be used to constrain ISM properties of the galaxy including the gas density (n_H) and the UV radiation field (U_{UV}) from PDR modeling as shown in Figure 4.4 (e.g., Popping et al. 2017; Valentino et al. 2020a). As such, we will determine if D49 has similar ISM properties to MS galaxies at lower redshifts based on the inferred n_H and U_{UV} and the observed luminosity ratios. The observations will also provide a direct comparison of the [C I], CO, and dust properties with that of GN20. Figure 4.5 shows the [C I] and CO(7 – 6) spectra of D49, binned in steps of 90 km s^{-1}. As for GN20, following the procedure in Daddi et al. (2015), we searched for lines by scanning the S/N spectra at the reported coordinates of D49 based on the CO(3 – 2) observations (Magdis et al. 2017). Although the [C I]($^3P_1$ – $^3P_0$) line is faint and remains undetected, the [C I]($^3P_2$ – $^3P_1$) and CO(7 – 6) lines are robust and detected at levels of 6σ and 26σ, respectively. For the [C I]($^3P_2$ – $^3P_1$) line, we derive a velocity-integrated flux of 0.60 ± 0.10 Jy km s^{-1} and a line width of 971 km s^{-1}. The best-fitted line width of the CO(7 – 6) of 629 km s^{-1} is narrower than that of the [C I]($^3P_2$ – $^3P_1$) line profile, similarly to the observations of GN20 (Figure 3.1 in Chapter 3). The velocity-integrated flux of the CO(7 – 6) line is 2.0 ± 0.08 Jy km s^{-1}. The continuum at 1.86 mm and 3.05 mm are detected at 4σ and 2σ significance, respectively. We adopt the best-fitted line width of the [C I]($^3P_2$ – $^3P_1$) line to determine the velocity-integrated flux of the [C I]($^3P_1$ – $^3P_0$) line emission yielding 0.36 ± 0.12 Jy km s^{-1}. The upper limit on [C I]($^3P_1$ – $^3P_0$) can thus be used to constrain a lower and upper limit on the excitation temperature and the neutral atomic carbon mass (eq. 1.5 in Chapter 1). The pilot study shows the feasibility of [C I] and high-J CO detections in massive MS galaxies at the peak of the cosmic star formation history. Such effort can be readily extended to the growing sample of spectroscopically confirmed main-sequence objects at high redshift, greatly expanding the current analysis based on mid-J CO transitions and dust emission.

4.4 MASSIVE QUIESCENT GALAXIES AT COSMIC NOON

In the local Universe, it has been established that galaxies are separated into two broad populations of quiescent and star-forming galaxies. For the former, the most massive ones ($\log(M_\star/M_\odot > 11.0$) are referred to as local ultra-massive galaxies (UMGs) and tend to reside in high-density environments such as groups or clusters of galaxies (e.g., Blanton & Moustakas 2009).

Quiescent galaxies follow tight scaling relations based on their physical properties which distinguish them from the general star-forming population of galaxies. They populate the extreme massive end of the red sequence in the galaxy color-magnitude diagram (Baum 1959; de Vaucouleurs 1961; Strateva et al. 2001; Bell et al. 2004) and form the fundamental plane (Djorgovski & Davis 1987; Dressler et al. 1987), which is a three-dimensional plane describing the relation between the effective radius, the average surface brightness within the effective radius, and the central velocity dispersion. Moreover, they are characterized by early-type morphologies, old mean stellar ages, and little dust attenuation. Most of the stars in local UMGs must have formed in the first ~ 3 Gyr if cosmic history (i.e., $z > 2$) through short (< 1 Gyr, as low as ~ 0.2 Gyr for the most massive galaxies), hence intense, bursts of star formation (Thomas et al. 2005; Renzini 2006; van Dokkum & van der Marel 2007).

At higher redshift, the increasing observations of massive ($M_\star \geq 10^{11}\, M_\odot$) quiescent galaxies (QGs) with weak or absent star formation challenge the current understanding of galaxy formation and evolution (e.g., Schreiber et al. 2018). In particular, at the peak of the cosmic star formation activity at $z \sim 2$ (Madau & Dickinson 2014), half of the most massive galaxies at this epoch are already passive and devoid of star formation (Brammer et al. 2011). Furthermore, the existence of massive dead galaxy populations at $z > 3$ implies that they must have formed through short and intense bursts of star formation early in the Universe (Glazebrook et al. 2017; Valentino et al. 2020b). How and why did they die? The physical mechanisms responsible for quenching star formation in galaxies are some of the most debated topics in galaxy studies. Several possibilities have been suggested including feedback from an active galactic nucleus (AGN) or star formation activity, gas strangulation or starvation, virial shocking of the circumgalactic medium, or from a combination of these (Man & Belli 2018, and references therein), although no consensus has yet been reached.

Radio emission in quiescent galaxies: At low redshifts ($z < 0.3$), strong radio emission have been observed in massive elliptical galaxies (Kauffmann et al. 2003; Best et al. 2005; Simpson et al. 2013), which can not be explained by the low observed SFRs through the radio-SFR relation (Bell 2003). A common interpretation is that the excess radio emission originates from an AGN at

the center of the galaxy, where radiation or jets from the accreting black hole prevents the gas to cool condense and form stars or removes it entirely from the galaxy (e.g., Fabian 2012). These radio-loud AGNs are generally hosted by elliptical galaxies and are classified by their large observed radio jets and lobes (Wilson & Colbert 1995).

Previous works have reported that the fraction of radio-loud galaxies ($f_{\rm RL}$) is a strong function of the host galaxy stellar mass ($f_{RL} \propto M_{\star}^{2.5}$: Best et al. 2005), reaching up to > 30% at stellar masses above $5 \times 10^{11}\,M_{\odot}$ and radio luminosities $> 10^{23}\,{\rm W\,Hz^{-1}}$. At higher redshift ($z = 1 - 2$), the radio fraction remains constant for massive galaxies with $M_{\star} > 10^{11.5}\,M_{\odot}$. The high ratio of detected radio excess in QGs suggest that AGNs play an important role in the evolution of these galaxies. Although Barišić et al. (2017) reported coinciding radio and UV emission in a sample of quiescent candidates at $z \sim 1$, to our knowledge, no results are reported in the literature for QGs at higher redshift and closer to their quenching epoch. In this chapter, I report the current analysis of a sample of 14 Ultra Massive Quiescent Galaxies (UMQGs) at $z = 2$ with both rest-frame UV and optical *HST* imaging, in addition to X-shooter spectroscopy presented in Stockmann et al. (2020). The sample is mainly selected from the Cosmic Evolution Survey (COSMOS: Scoville et al. 2007), plus an object from the Ultra Deep Survey (UDS) field (Toft et al. 2012). The UMQG sample was initially selected with $z_{\rm phot} > 1.9$ ($z_{\rm phot} > 1.6$ for one source), $\log(M_{\star}/M_{\odot} > 11)$, and $K_{\rm AB} < 20.5\,{\rm mag}$ (Figure 4.6), for follow-up observations with the VLT/X-shooter spectrograph and *HST*/WFC3 imaging, complementing the existing multiwavelength photometry observations from UV to NIR wavelengths. The $K_{\rm AB}$-band, stellar mass, photometric redshift ($z_{\rm phot}$), and rest-frame colors are estimated using EAZY (Brammer, van Dokkum & Coppi 2008), and stellar masses are determined using the FAST code (Kriek et al. 2009).

The aim of this project is to explore the FIR and radio properties of this 60% mass-complete sample of 14 spectroscopically confirmed UMQGs close to their quenching epoch at $z \sim 2$. The goal is to characterize possible pockets of remaining dust and gas reservoirs, and investigate the connection between AGN and star formation activity, possibly offering insight into the processes that caused their death. For this reason, I cross-matched the sample with the "super-deblended" FIR to submillimeter catalog from Jin et al. (2018), where the FIR emission is deblended to match the optical-NIR positions based

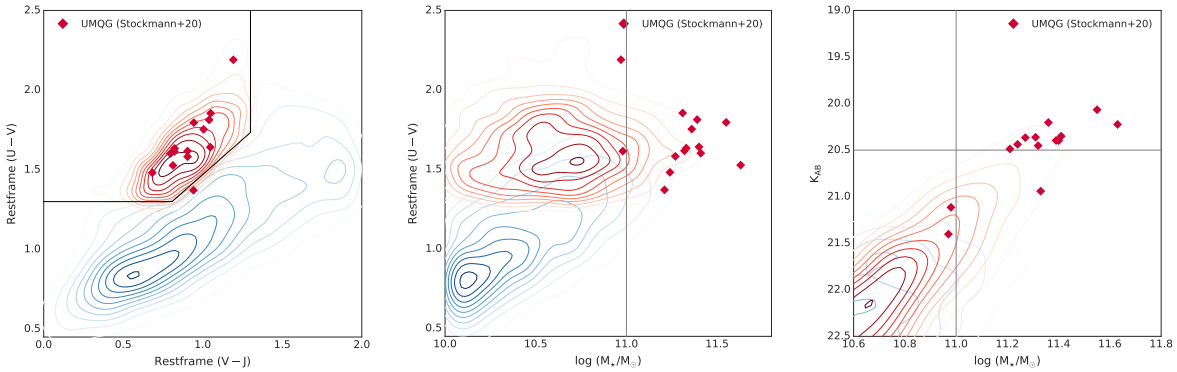

Figure 4.6: *Left: UVJ* colour-colour diagram at $1.9 < z < 2.5$ for galaxies with $\log(M_\star/M_\odot) > 10$. The black solid lines separating the SFGs (blue contours) from the quiescent galaxies (red contours) are from Muzzin et al. (2013). We also overplot the ultra-massive quiescent galaxies from (Stockmann et al. 2020) as red diamonds. *Middle*: Rest-frame *U-V* color vs. as a function of stellar mass. The grey line is drawn at $\log(M_\star/M_\odot) > 11$. *Right:* K_s band flux versus stellar mass. The grey lines drawn at $K_s = 20.5$ and $\log(M_\star/M_\odot) > 11$ present the selection of the UMQG sample in Stockmann et al. (2020) (Fig. 1).

on a mix of priors defined from deep *Spitzer* MIPS 24 µm and VLA 3 GHz detections. Based on the VLA 1.4 GHz and 3 GHz flux measurements from Jin et al. (2018), radio luminosities are derived following the conversion reported in Pracy et al. (2016) and assuming a spectral index of 0.7. Note that the VLA-COSMOS 3 GHz survey (rms $\sim$ 2.3 µJy beam^{-1}) has substantially better sensitivity than the 1.4 GHz observations (rms $\sim 10-15$ µJy beam^{-1}), yielding four times more radio sources at 3 GHz compared to that at 1.4 GHz (Smolčić et al. 2017). Therefore, the analysis relies on the 3 GHz detections. The radio emission is considered a detection if the signal to noise (SNR) > 5.

In Figures 4.7, 4.8, and 4.9, I present the *HST* images of the UMQG sample from Stockmann et al. (2020). For the 6 radio-detected galaxies, where the contours of the 1.4 and 3 GHz emission are shown, it is confirmed that the radio emission in these galaxies is coinciding with their rest-frame optical light. Moreover, all the radio-detected sources are classified as radio-loud with $L_{3\,\mathrm{GHz}} > 10^{23}\,\mathrm{W\,Hz^{-1}}$ (Best et al. 2005). Five of the radio-detected galaxies have *Spitzer*/MIPS 24 µm detections, which could indicate that an AGN is responsible for the heating the MIR emission in these galaxies. As none of the galaxies are detected at FIR or submillimeter wavelengths, the radio emission at unlikely to arise from star formation. Interestingly, only one of the galaxies

that were reported in Stockmann et al. (2020) to be double systems with major mergers (UV-10899, UV-250513, and CP-561356) and minor mergers (UV-105842 and CP-1291751) are detected at 3 GHz, where the radio detection is centered on the most massive system.

The next step forward is to explore if the spectroscopically-confirmed UMQGs are representative of the massive QGs population at these redshifts and compare the radio fraction of the UMQGs with that of the general sample at $1.9 < z < 2.5$ with $\log(M_\star/M_\odot > 10)$ in the COSMOS field, and the fractions reported in previous studies (e.g., Best et al. 2014; Williams & Röttgering 2015; Barišić et al. 2017). For the general sample in the COSMOS field, the relation between SFR and radio luminosity (Best et al. 2005) will be used to determine if the radio detections arise from star formation. Moreover, AGN duty cycles will be inferred which will be compared with those predicted from semi-analytical models, assuming that the luminosity of the AGN can be converted to a kinetic energy injected by the radio jet (e.g., Ceraj et al. 2018, and references therein). As previous works report such scaling relations between the radio and kinetic luminosities (e.g., Willott et al. 1999; Cavagnolo et al. 2010), this comparison can provide insight to our understanding of the the radio mode feedback in quiescent galaxies at the peak of the cosmic star formation activity. Moreover, as quiescent galaxies represent the final stages of galaxy evolution, establishing the mechanisms responsible for quenching their star formation is important to understand the complex life phases of galaxies, from their birth to death.

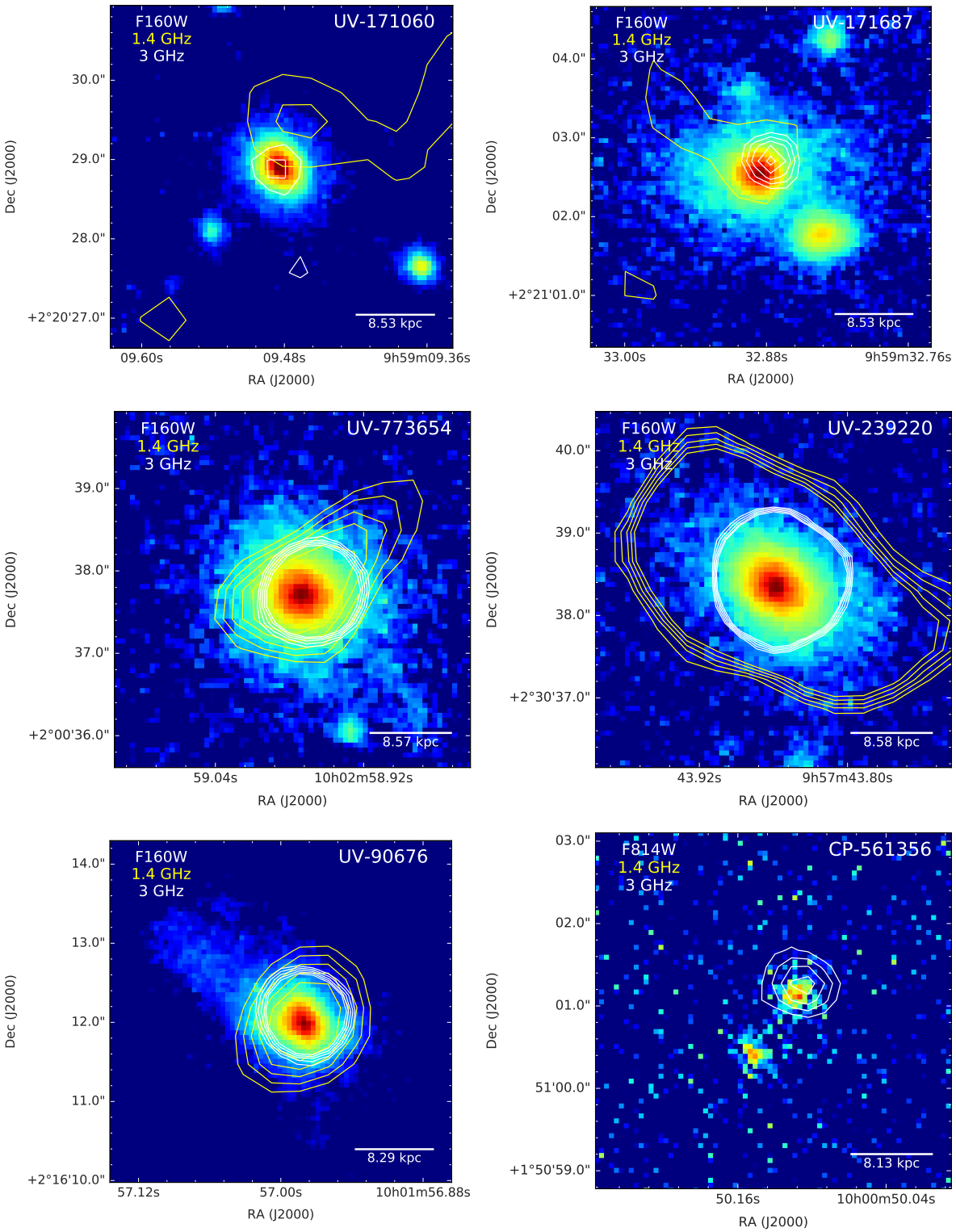

Figure 4.7: *HST* images (F160W or F814W) overlaid with VLA 3 GHz and 1.4 GHz contours (white and grey, respectively) of the radio-detected UMQGs from Stockmann et al. (2020).

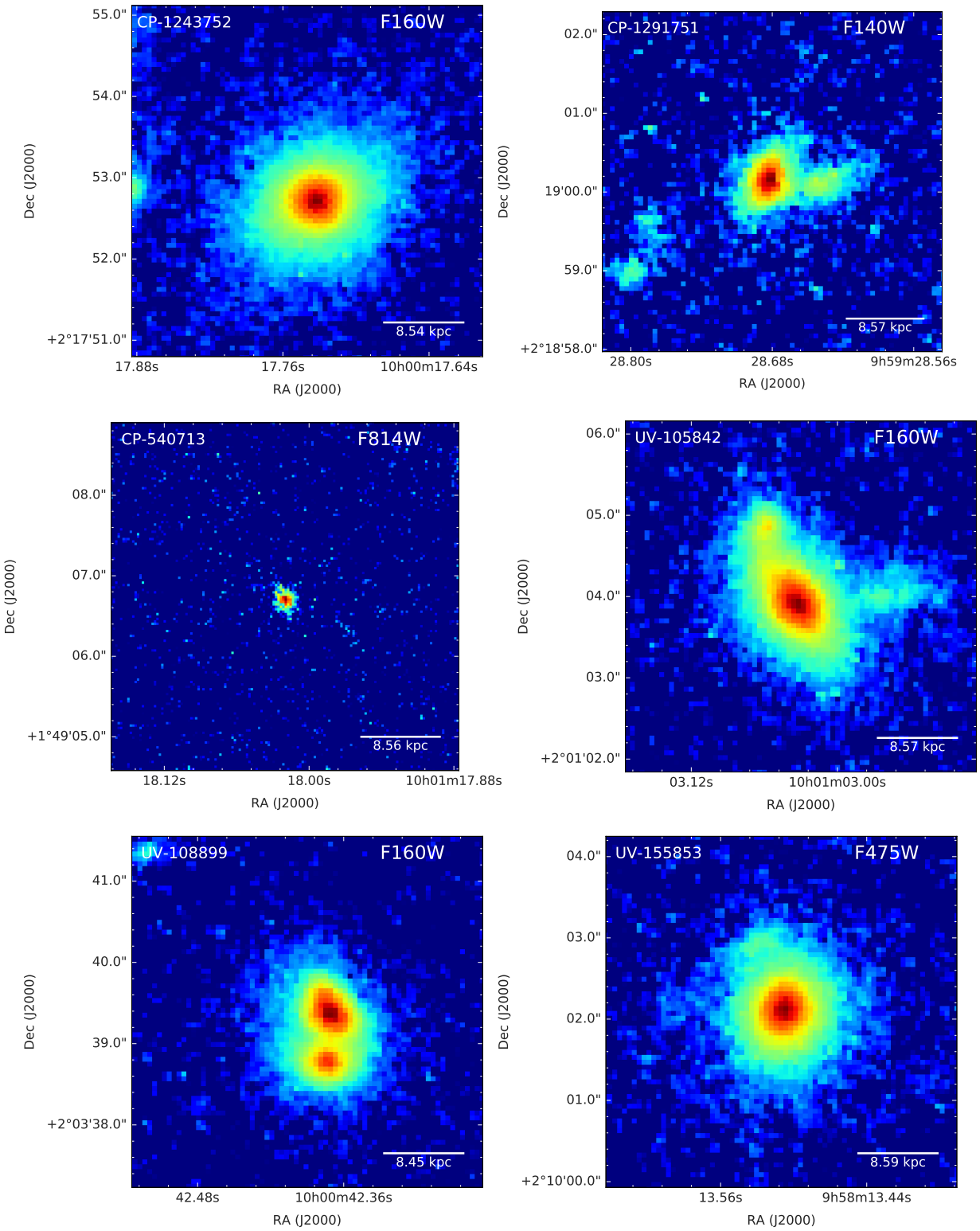

Figure 4.8: *HST* images (F140W, F160W, F475W or F814W) of the UMQGs from Stockmann et al. (2020) with no detections at 1.4 and 3 GHz.

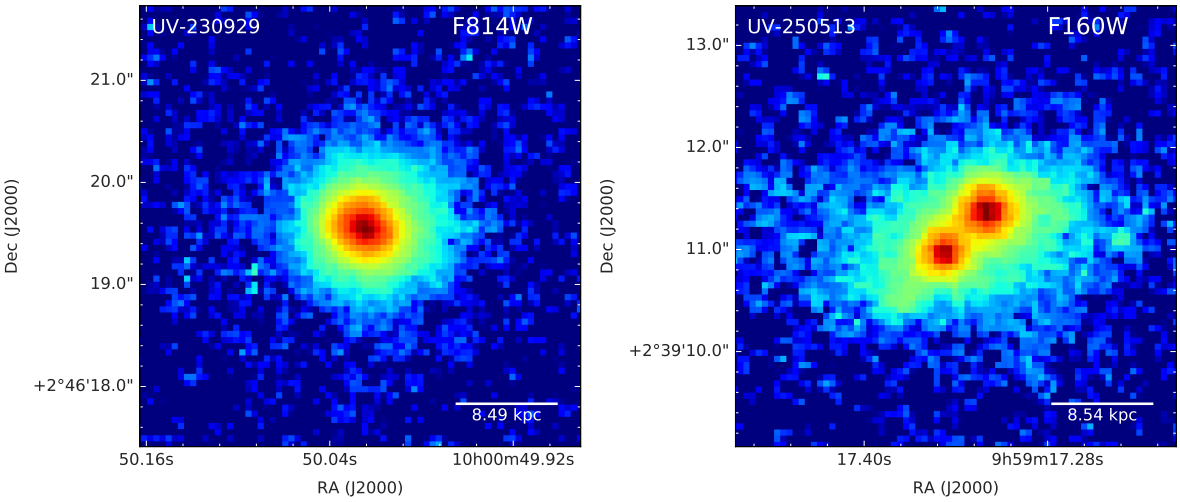

Figure 4.9: *HST* images (F160W or F814W) of the UMQGs from Stockmann et al. (2020) with no detections at 1.4 and 3 GHz.

List of publications

Total: 7 – first author: 2

1. **Cortzen, I.**; Magdis, G. E.; Valentino, F.; Daddi E.; Liu, D.; Rigopoulou, D.; Sargent, M.; Riechers, D.; Cormier, D.; Hodge, J. A.; Walter, F.; Elbaz, D.; Béthermin, M.; Greve, T. R.; Kokorev, V.; & Toft S.,
"*Deceptively cold dust in the massive starburst galaxy GN20 at $z \sim 4$*",
Astronomy & Astrophysics Letters, Volume 634, L14, 2020.
2020A&A...634L..14C

2. Stockmann, M.; Toft, S.; Gallazzi, A.; A.; Zibetti, S.; Conselice, C. J.; Margalef-Bentabol, B.; Zabl, J.; Jørgensen, I.; Magdis, G. E.; Gomez-Guijarro, C.; Valentino, F. M.; Brammer, G. B.; Ceverino, D.; **Cortzen, I.**; Davidzon, I.; Demarco, R.; Faisst, A.; Hirschmann, M.; Krogager, J.-K.; Lagos, C. D.; Man, A. W. S.; Mundy, C. J.; Peng, Y.; Selsing, J.; Steinhardt, C. L.; & Whitaker, K. E.,
"*X-Shooter Spectroscopy and HST Imaging of 15 Ultra Massive Quiescent Galaxies at $z \gtrsim 2$*", The Astrophysical Journal, Volume 888, Issue 1, article id. 4, 23 pages, 2020.
2020ApJ...888.4S

3. Valentino, F.; Magdis, G. E.; Daddi, E.; Liu, D.; Aravena, M.; Bournaud, F.; **Cortzen, I.**; Gao, Y.; Jin, S.; Juneau, S.; Kartaltepe, J. S.; Kokorev, V.; Lee, M.; Madden, S. C.; Narayanan, D.; Popping, G.; & Puglisi, A.,
"*The properties of the interstellar medium of galaxies across cosmic time as traced by the neutral atomic carbon [CI]*",
The Astrophysical Journal, Volume 890, Issue 1, 24 pages, 2020.
2020ApJ...890...24V

4. Hernán-Callabero, A.; Spoon, H.; Alonso-Herrero, A.; Hatziminaoglou, E.; Magdis, G. E.; Pérez-González, P. G.; Pereira-Santaella, M.; Arribas, S.; Colina, L.; **Cortzen, I.**; Labiano, Á.; Piqueras, J.; & Rigopoulou, D., "*Extinction in the 11.2μm PAH band and the low $L_{11.2}/L_{IR}$ in ULIRGs*", Monthly Notices of the Royal Astronomical Society, submitted on Janury 20th 2020.

5. **Cortzen, I.**; Garrett, J.; Magdis, G. E.; Rigopoulou, D.; Valentino, F.; Pereira-Santaella, M.; Combes, F.; Alonso-Herrero, A.; Toft, S.; Daddi, E.; Elbaz, D.; Gómez-Guijarro, C.; Stockmann, M.; Huang, J.; & Kramer, C,
"*PAHs as tracers of the molecular gas in star-forming galaxies"*,
Monthly Notices of the Royal Astronomical Society, volume 482, Issue 2, p.1618-1633, 2019.
2019MNRAS.482.1618C

6. Gómez-Guijarro, C.; Toft, S.; Karim, A.; Magnelli, B.; Magdis, G. E.; Jiménez-Andrade, E. F.; Capak, P. L.; Fraternali, F.; Fujimoto, S.; Riechers, D. A.; Schinnerer, E.; Smolčić, V.; Aravena, M.; Bertoldi, F.; **Cortzen, I.**; Hasinger, G.; Hu, E. M.; Jones, G. C.; Koekemoer, A. M.; Lee, N.; McCracken, H. J.; Michałowski, M. J.; Navarrete, F.; Pović, M.; Puglisi, A.; Romano-Díaz, E.; Sheth, K.; Silverman, J. D.; Staguhn, J.; Steinhardt, C. L.; Stockmann, M.; Tanaka, M.; Valentino, F.; van Kampen, E.; & Zirm, A.,
"*Starburst to Quiescent from HST/ALMA: Stars and Dust Unveil Minor Mergers in Submillimeter Galaxies at $z \sim 4.5$*",
ApJ, Volume 856, Issue 2, 121, 2018.
2018ApJ...856..121G

7. Lee, N.; Sheth, K.; Scott, K. S.; Toft, S.; Magdis, G. E.; Damjanov, I.; Zahid, H. J.; Casey, C. M.; **Cortzen, I.**; Gómez-Guijarro, C.; Karim, A.; Leslie, S. K.; & Schinnerer, E.,
"*The fine line between normal and starburst galaxies*",
Monthly Notices of Royal Astronomical Society, volume 471, issue 2, p.2124-2142, 2017.
2017MNRAS.471.2124L

APPENDIX A

Appendix

A.1 General properties of the 5muses sample

Table A.1: General properties of the 5MUSES sample.

ID	R.A.	Decl.	z	$\log(L_{6.2})$	$\log(L_{7.7})$	$EW_{6.2}$	$\log(M_*)$	$\log(L_{\rm IR})$	$\log(M_{\rm d})$	$\log(M_{\rm H_2})$
	[hh:mm:ss]	[dd:mm:ss]		[$L_\odot$]	[$L_\odot$]	[µm]	[$M_\odot$]	[$L_\odot$]	[$M_\odot$]	[$M_\odot$]
2	02:15:03.5	-04:24:21.7	0.137	8.58 ± 0.19	9.19 ± 0.14	0.776 ± 0.009	–	10.86 ± 0.04	8.01 ± 0.28	10.01
4	02:15:57.1	-03:37:29.1	0.032	7.59 ± 0.08	8.09 ± 0.09	0.504 ± 0.048	9.97	9.83 ± 0.02	7.18 ± 0.29	9.18
5	02:16:38.2	-04:22:50.9	0.304	9.06 ± 0.24	9.48 ± 0.11	< 0.094	10.80	11.54 ± 0.02	–	–
6	02:16:40.7	-04:44:05.1	0.870	9.13 ± 1.62	–	< 0.045	–	12.70 ± 0.01	–	–
8	02:16:49.7	-04:25:54.8	0.143	9.01 ± 0.09	9.48 ± 0.08	1.107 ± 0.057	10.05	10.99 ± 0.01	7.29 ± 0.42	9.29
9	02:16:57.8	-03:24:59.8	0.137	6.72 ± 17.72	8.83 ± 0.32	< 0.062	9.94	10.84 ± 0.01	6.40 ± 0.42	8.40
10	02:17:29.1	-04:19:37.8	1.146	9.81 ± 0.56	–	< 0.113	11.06	12.74 ± 0.06	–	–
11	02:17:43.0	-04:36:25.2	0.784	9.60 ± 0.37	8.98 ± 2.23	< 0.080	11.53	12.00 ± 0.06	–	–
12	02:17:43.8	-05:17:51.8	0.031	8.10 ± 0.03	8.58 ± 0.03	0.645 ± 0.080	9.93	10.11 ± 0.01	7.29 ± 0.43	9.29
13	02:17:54.9	-03:58:26.5	0.226	9.56 ± 0.06	10.09 ± 0.04	0.530 ± 0.044	10.91	11.67 ± 0.01	8.76 ± 0.31	10.76
14	02:18:08.2	-04:58:45.3	0.712	9.73 ± 0.22	8.78 ± 2.74	< 0.049	10.60	12.32 ± 0.02	7.88 ± 0.43	9.88
16	02:18:30.6	-04:56:23.0	1.401	–	–	< 0.083	–	12.80 ± 0.02	8.36 ± 0.43	10.36
18	02:18:49.8	-05:21:58.2	0.292	9.60 ± 0.07	10.19 ± 0.06	0.571 ± 0.058	10.87	11.64 ± 0.03	8.35 ± 0.26	10.35
19	02:18:59.7	-04:02:37.2	0.199	7.87 ± 1.80	9.15 ± 0.08	< 0.160	–	11.13 ± 0.01	8.23 ± 0.01	10.23
20	02:19:09.6	-05:25:12.9	0.098	7.89 ± 0.50	8.66 ± 0.26	< 0.194	–	10.66 ± 0.01	6.70 ± 0.14	8.70
20	02:19:09.6	-05:25:12.9	0.098	7.89 ± 0.50	8.66 ± 0.26	< 0.194	10.37	10.66 ± 0.01	6.70 ± 0.14	8.70
21	02:19:12.7	-05:05:41.9	0.194	8.81 ± 0.21	9.35 ± 0.09	0.639 ± 0.041	9.86	11.04 ± 0.02	7.62 ± 0.24	9.62
22	02:19:16.1	-05:57:27.0	0.103	8.05 ± 0.35	8.60 ± 0.11	0.198 ± 0.027	10.98	10.66 ± 0.01	7.71 ± 0.15	9.71
23	02:19:28.3	-04:22:39.8	0.042	7.97 ± 0.06	8.47 ± 0.07	0.611 ± 0.053	10.23	9.98 ± 0.01	6.50 ± 0.24	8.50

Table A.1 continued from previous page

ID	R.A.	Decl.	z	$\log(L_{6.2})$	$\log(L_{7.7})$	$EW_{6.2}$	$\log(M_*)$	$\log(L_{\rm IR})$	$\log(M_{\rm d})$	$\log(M_{\rm H_2})$
	[hh:mm:ss]	[dd:mm:ss]		[$L_\odot$]	[$L_\odot$]	[µm]	[$M_\odot$]	[$L_\odot$]	[$M_\odot$]	[$M_\odot$]
25	02:19:38.7	-03:25:08.3	0.435	8.72 ± 0.81	9.20 ± 0.34	< 0.094	–	11.62 ± 0.01	7.18 ± 0.37	9.18
26	02:19:39.1	-05:11:33.9	0.151	8.85 ± 0.12	9.56 ± 0.05	0.101 ± 0.010	10.67	11.36 ± 0.01	7.88 ± 0.15	9.88
28	02:19:53.0	-05:18:24.2	0.072	8.97 ± 0.02	9.47 ± 0.02	0.781 ± 0.019	10.71	10.86 ± 0.04	7.75 ± 0.28	9.75
29	02:19:57.0	-05:24:40.5	0.081	8.60 ± 0.06	9.10 ± 0.04	0.699 ± 0.079	10.22	10.46 ± 0.01	7.65 ± 0.15	9.65
30	02:20:00.2	-04:39:47.7	0.350	8.94 ± 0.40	9.60 ± 0.24	0.137 ± 0.007	10.39	11.48 ± 0.06	–	–
31	02:20:05.9	-03:15:45.8	1.560	–	–	< 0.178	12.46	13.07 ± 0.01	8.92 ± 0.23	10.92
32	02:20:12.2	-03:41:11.8	0.166	8.00 ± 1.06	7.86 ± 0.77	< 0.079	10.24	10.40 ± 0.08	–	–
34	02:21:45.1	-05:32:07.4	0.008	5.48 ± 0.61	5.95 ± 0.72	0.391 ± 0.049	–	8.18 ± 0.01	5.43 ± 0.05	7.43
35	02:21:47.8	-02:57:30.7	0.068	8.80 ± 0.03	9.30 ± 0.03	0.714 ± 0.037	10.39	10.96 ± 0.04	8.09 ± 0.30	10.09
36	02:21:47.9	-04:46:13.5	0.025	6.37 ± 0.78	6.91 ± 0.67	0.809 ± 0.035	8.93	9.23 ± 0.02	6.52 ± 0.22	8.52
37	02:21:51.5	-03:29:11.8	0.164	8.96 ± 0.12	9.50 ± 0.06	0.748 ± 0.104	–	11.10 ± 0.02	7.91 ± 0.18	9.91
38	02:22:05.0	-05:05:37.0	0.258	9.60 ± 0.06	10.17 ± 0.05	0.696 ± 0.035	11.38	11.67 ± 0.03	8.50 ± 0.34	10.50
39	02:22:23.3	-04:43:19.9	0.073	8.12 ± 0.14	8.66 ± 0.10	0.356 ± 0.023	10.72	10.26 ± 0.03	7.33 ± 0.18	9.33
40	02:22:24.1	-05:05:50.4	0.149	8.98 ± 0.10	9.49 ± 0.06	0.602 ± 0.022	10.43	10.93 ± 0.01	7.55 ± 0.25	9.55
41	02:22:41.3	-04:56:52.1	0.139	8.42 ± 0.34	9.09 ± 0.19	0.308 ± 0.008	–	10.51 ± 0.01	7.84 ± 0.03	9.84
43	02:22:58.0	-04:18:40.8	0.239	9.14 ± 0.15	9.74 ± 0.10	0.205 ± 0.013	11.22	11.25 ± 0.02	8.32 ± 0.11	10.32
44	02:23:02.0	-05:23:35.9	0.708	10.11 ± 0.18	10.82 ± 0.06	< 0.054	11.00	12.67 ± 0.02	9.13 ± 0.39	11.13
45	02:23:09.3	-05:23:16.2	0.084	7.44 ± 0.76	8.19 ± 0.29	< 0.426	9.57	9.99 ± 0.01	6.28 ± 0.19	8.28
47	02:23:15.6	-04:06:06.0	0.199	8.91 ± 0.20	9.57 ± 0.07	0.486 ± 0.067	11.31	11.31 ± 0.02	8.33 ± 0.19	10.33
48	02:23:29.1	-04:32:09.6	0.144	8.61 ± 0.24	9.24 ± 0.15	0.585 ± 0.075	10.60	11.00 ± 0.01	7.87 ± 0.16	9.87

Table A.1 continued from previous page

ID	R.A.	Decl.	z	$\log(L_{6.2})$	$\log(L_{7.7})$	$EW_{6.2}$	$\log(M_*)$	$\log(L_{\mathrm{IR}})$	$\log(M_{\mathrm{d}})$	$\log(M_{\mathrm{H_2}})$
	[hh:mm:ss]	[dd:mm:ss]		[$\mathrm{L_\odot}$]	[$\mathrm{L_\odot}$]	[µm]	[$\mathrm{M_\odot}$]	[$\mathrm{L_\odot}$]	[$\mathrm{M_\odot}$]	[$\mathrm{M_\odot}$]
49	02:23:34.7	-03:52:29.4	0.176	8.82 ± 0.20	9.45 ± 0.09	0.966 ± 0.129	10.20	11.02 ± 0.01	7.43 ± 0.33	9.43
50	02:23:45.0	-05:42:34.5	0.143	9.17 ± 0.06	9.77 ± 0.04	0.689 ± 0.003	10.74	11.08 ± 0.04	7.88 ± 0.22	9.88
51	02:23:56.5	-02:54:31.1	0.451	9.37 ± 0.26	10.19 ± 0.16	0.058 ± 0.004	–	11.71 ± 0.01	7.25 ± 0.39	9.25
52	02:24:13.6	-04:22:27.8	0.116	8.88 ± 0.07	9.37 ± 0.05	0.626 ± 0.062	10.47	10.90 ± 0.02	7.77 ± 0.21	9.77
53	02:24:22.5	-04:02:30.6	0.171	8.48 ± 0.36	9.19 ± 0.05	0.414 ± 0.007	10.68	11.09 ± 0.01	7.58 ± 0.25	9.58
54	02:24:31.6	-05:28:18.8	2.068	–	–	–	12.43	13.35 ± 0.01	9.47 ± 0.13	11.47
55	02:24:34.3	-04:15:31.2	0.259	9.58 ± 0.05	10.14 ± 0.03	0.584 ± 0.019	11.07	11.57 ± 0.02	8.29 ± 0.24	10.29
56	02:24:39.0	-04:27:06.4	0.252	9.02 ± 0.20	9.51 ± 0.19	0.156 ± 0.034	11.09	11.21 ± 0.02	9.08 ± 0.01	11.08
57	02:24:47.0	-04:08:51.4	0.096	8.89 ± 0.05	9.48 ± 0.03	0.456 ± 0.012	11.07	10.89 ± 0.02	8.10 ± 0.29	10.10
58	02:24:57.6	-04:14:18.0	0.063	8.52 ± 0.04	9.13 ± 0.03	0.476 ± 0.035	10.65	10.69 ± 0.04	7.80 ± 0.34	9.80
60	02:25:07.4	-04:18:35.8	0.105	8.37 ± 0.16	8.89 ± 0.09	0.632 ± 0.062	10.48	10.61 ± 0.02	7.98 ± 0.22	9.98
61	02:25:08.3	-05:39:17.7	0.293	8.70 ± 0.62	9.23 ± 0.57	0.025 ± 0.002	11.25	11.55 ± 0.05	–	–
62	02:25:22.6	-04:54:52.2	0.144	9.01 ± 0.10	9.61 ± 0.07	0.719 ± 0.007	11.01	11.27 ± 0.01	8.22 ± 0.29	10.22
63	02:25:36.4	-05:00:11.6	0.053	8.97 ± 0.02	9.52 ± 0.01	0.709 ± 0.051	10.72	11.02 ± 0.05	8.00 ± 0.31	10.00
64	02:25:48.2	-05:00:51.5	0.150	8.72 ± 0.15	9.41 ± 0.06	0.297 ± 0.051	10.70	11.15 ± 0.01	7.71 ± 0.36	9.72
65	02:25:49.8	-04:00:24.7	0.044	8.44 ± 0.03	9.02 ± 0.03	0.438 ± 0.009	10.52	10.62 ± 0.01	7.39 ± 0.30	9.39
66	02:26:00.0	-05:01:45.3	0.205	9.29 ± 0.13	9.84 ± 0.07	0.916 ± 0.027	10.98	11.28 ± 0.03	8.27 ± 0.22	10.27
67	02:26:02.9	-04:53:06.8	0.056	8.20 ± 0.08	8.70 ± 0.09	0.669 ± 0.028	10.15	10.13 ± 0.02	7.25 ± 0.22	9.25
68	02:26:03.6	-04:59:03.8	0.055	8.34 ± 0.04	8.89 ± 0.04	0.634 ± 0.047	–	10.59 ± 0.03	7.68 ± 0.34	9.68
69	02:26:17.4	-05:04:43.5	0.057	8.68 ± 0.03	9.27 ± 0.03	0.168 ± 0.005	11.23	10.72 ± 0.01	7.11 ± 0.32	9.11

Table A.1 continued from previous page

ID	R.A.	Decl.	z	$\log(L_{6.2})$	$\log(L_{7.7})$	$EW_{6.2}$	$\log(M_*)$	$\log(L_{\rm IR})$	$\log(M_{\rm d})$	$\log(M_{\rm H_2})$
	[hh:mm:ss]	[dd:mm:ss]		[$L_\odot$]	[$L_\odot$]	[μm]	[$M_\odot$]	[$L_\odot$]	[$M_\odot$]	[$M_\odot$]
70	02:26:37.8	-03:58:41.7	0.070	8.22 ± 0.13	8.81 ± 0.10	0.377 ± 0.019	10.37	10.42 ± 0.03	7.27 ± 0.15	9.27
71	02:26:55.9	-04:03:02.5	0.135	8.68 ± 0.19	9.19 ± 0.09	1.026 ± 0.179	10.18	10.66 ± 0.01	7.15 ± 0.17	9.15
73	02:27:20.7	-04:45:37.2	0.055	8.87 ± 0.02	9.41 ± 0.01	0.625 ± 0.032	10.61	11.02 ± 0.02	7.86 ± 0.32	9.86
74	02:27:38.5	-04:47:02.8	0.173	9.00 ± 0.13	9.65 ± 0.04	0.918 ± 0.032	10.79	11.07 ± 0.01	7.51 ± 0.35	9.51
75	02:27:41.6	-04:56:50.6	0.055	8.45 ± 0.04	8.98 ± 0.02	0.627 ± 0.004	10.22	10.51 ± 0.02	7.79 ± 0.36	9.79
77	10:32:37.4	+58:08:46.0	0.251	9.45 ± 0.06	10.14 ± 0.03	0.394 ± 0.060	11.10	11.81 ± 0.01	8.82 ± 0.39	10.82
79	10:34:50.5	+58:44:18.2	0.091	8.83 ± 0.04	9.35 ± 0.03	0.643 ± 0.047	10.14	10.85 ± 0.01	7.86 ± 0.23	9.86
80	10:35:13.7	+57:34:44.6	1.537	10.65 ± 0.12	10.91 ± 0.13	< 0.171	10.74	13.13 ± 0.02	9.39 ± 0.23	11.39
81	10:35:27.2	+58:37:12.0	0.885	9.84 ± 0.21	10.29 ± 0.11	0.080 ± 0.010	11.18	12.57 ± 0.01	9.67 ± 0.05	11.67
82	10:35:31.5	+58:12:34.2	0.176	9.17 ± 0.09	9.76 ± 0.06	0.574 ± 0.018	10.75	11.27 ± 0.01	8.27 ± 0.24	10.27
83	10:35:42.8	+58:33:13.1	0.087	8.51 ± 0.08	9.04 ± 0.07	0.761 ± 0.002	9.70	10.48 ± 0.01	7.12 ± 0.29	9.12
84	10:36:01.8	+58:18:36.2	0.100	8.43 ± 0.14	8.90 ± 0.11	0.421 ± 0.012	10.82	10.54 ± 0.02	7.86 ± 0.24	9.86
85	10:36:06.5	+58:18:29.7	0.210	8.90 ± 0.27	9.56 ± 0.10	< 0.068	10.18	11.41 ± 0.02	–	–
86	10:36:46.4	+58:43:30.6	0.140	8.87 ± 0.10	9.47 ± 0.07	0.549 ± 0.020	10.66	10.94 ± 0.01	7.88 ± 0.19	9.88
87	10:37:02.0	+57:44:14.8	0.577	9.30 ± 0.28	8.86 ± 1.48	< 0.065	–	12.06 ± 0.05	–	–
88	10:37:24.7	+58:05:12.9	1.517	–	–	< 0.158	11.71	13.02 ± 0.06	–	–
89	10:38:03.4	+57:27:01.5	1.285	–	–	< 0.086	11.34	13.20 ± 0.01	9.15 ± 0.21	11.15
90	10:38:13.9	+58:00:47.4	0.205	7.62 ± 3.32	8.82 ± 0.14	< 0.335	10.18	11.12 ± 0.01	7.83 ± 0.13	9.83
91	10:38:18.2	+58:35:56.5	0.129	8.29 ± 0.34	9.07 ± 0.09	0.312 ± 0.018	9.50	10.50 ± 0.03	–	–
93	10:38:56.2	+57:03:33.9	0.178	8.44 ± 0.52	9.22 ± 0.20	0.338 ± 0.011	10.72	10.74 ± 0.02	6.56 ± 0.22	8.56

Table A.1 continued from previous page

ID	R.A.	Decl.	z	$\log(L_{6.2})$	$\log(L_{7.7})$	$EW_{6.2}$	$\log(M_*)$	$\log(L_{\mathrm{IR}})$	$\log(M_{\mathrm{d}})$	$\log(M_{\mathrm{H_2}})$
	[hh:mm:ss]	[dd:mm:ss]		[$\mathrm{L_\odot}$]	[$\mathrm{L_\odot}$]	[µm]	[$\mathrm{M_\odot}$]	[$\mathrm{L_\odot}$]	[$\mathrm{M_\odot}$]	[$\mathrm{M_\odot}$]
97	10:40:16.3	+57:08:46.1	0.118	8.86 ± 0.08	9.43 ± 0.05	0.661 ± 0.003	10.68	10.80 ± 0.01	7.73 ± 0.13	9.73
98	10:40:58.8	+58:17:03.4	0.072	7.13 ± 0.94	7.48 ± 0.43	< 0.119	9.43	9.91 ± 0.01	7.07 ± 0.01	9.07
99	10:41:31.8	+59:22:58.4	0.925	–	–	< 0.061	11.02	12.32 ± 0.01	8.86 ± 0.04	10.86
100	10:41:32.5	+56:59:53.0	0.346	9.61 ± 0.07	10.21 ± 0.05	0.454 ± 0.044	9.85	11.75 ± 0.01	7.94 ± 0.32	9.94
101	10:41:59.8	+58:58:56.4	0.360	9.39 ± 0.15	10.13 ± 0.07	< 0.127	10.86	11.91 ± 0.01	8.31 ± 0.05	10.31
102	10:42:55.7	+57:55:49.8	1.468	10.32 ± 0.20	–	< 0.067	11.81	12.81 ± 0.01	8.38 ± 0.40	10.38
103	10:43:03.5	+58:57:18.1	0.595	8.74 ± 1.13	9.68 ± 0.25	< 0.066	11.67	11.90 ± 0.05	–	–
105	10:44:32.9	+56:40:41.6	0.068	8.57 ± 0.04	9.11 ± 0.03	0.637 ± 0.117	10.79	10.94 ± 0.02	8.04 ± 0.31	10.04
105	10:44:32.9	+56:40:41.6	0.067	8.57 ± 0.04	9.11 ± 0.03	0.637 ± 0.117	–	10.94 ± 0.02	8.04 ± 0.31	10.04
106	10:44:38.2	+56:22:10.8	0.025	8.34 ± 0.01	8.92 ± 0.01	0.509 ± 0.027	10.74	10.44 ± 0.04	7.46 ± 0.35	9.46
107	10:44:54.1	+57:44:25.8	0.118	9.04 ± 0.05	9.59 ± 0.02	0.585 ± 0.096	11.03	11.00 ± 0.07	8.39 ± 0.17	10.39
108	10:45:01.7	+57:11:11.4	0.390	9.14 ± 0.18	9.73 ± 0.14	< 0.164	11.41	11.60 ± 0.05	–	–
109	10:45:16.0	+59:23:04.7	0.322	8.82 ± 0.37	9.47 ± 0.26	0.094 ± 0.005	10.87	11.44 ± 0.01	7.65 ± 0.33	9.65
110	10:46:43.3	+58:47:15.1	0.140	8.78 ± 0.10	9.34 ± 0.05	0.522 ± 0.017	11.08	10.90 ± 0.02	8.37 ± 0.26	10.37
112	10:47:05.1	+59:07:28.5	0.391	8.78 ± 0.44	7.15 ± 18.55	0.032 ± 0.003	10.03	11.58 ± 0.01	7.86 ± 0.30	9.86
114	10:47:29.9	+57:28:42.9	0.230	9.64 ± 0.04	10.15 ± 0.02	0.477 ± 0.052	11.14	11.54 ± 0.02	8.75 ± 0.29	10.75
115	10:48:37.8	+58:26:42.2	0.232	9.67 ± 0.03	10.20 ± 0.02	0.729 ± 0.022	10.68	11.66 ± 0.02	8.66 ± 0.39	10.66
116	10:48:39.7	+55:53:56.5	2.043	10.70 ± 0.24	11.91 ± 0.05	–	–	13.46 ± 0.25	–	–
117	10:48:43.9	+58:03:41.3	0.162	8.88 ± 0.11	9.52 ± 0.03	0.838 ± 0.029	10.47	11.02 ± 0.01	7.68 ± 0.20	9.68
118	10:49:07.2	+56:57:15.4	0.072	8.82 ± 0.02	9.31 ± 0.02	0.805 ± 0.014	10.10	10.62 ± 0.01	7.60 ± 0.27	9.60

Table A.1 continued from previous page

ID	R.A.	Decl.	z	$\log(L_{6.2})$	$\log(L_{7.7})$	$EW_{6.2}$	$\log(M_*)$	$\log(L_{\rm IR})$	$\log(M_{\rm d})$	$\log(M_{\rm H_2})$
	[hh:mm:ss]	[dd:mm:ss]		[$L_\odot$]	[$L_\odot$]	[μm]	[$M_\odot$]	[$L_\odot$]	[$M_\odot$]	[$M_\odot$]
119	10:49:18.3	+56:25:13.0	0.330	9.31 ± 0.10	10.01 ± 0.05	0.037 ± 0.001	9.97	11.20 ± 0.08	–	–
123	10:50:06.0	+56:15:00.0	0.119	8.98 ± 0.05	9.54 ± 0.04	0.714 ± 0.097	11.12	11.13 ± 0.03	7.77 ± 0.24	9.77
124	10:50:47.8	+59:03:48.4	0.131	8.74 ± 0.10	9.29 ± 0.06	0.623 ± 0.015	10.58	10.86 ± 0.04	8.12 ± 0.24	10.12
126	10:50:58.8	+56:05:50.0	0.125	8.44 ± 0.22	8.94 ± 0.17	0.496 ± 0.054	10.63	10.41 ± 0.05	–	–
127	10:51:06.1	+59:16:25.3	0.768	9.89 ± 0.14	10.17 ± 0.13	0.078 ± 0.003	10.54	12.23 ± 0.01	8.83 ± 0.04	10.83
128	10:51:28.1	+57:35:02.4	0.073	8.31 ± 0.08	8.89 ± 0.04	0.695 ± 0.081	9.98	10.40 ± 0.01	7.07 ± 0.24	9.07
130	10:51:58.5	+59:06:52.1	1.814	–	–	< 0.093	12.75	13.16 ± 0.01	9.40 ± 0.16	11.40
131	10:52:00.3	+59:19:33.8	0.115	8.30 ± 0.25	8.94 ± 0.11	0.297 ± 0.036	10.24	10.78 ± 0.01	7.28 ± 0.28	9.28
132	10:52:06.6	+58:09:47.1	0.117	9.33 ± 0.03	9.88 ± 0.02	0.661 ± 0.009	10.67	11.31 ± 0.01	8.49 ± 0.31	10.49
133	10:53:36.9	+58:03:50.7	0.460	9.77 ± 0.09	10.37 ± 0.06	0.368 ± 0.001	11.02	11.92 ± 0.01	8.99 ± 0.09	10.99
135	10:54:04.1	+57:40:19.7	1.101	9.88 ± 0.35	–	< 0.084	10.94	12.50 ± 0.02	8.56 ± 0.14	10.56
136	10:54:21.7	+58:23:44.7	0.204	9.20 ± 0.11	9.77 ± 0.06	0.074 ± 0.001	11.41	11.47 ± 0.01	8.90 ± 0.08	10.90
138	10:56:04.8	+57:42:30.0	1.211	9.77 ± 0.72	–	< 0.146	11.16	12.98 ± 0.02	8.50 ± 0.42	10.50
139	10:56:37.0	+57:34:49.4	0.047	7.89 ± 0.11	8.52 ± 0.08	0.444 ± 0.060	10.06	10.22 ± 0.01	7.25 ± 0.28	9.25
140	10:56:41.8	+58:00:46.0	0.130	9.08 ± 0.05	9.62 ± 0.03	0.686 ± 0.014	10.52	11.00 ± 0.02	7.99 ± 0.39	9.99
141	10:57:05.4	+58:04:37.4	0.140	8.72 ± 0.13	9.47 ± 0.07	0.097 ± 0.001	11.15	11.19 ± 0.02	8.29 ± 0.28	10.29
142	10:57:33.5	+56:57:37.5	0.086	8.31 ± 0.12	8.81 ± 0.11	0.454 ± 0.023	10.29	10.32 ± 0.01	6.83 ± 0.33	8.83
143	10:57:40.6	+57:06:16.5	0.073	8.21 ± 0.10	8.76 ± 0.09	0.503 ± 0.058	10.38	10.26 ± 0.01	7.31 ± 0.19	9.31
144	10:58:29.3	+58:04:39.3	0.136	7.90 ± 0.64	8.38 ± 0.15	0.452 ± 0.075	10.09	10.56 ± 0.03	–	–
145	10:58:54.1	+57:41:30.0	0.232	8.98 ± 0.14	9.44 ± 0.11	0.222 ± 0.031	10.94	11.10 ± 0.07	–	–

Table A.1 continued from previous page

ID	R.A.	Decl.	z	$\log(L_{6.2})$	$\log(L_{7.7})$	$EW_{6.2}$	$\log(M_*)$	$\log(L_{\mathrm{IR}})$	$\log(M_{\mathrm{d}})$	$\log(M_{\mathrm{H_2}})$
	[hh:mm:ss]	[dd:mm:ss]		[$\mathrm{L_\odot}$]	[$\mathrm{L_\odot}$]	[µm]	[$\mathrm{M_\odot}$]	[$\mathrm{L_\odot}$]	[$\mathrm{M_\odot}$]	[$\mathrm{M_\odot}$]
146	10:59:03.5	+57:21:55.1	0.119	8.30 ± 0.27	9.18 ± 0.09	< 0.261	10.73	10.87 ± 0.02	7.55 ± 0.16	9.55
147	10:59:51.7	+58:18:02.9	2.335	–	–	–	13.77	13.40 ± 0.02	9.29 ± 0.19	11.29
148	11:00:00.0	+57:48:48.2	0.453	9.35 ± 0.15	9.75 ± 0.18	< 0.052	10.54	11.78 ± 0.01	8.76 ± 0.01	10.76
149	11:00:02.1	+57:31:42.2	0.387	9.92 ± 0.05	10.43 ± 0.05	0.496 ± 0.027	10.50	12.02 ± 0.01	8.26 ± 0.41	10.26
151	11:01:25.0	+57:43:15.9	0.243	8.86 ± 0.23	9.52 ± 0.15	0.545 ± 0.058	11.30	11.26 ± 0.01	8.22 ± 0.13	10.22
152	11:01:33.8	+57:52:06.6	0.277	9.68 ± 0.04	10.25 ± 0.03	0.509 ± 0.057	11.41	11.81 ± 0.01	8.75 ± 0.27	10.75
153	11:02:23.6	+57:44:36.2	0.226	8.23 ± 1.16	8.90 ± 0.14	< 0.093	9.61	11.25 ± 0.01	8.60 ± 0.04	10.60
154	11:02:35.0	+57:46:55.7	0.226	9.33 ± 0.11	9.82 ± 0.08	0.523 ± 0.066	10.47	11.46 ± 0.01	7.83 ± 0.42	9.83
155	15:58:32.9	+54:44:27.2	0.350	–	–	0.086 ± 0.001	11.14	11.52 ± 0.03	–	–
156	15:58:33.3	+54:59:37.2	0.340	9.51 ± 0.09	10.29 ± 0.03	0.327 ± 0.012	10.17	12.10 ± 0.03	–	10.76
157	15:59:36.1	+54:42:03.8	0.308	–	–	< 0.060	9.74	11.32 ± 0.06	–	–
158	16:00:38.8	+55:10:18.7	0.145	9.07 ± 0.05	9.71 ± 0.03	0.637 ± 0.020	10.99	11.45 ± 0.04	–	10.37
160	16:01:14.5	+55:13:04.1	0.220	–	–	< 0.079	10.94	10.82 ± 0.06	–	–
162	16:01:28.5	+54:45:21.4	0.728	–	–	< 0.034	10.57	12.47 ± 0.01	–	–
163	16:03:22.8	+54:42:37.3	0.215	–	–	0.687 ± 0.070	10.36	11.35 ± 0.03	–	–
165	16:03:41.3	+55:26:12.7	0.146	–	–	0.610 ± 0.012	11.10	11.11 ± 0.03	–	–
166	16:03:58.2	+55:55:04.4	0.322	–	–	0.406 ± 0.030	11.02	11.56 ± 0.06	–	–
167	16:04:01.2	+55:15:02.7	0.182	–	–	< 0.112	10.80	11.11 ± 0.05	–	–
168	16:04:08.2	+54:25:31.2	0.260	9.53 ± 0.05	10.09 ± 0.04	0.604 ± 0.054	11.02	11.52 ± 0.02	8.29 ± 0.24	10.29
169	16:04:08.3	+54:58:13.1	0.064	8.78 ± 0.02	9.33 ± 0.02	0.602 ± 0.009	10.82	10.83 ± 0.03	–	9.58

Table A.1 continued from previous page

ID	R.A.	Decl.	z	$\log(L_{6.2})$	$\log(L_{7.7})$	$EW_{6.2}$	$\log(M_*)$	$\log(L_{\rm IR})$	$\log(M_{\rm d})$	$\log(M_{\rm H_2})$
	[hh:mm:ss]	[dd:mm:ss]		[$L_\odot$]	[$L_\odot$]	[μm]	[$M_\odot$]	[$L_\odot$]	[$M_\odot$]	[$M_\odot$]
171	16:04:40.6	+55:34:09.3	0.078	8.77 ± 0.02	9.27 ± 0.02	0.521 ± 0.035	10.93	11.10 ± 0.04	–	9.99
173	16:06:30.6	+54:20:07.4	0.820	9.66 ± 0.23	9.10 ± 1.43	< 0.052	10.41	11.91 ± 0.10	–	–
174	16:06:55.4	+53:40:16.9	0.214	8.71 ± 0.44	9.22 ± 0.24	< 0.086	10.69	11.26 ± 0.02	8.18 ± 0.03	10.18
176	16:07:30.4	+55:49:05.6	0.118	–	–	0.835 ± 0.100	10.07	10.81 ± 0.03	–	–
177	16:07:43.1	+55:44:16.5	0.118	–	–	0.752 ± 0.049	10.85	11.13 ± 0.03	–	–
178	16:08:01.8	+55:53:59.7	0.062	–	–	1.057 ± 0.011	9.63	10.24 ± 0.04	–	–
179	16:08:03.7	+54:53:02.0	0.053	8.15 ± 0.05	8.77 ± 0.03	0.373 ± 0.019	11.08	10.35 ± 0.04	7.78 ± 0.43	9.78
180	16:08:19.6	+55:33:14.3	0.115	–	–	0.337 ± 0.005	10.66	10.83 ± 0.02	–	–
181	16:08:32.6	+55:29:27.0	0.065	8.39 ± 0.06	8.96 ± 0.06	0.844 ± 0.121	10.53	10.27 ± 0.02	7.58 ± 0.24	9.58
183	16:08:39.7	+55:23:30.7	0.064	8.46 ± 0.04	8.96 ± 0.03	0.964 ± 0.029	9.87	10.33 ± 0.02	–	–
184	16:08:47.0	+56:37:02.2	0.590	–	–	0.045 ± 0.001	10.20	12.21 ± 0.02	–	–
185	16:08:58.4	+55:30:10.3	0.066	7.94 ± 0.15	8.49 ± 0.12	0.586 ± 0.104	10.68	10.34 ± 0.01	7.52 ± 0.29	9.52
186	16:08:58.7	+56:36:35.7	0.117	–	–	0.566 ± 0.050	10.45	10.77 ± 0.04	–	–
187	16:09:07.6	+55:24:28.4	0.065	8.48 ± 0.05	9.07 ± 0.02	0.670 ± 0.003	10.29	10.56 ± 0.03	7.76 ± 0.34	9.76
188	16:09:08.3	+55:22:41.5	0.084	8.76 ± 0.04	9.26 ± 0.04	0.824 ± 0.056	10.59	10.62 ± 0.01	7.80 ± 0.31	9.80
189	16:09:26.7	+55:16:42.3	0.068	8.20 ± 0.07	8.74 ± 0.04	0.507 ± 0.058	10.40	10.30 ± 0.02	7.53 ± 0.29	9.53
190	16:09:30.5	+56:35:09.1	0.030	–	–	0.428 ± 0.028	9.37	9.22 ± 0.06	–	–
191	16:09:31.6	+54:18:27.4	0.082	8.51 ± 0.09	9.09 ± 0.06	0.497 ± 0.033	10.63	10.61 ± 0.04	7.81 ± 0.28	9.81
192	16:09:37.5	+54:12:59.3	0.086	8.79 ± 0.04	9.28 ± 0.02	0.681 ± 0.018	10.80	10.68 ± 0.03	7.96 ± 0.36	9.96
192	16:09:37.5	+54:12:59.3	0.086	8.79 ± 0.04	9.28 ± 0.02	0.681 ± 0.018	–	10.68 ± 0.03	7.96 ± 0.36	9.96

Table A.1 continued from previous page

ID	R.A.	Decl.	z	$\log(L_{6.2})$	$\log(L_{7.7})$	$EW_{6.2}$	$\log(M_*)$	$\log(L_{\mathrm{IR}})$	$\log(M_{\mathrm{d}})$	$\log(M_{\mathrm{H_2}})$
	[hh:mm:ss]	[dd:mm:ss]		[$\mathrm{L_\odot}$]	[$\mathrm{L_\odot}$]	[µm]	[$\mathrm{M_\odot}$]	[$\mathrm{L_\odot}$]	[$\mathrm{M_\odot}$]	[$\mathrm{M_\odot}$]
193	16:11:03.7	+54:43:22.1	0.063	8.08 ± 0.10	8.66 ± 0.08	0.536 ± 0.018	10.38	10.20 ± 0.02	7.56 ± 0.28	9.56
194	16:11:19.4	+55:33:55.4	0.224	< 8.34	9.57 ± 0.12	< 0.100	11.19	11.76 ± 0.03	–	10.47
195	16:11:23.4	+54:51:58.2	0.078	8.44 ± 0.07	8.98 ± 0.05	0.516 ± 0.002	10.52	10.40 ± 0.02	7.36 ± 0.24	9.36
196	16:12:23.4	+54:03:39.2	0.138	8.86 ± 0.08	9.49 ± 0.03	0.839 ± 0.136	10.60	11.05 ± 0.01	7.78 ± 0.20	9.78
197	16:12:33.4	+54:56:30.5	0.083	8.36 ± 0.10	8.93 ± 0.08	0.560 ± 0.083	10.99	10.72 ± 0.03	8.22 ± 0.32	10.22
198	16:12:41.1	+54:39:56.8	0.035	7.49 ± 0.07	7.97 ± 0.08	0.841 ± 0.078	9.30	9.54 ± 0.01	6.44 ± 0.17	8.44
199	16:12:49.5	+56:42:32.8	0.336	–	–	0.411 ± 0.036	10.52	11.60 ± 0.08	–	–
200	16:12:50.9	+53:23:05.0	0.048	8.16 ± 0.04	8.79 ± 0.03	0.405 ± 0.074	10.48	10.41 ± 0.02	7.20 ± 0.33	9.20
202	16:12:54.2	+54:55:25.4	0.065	8.54 ± 0.03	9.11 ± 0.02	0.624 ± 0.015	11.22	10.59 ± 0.04	8.17 ± 0.43	10.17
203	16:13:01.8	+55:21:23.1	0.012	–	–	0.563 ± 0.044	9.91	9.47 ± 0.05	–	–
204	16:13:57.0	+53:41:05.3	0.180	8.47 ± 0.38	9.03 ± 0.19	0.106 ± 0.004	10.85	10.86 ± 0.01	9.05 ± 0.04	11.05
205	16:14:03.0	+56:07:57.0	0.063	–	–	0.746 ± 0.052	10.73	10.79 ± 0.06	–	–
207	16:14:06.9	+55:14:52.0	0.564	–	–	0.047 ± 0.010	11.23	12.18 ± 0.03	–	–
208	16:14:11.5	+54:05:54.3	0.305	9.37 ± 0.10	9.95 ± 0.08	0.587 ± 0.123	10.60	11.73 ± 0.03	8.30 ± 0.28	10.30
209	16:14:49.1	+55:45:12.9	0.064	–	–	0.148 ± 0.007	10.98	10.26 ± 0.03	–	–
210	16:15:21.8	+54:31:48.3	0.474	9.31 ± 0.24	9.69 ± 0.31	< 0.058	10.42	11.59 ± 0.01	8.46 ± 0.02	10.46
211	16:15:28.1	+53:44:02.5	0.133	–	–	0.476 ± 0.071	10.77	11.01 ± 0.03	–	–
212	16:15:42.1	+56:18:14.7	0.109	–	–	< 0.150	10.77	10.67 ± 0.04	–	–
214	16:15:46.5	+55:03:31.0	0.087	–	–	0.169 ± 0.003	10.05	10.26 ± 0.03	–	–
215	16:15:48.3	+53:45:51.1	0.147	–	–	0.512 ± 0.104	10.62	11.18 ± 0.03	–	–

Table A.1 continued from previous page

ID	R.A.	Decl.	z	$\log(L_{6.2})$	$\log(L_{7.7})$	$EW_{6.2}$	$\log(M_*)$	$\log(L_{\rm IR})$	$\log(M_{\rm d})$	$\log(M_{\rm H_2})$
	[hh:mm:ss]	[dd:mm:ss]		[$L_\odot$]	[$L_\odot$]	[μm]	[$M_\odot$]	[$L_\odot$]	[$M_\odot$]	[$M_\odot$]
216	16:15:51.5	+54:15:36.0	0.215	9.31 ± 0.12	9.85 ± 0.06	0.445 ± 0.049	10.71	11.49 ± 0.01	8.36 ± 0.30	10.36
217	16:16:44.4	+53:37:34.3	0.147	–	–	0.828 ± 0.080	10.50	11.19 ± 0.02	–	–
219	16:16:45.9	+54:25:54.4	0.223	9.12 ± 0.13	9.54 ± 0.10	0.162 ± 0.002	10.80	11.28 ± 0.01	8.09 ± 0.03	10.09
220	16:16:56.0	+54:53:07.1	0.418	–	–	0.391 ± 0.039	9.93	11.81 ± 0.05	–	–
221	16:17:00.0	+56:00:27.2	0.063	–	–	0.517 ± 0.049	10.97	10.66 ± 0.02	–	–
222	16:17:12.3	+55:18:53.0	0.037	–	–	0.714 ± 0.030	9.05	9.53 ± 0.06	–	–
223	16:17:16.6	+55:09:20.3	0.092	–	–	0.728 ± 0.022	10.40	10.65 ± 0.04	–	–
225	16:17:48.1	+55:18:31.1	0.145	8.78 ± 0.04	9.33 ± 0.03	0.363 ± 0.030	10.99	11.13 ± 0.05	–	10.31
227	16:17:59.2	+54:15:01.3	0.134	8.39 ± 0.32	9.70 ± 0.03	0.137 ± 0.006	10.74	11.15 ± 0.01	7.41 ± 0.11	9.41
228	16:18:09.4	+55:15:22.1	0.136	–	–	0.137 ± 0.002	10.89	10.71 ± 0.05	–	–
229	16:18:19.3	+54:18:59.1	0.082	8.87 ± 0.03	9.46 ± 0.02	0.472 ± 0.005	11.36	11.16 ± 0.04	8.31 ± 0.43	10.31
230	16:18:23.1	+55:27:21.4	0.084	9.28 ± 0.02	9.79 ± 0.01	0.613 ± 0.016	10.46	11.13 ± 0.03	–	9.98
231	16:18:27.7	+55:22:08.6	0.083	–	–	0.673 ± 0.082	10.36	10.74 ± 0.05	–	–
232	16:18:43.4	+55:44:33.1	0.153	–	–	0.618 ± 0.046	10.65	11.29 ± 0.03	–	–
233	16:18:48.0	+53:58:37.6	0.079	–	–	0.124 ± 0.005	11.18	10.49 ± 0.09	–	–
234	16:19:29.6	+54:18:41.9	0.100	8.80 ± 0.03	9.36 ± 0.02	0.487 ± 0.048	10.47	11.07 ± 0.02	–	10.12
235	16:19:50.5	+54:37:15.4	0.146	–	–	0.761 ± 0.041	10.81	11.14 ± 0.03	–	–
239	16:20:34.0	+54:23:23.5	0.133	–	–	0.622 ± 0.058	10.76	11.07 ± 0.05	–	–
240	16:20:38.1	+55:35:21.5	0.191	–	–	0.716 ± 0.099	10.67	11.39 ± 0.03	–	–
241	16:20:58.8	+54:25:13.2	0.082	–	–	0.880 ± 0.005	10.76	11.11 ± 0.03	–	–

Table A.1 continued from previous page

ID	R.A.	Decl.	z	$\log(L_{6.2})$	$\log(L_{7.7})$	$EW_{6.2}$	$\log(M_*)$	$\log(L_{\mathrm{IR}})$	$\log(M_{\mathrm{d}})$	$\log(M_{\mathrm{H_2}})$
	[hh:mm:ss]	[dd:mm:ss]		[$\mathrm{L}_\odot$]	[$\mathrm{L}_\odot$]	[µm]	[$\mathrm{M}_\odot$]	[$\mathrm{L}_\odot$]	[$\mathrm{M}_\odot$]	[$\mathrm{M}_\odot$]
242	16:20:59.0	+54:26:01.5	0.046	–	–	0.732 ± 0.068	8.87	10.20 ± 0.07	–	–
243	16:21:10.5	+54:41:16.8	0.155	–	–	0.175 ± 0.008	10.85	10.92 ± 0.06	–	–
244	16:21:28.0	+55:14:52.9	0.100	–	–	0.707 ± 0.091	10.69	10.74 ± 0.02	–	–
245	16:21:33.0	+55:18:29.9	0.238	–	–	0.494 ± 0.081	10.12	11.27 ± 0.13	–	–
247	16:21:50.9	+55:30:08.9	0.099	–	–	0.911 ± 0.009	10.60	10.82 ± 0.02	–	–
248	16:22:10.9	+55:02:53.8	0.034	–	–	0.527 ± 0.062	10.67	10.58 ± 0.04	–	–
249	16:22:14.8	+55:06:14.2	0.237	9.49 ± 0.03	10.02 ± 0.02	0.470 ± 0.021	10.96	11.67 ± 0.02	–	10.33
250	16:23:13.1	+55:11:11.6	0.237	9.71 ± 0.02	10.23 ± 0.01	0.405 ± 0.001	11.29	11.67 ± 0.02	–	10.84
251	16:30:01.5	+41:09:52.9	0.121	–	–	0.697 ± 0.127	10.72	10.84 ± 0.01	–	–
252	16:31:11.3	+40:48:05.2	0.258	–	–	0.042 ± 0.002	9.92	11.30 ± 0.24	–	–
253	16:31:28.6	+40:45:36.0	0.181	–	–	0.170 ± 0.009	9.94	11.13 ± 0.04	–	–
254	16:32:20.4	+40:23:34.4	0.079	–	–	0.602 ± 0.002	–	10.79 ± 0.05	–	–
255	16:33:08.3	+40:33:21.6	0.404	–	–	0.164 ± 0.013	10.59	11.82 ± 0.05	–	–
256	16:33:10.9	+40:56:41.4	0.136	–	–	0.725 ± 0.022	10.10	10.86 ± 0.03	–	–
258	16:33:17.6	+40:34:43.6	0.378	–	–	< 0.073	10.98	11.46 ± 0.03	–	–
260	16:33:35.9	+40:15:29.1	0.028	–	–	0.954 ± 0.037	9.84	10.07 ± 0.04	–	–
261	16:33:59.1	+40:53:04.7	0.032	–	–	0.474 ± 0.027	9.86	9.92 ± 0.03	–	–
262	16:34:01.8	+41:20:52.6	0.028	–	–	0.739 ± 0.030	10.37	10.32 ± 0.04	–	–
263	16:35:06.1	+41:10:38.5	0.079	–	–	0.462 ± 0.001	10.80	10.83 ± 0.03	–	–
264	16:35:41.7	+40:59:00.7	0.188	–	–	< 0.189	9.20	11.04 ± 0.03	–	–

Table A.1 continued from previous page

ID	R.A.	Decl.	z	$\log(L_{6.2})$	$\log(L_{7.7})$	$EW_{6.2}$	$\log(M_*)$	$\log(L_{\rm IR})$	$\log(M_{\rm d})$	$\log(M_{\rm H_2})$
	[hh:mm:ss]	[dd:mm:ss]		[$L_\odot$]	[$L_\odot$]	[μm]	[$M_\odot$]	[$L_\odot$]	[$M_\odot$]	[$M_\odot$]
265	16:35:46.9	+40:39:03.6	0.122	–	–	0.613 ± 0.007	10.39	11.09 ± 0.03	–	–
266	16:36:08.1	+41:05:07.7	0.170	–	–	0.457 ± 0.010	–	11.91 ± 0.10	–	–
267	16:36:45.3	+41:51:33.7	0.081	–	–	< 0.190	11.10	10.24 ± 0.06	–	–
268	16:36:51.7	+40:56:00.2	0.476	–	–	< 0.101	11.28	11.83 ± 0.02	–	–
269	16:37:05.3	+41:31:55.9	0.122	–	–	0.704 ± 0.001	10.64	11.20 ± 0.03	–	–
270	16:37:09.3	+41:40:30.9	0.760	–	–	< 0.032	–	12.41 ± 0.05	–	–
271	16:37:15.6	+41:49:33.7	0.121	–	–	0.580 ± 0.012	10.74	10.95 ± 0.03	–	–
272	16:37:29.3	+40:52:48.5	0.026	–	–	0.406 ± 0.020	–	10.10 ± 0.04	–	–
273	16:37:31.4	+40:51:55.6	0.189	< 8.78	–	0.404 ± 0.045	10.97	11.44 ± 0.05	–	10.15
274	16:37:51.2	+40:14:39.9	0.072	–	–	0.880 ± 0.043	10.33	10.63 ± 0.03	–	–
275	16:37:51.4	+41:30:27.3	0.286	< 9.46	–	0.131 ± 0.011	11.13	12.04 ± 0.04	–	11.16
276	16:37:51.9	+40:15:04.0	0.070	–	–	0.771 ± 0.021	10.30	10.61 ± 0.03	–	–
277	16:38:02.2	+40:46:53.4	0.103	–	–	0.204 ± 0.005	10.81	10.56 ± 0.06	–	–
278	16:38:05.9	+41:35:08.2	0.119	–	–	0.573 ± 0.134	10.69	11.02 ± 0.03	–	–
279	16:38:08.5	+40:32:13.8	0.220	–	–	0.486 ± 0.015	10.63	11.69 ± 0.05	–	–
280	16:38:09.6	+40:28:44.8	0.072	–	–	0.696 ± 0.067	10.12	10.55 ± 0.04	–	–
281	16:39:06.2	+40:40:03.3	0.035	–	–	0.719 ± 0.007	9.74	9.82 ± 0.03	–	–
282	16:40:19.7	+40:37:44.4	0.151	–	–	< 0.199	10.62	10.76 ± 0.08	–	–
284	16:40:43.7	+41:33:10.0	0.155	–	–	0.720 ± 0.006	10.95	11.14 ± 0.04	–	–
285	16:40:46.6	+41:25:22.6	0.096	–	–	0.098 ± 0.003	10.68	10.78 ± 0.05	–	–

Table A.1 continued from previous page

ID	R.A.	Decl.	z	$\log(L_{6.2})$	$\log(L_{7.7})$	$EW_{6.2}$	$\log(M_*)$	$\log(L_{\mathrm{IR}})$	$\log(M_{\mathrm{d}})$	$\log(M_{\mathrm{H_2}})$
	[hh:mm:ss]	[dd:mm:ss]		[$\mathrm{L_\odot}$]	[$\mathrm{L_\odot}$]	[µm]	[$\mathrm{M_\odot}$]	[$\mathrm{L_\odot}$]	[$\mathrm{M_\odot}$]	[$\mathrm{M_\odot}$]
286	16:41:01.4	+41:18:50.7	0.099	–	–	0.072 ± 0.013	10.64	10.67 ± 0.05	–	–
287	16:41:15.4	+41:03:20.7	0.138	–	–	0.519 ± 0.006	10.93	11.14 ± 0.02	–	–
288	16:41:35.3	+41:38:07.3	0.395	–	–	0.072 ± 0.003	10.15	11.58 ± 0.07	–	–
289	16:41:53.8	+40:58:42.6	0.327	–	–	0.119 ± 0.004	10.64	11.43 ± 0.03	–	–
290	16:42:11.9	+41:08:16.8	0.144	–	–	0.546 ± 0.013	10.37	11.36 ± 0.04	–	–
291	16:42:14.5	+40:51:29.0	0.104	–	–	< 0.058	10.70	10.62 ± 0.01	–	–
292	17:10:33.2	+58:44:56.7	0.281	9.29 ± 0.08	9.79 ± 0.03	0.325 ± 0.001	10.79	11.42 ± 0.01	8.22 ± 0.12	10.22
293	17:11:24.2	+59:31:21.5	1.489	10.17 ± 0.21	–	< 0.080	11.53	12.71 ± 0.01	8.27 ± 0.41	10.27
294	17:12:32.4	+59:21:26.2	0.210	9.17 ± 0.13	9.77 ± 0.04	0.507 ± 0.006	11.49	11.63 ± 0.01	8.55 ± 0.39	10.55
295	17:12:33.4	+58:36:10.3	1.663	9.98 ± 0.42	–	< 0.113	12.57	12.88 ± 0.01	8.45 ± 0.41	10.45
296	17:12:33.7	+59:40:26.8	0.217	9.37 ± 0.08	9.76 ± 0.05	0.983 ± 0.067	10.24	11.26 ± 0.01	7.68 ± 0.36	9.68
297	17:13:16.6	+58:32:34.9	0.079	8.62 ± 0.05	9.17 ± 0.04	0.780 ± 0.020	10.88	10.59 ± 0.01	7.98 ± 0.34	9.98
298	17:13:25.2	+59:05:31.2	0.126	8.07 ± 0.46	8.85 ± 0.20	< 0.189	10.34	10.33 ± 0.06	–	–
299	17:14:14.8	+58:52:21.6	0.167	9.14 ± 0.07	9.69 ± 0.03	0.780 ± 0.006	10.46	11.19 ± 0.01	7.56 ± 0.40	9.56
300	17:14:20.0	+60:27:24.8	2.990	11.17 ± 0.09	–	–	11.30	13.14 ± 0.02	8.70 ± 0.43	10.70
301	17:14:30.8	+58:42:25.4	0.562	9.20 ± 0.29	9.62 ± 0.17	< 0.075	11.31	12.01 ± 0.01	7.58 ± 0.42	9.58
302	17:14:46.4	+59:33:59.8	0.129	9.25 ± 0.03	9.80 ± 0.01	0.637 ± 0.002	11.16	11.11 ± 0.01	8.05 ± 0.34	10.05
303	17:14:47.3	+58:38:05.8	0.257	9.57 ± 0.05	10.09 ± 0.04	0.836 ± 0.012	–	11.57 ± 0.01	8.18 ± 0.30	10.18
304	17:15:13.8	+59:46:38.3	0.248	9.12 ± 0.09	9.61 ± 0.06	0.338 ± 0.091	11.08	11.28 ± 0.02	8.45 ± 0.28	10.45
305	17:15:44.0	+60:08:35.2	0.157	–	8.43 ± 0.17	< 0.190	10.95	10.68 ± 0.01	7.01 ± 0.17	9.01

Table A.1 continued from previous page

ID	R.A.	Decl.	z	$\log(L_{6.2})$	$\log(L_{7.7})$	$EW_{6.2}$	$\log(M_*)$	$\log(L_{\rm IR})$	$\log(M_{\rm d})$	$\log(M_{\rm H_2})$
	[hh:mm:ss]	[dd:mm:ss]		[$L_\odot$]	[$L_\odot$]	[μm]	[$M_\odot$]	[$L_\odot$]	[$M_\odot$]	[$M_\odot$]
306	17:15:50.5	+59:35:48.7	0.066	7.70 ± 0.24	8.24 ± 0.22	0.073 ± 0.005	11.01	10.25 ± 0.02	8.08 ± 0.29	10.08
307	17:16:14.5	+59:54:23.6	0.153	9.23 ± 0.04	9.77 ± 0.03	0.827 ± 0.009	10.80	11.25 ± 0.02	8.25 ± 0.39	10.25
308	17:16:30.2	+60:14:22.7	0.107	8.68 ± 0.08	9.17 ± 0.04	0.833 ± 0.133	9.69	10.62 ± 0.05	7.45 ± 0.25	9.45
309	17:16:50.6	+59:57:52.0	0.182	7.96 ± 1.20	8.74 ± 0.41	< 0.313	–	10.81 ± 0.01	8.04 ± 0.01	10.04
310	17:17:11.1	+60:27:10.0	0.110	8.78 ± 0.07	9.34 ± 0.06	0.488 ± 0.053	10.65	10.82 ± 0.01	7.74 ± 0.29	9.74
311	17:17:47.5	+59:32:58.1	0.248	8.68 ± 0.26	9.00 ± 0.28	< 0.093	–	10.84 ± 0.01	8.66 ± 0.01	10.66
312	17:17:54.6	+60:09:13.4	4.270	–	–	–	13.27	14.59 ± 0.13	–	–
313	17:18:52.7	+59:14:32.1	0.322	9.47 ± 0.10	10.32 ± 0.04	0.112 ± 0.010	10.64	11.90 ± 0.01	8.20 ± 0.19	10.20
314	17:19:13.5	+58:45:08.9	0.318	8.92 ± 0.26	9.55 ± 0.18	< 0.243	10.75	11.42 ± 0.12	–	–
315	17:19:33.3	+59:27:42.7	0.139	9.06 ± 0.06	9.71 ± 0.03	0.495 ± 0.005	10.96	11.22 ± 0.02	8.03 ± 0.42	10.03
316	17:19:44.9	+59:57:07.1	0.069	8.76 ± 0.02	9.28 ± 0.02	0.753 ± 0.005	10.55	10.73 ± 0.01	7.52 ± 0.36	9.52
317	17:20:43.3	+58:40:26.9	0.125	8.98 ± 0.05	9.58 ± 0.03	0.498 ± 0.006	10.91	11.11 ± 0.02	8.13 ± 0.39	10.13
318	17:20:44.9	+58:29:23.9	1.697	–	–	< 0.094	–	12.91 ± 0.01	8.56 ± 0.35	10.56
319	17:21:59.3	+59:50:34.2	0.028	7.73 ± 0.04	8.31 ± 0.05	0.387 ± 0.031	9.93	9.76 ± 0.01	7.07 ± 0.36	9.07
320	17:22:19.6	+59:45:07.0	0.272	8.37 ± 0.63	9.12 ± 0.13	< 0.133	10.75	11.22 ± 0.01	8.55 ± 0.01	10.55
321	17:22:28.2	+60:15:26.2	0.742	9.96 ± 0.11	10.60 ± 0.10	< 0.111	11.42	12.34 ± 0.01	8.91 ± 0.18	10.91
322	17:22:38.8	+58:51:07.0	1.624	–	9.89 ± 0.82	< 0.062	12.05	13.08 ± 0.01	9.16 ± 0.37	11.16
323	17:23:13.1	+59:05:33.1	0.108	8.84 ± 0.05	9.32 ± 0.03	0.750 ± 0.037	10.08	10.74 ± 0.02	7.52 ± 0.38	9.52
324	17:23:55.5	+60:13:01.1	0.175	9.22 ± 0.06	9.76 ± 0.03	0.905 ± 0.034	10.50	11.15 ± 0.01	8.28 ± 0.29	10.28
325	17:23:56.0	+59:40:47.4	0.030	7.33 ± 0.10	7.83 ± 0.14	0.518 ± 0.098	9.45	9.33 ± 0.01	6.24 ± 0.12	8.24

Table A.1 continued from previous page

ID	R.A.	Decl.	z	$\log(L_{6.2})$	$\log(L_{7.7})$	$EW_{6.2}$	$\log(M_*)$	$\log(L_{\rm IR})$	$\log(M_{\rm d})$	$\log(M_{\rm H_2})$
	[hh:mm:ss]	[dd:mm:ss]		[$L_\odot$]	[$L_\odot$]	[µm]	[$M_\odot$]	[$L_\odot$]	[$M_\odot$]	[$M_\odot$]
326	17:24:02.1	+60:06:01.2	0.156	8.92 ± 0.10	9.53 ± 0.06	0.461 ± 0.024	10.85	11.10 ± 0.01	7.97 ± 0.23	9.97
328	17:25:46.8	+59:36:55.3	0.035	8.35 ± 0.02	8.90 ± 0.02	0.554 ± 0.041	10.96	10.47 ± 0.02	7.79 ± 0.41	9.79
329	17:25:51.3	+60:11:38.9	0.029	8.14 ± 0.02	8.70 ± 0.02	0.454 ± 0.005	10.67	10.25 ± 0.01	7.23 ± 0.39	9.23
330	17:26:19.8	+60:16:00.0	0.924	9.88 ± 0.17	–	< 0.039	11.10	12.35 ± 0.08	–	–

Notes. This table contains the extended version of Table 2.3, enclosing all the information released as supplementary material. CO and PAH references for each data sample are listed in Section 2 of Cortzen et al. (2019). Column (1): Source name; column (2): Right ascension in units of hours, minutes, and seconds; column (3): Declination in units of degrees, arcminutes, and arcseconds; column (4): Redshift; column (5): PAH 6.2 µm luminosity; column (6): PAH 7.7 µm luminosity; column (7): Equivalent width of the PAH 6.2 µm feature; column (8): Stellar mass; column (9): Infrared luminosity (integrated from 8 – 1000 µm); column (10): Dust mass; column (11): Molecular gas mass derived using the $M_{\rm d}$–$\delta_{\rm GDR}$ method.

A.2 GALAXIES FROM THE LITERATURE WITH PAH, IR AND/OR CO.

Table A.2: Galaxies from the literature with PAH, IR and/or CO.

ID	R.A. [hh:mm:ss]	Decl. [dd:mm:ss]	Sample	z	$\log(L_{6.2})$ [$L_\odot$]	$\log(L_{7.7})$ [$L_\odot$]	$EW_{6.2}$ [µm]	$\log(M_*)$ [$M_\odot$]	$\log(L_{IR})$ [$L_\odot$]	Line	$\log(L'_{CO})$ [$L_\odot$]	$\log(M_d)$ [$M_\odot$]
NGC 4536	12:34:27.0	+02:11:16.5	SINGS	0.003	8.25 ± 0.20	–	–	–	10.34 ± 0.20	–	–	7.65 ± 0.31
NGC 3049	09:54:49.5	+09:16:18.1	SINGS	0.006	7.81 ± 0.20	–	–	–	9.65 ± 0.20	CO(3-2)	7.68 ± 0.21	7.37 ± 0.24
NGC 3351	10:43:57.7	+11:42:13.5	SINGS	0.002	7.49 ± 0.20	–	–	–	9.41 ± 0.20	CO(3-2)	8.01 ± 0.21	6.92 ± 0.37
NGC 4579	12:37:43.5	+11:49:03.8	SINGS	0.004	7.02 ± 0.20	–	–	–	9.05 ± 0.20	CO(3-2)	7.72 ± 0.21	6.88 ± 0.40
NGC 3773	11:38:12.9	+12:06:45.8	SINGS	0.003	6.71 ± 0.20	–	–	–	8.52 ± 0.20	CO(3-2)	6.77 ± 0.21	5.81 ± 0.32
NGC 3627	11:20:15.0	+12:59:29.0	SINGS	0.002	7.53 ± 0.20	–	–	–	9.29 ± 0.20	CO(3-2)	8.19 ± 0.21	6.70 ± 0.38
NGC 4569	12:36:49.7	+13:09:45.5	SINGS	0.004	7.52 ± 0.20	–	–	–	9.60 ± 0.20	CO(3-2)	8.54 ± 0.21	7.22 ± 0.39
NGC 4254	12:18:49.5	+14:24:57.5	SINGS	0.004	8.06 ± 0.20	–	–	–	9.69 ± 0.20	CO(3-2)	8.65 ± 0.21	7.14 ± 0.39
NGC 0628	01:36:41.6	+15:47:00.0	SINGS	0.002	7.01 ± 0.20	–	–	–	8.33 ± 0.20	CO(3-2)	6.94 ± 0.21	6.11 ± 0.36
NGC 4321	12:22:54.8	+15:49:19.2	SINGS	0.003	7.91 ± 0.20	–	–	–	9.65 ± 0.20	CO(3-2)	8.69 ± 0.21	7.27 ± 0.41
NGC 4826	12:56:43.5	+21:40:58.0	SINGS	0.001	7.10 ± 0.20	–	–	–	9.04 ± 0.20	CO(3-2)	8.26 ± 0.21	6.34 ± 0.37
NGC 3190	10:18:05.6	+21:49:54.2	SINGS	0.005	7.33 ± 0.20	–	–	–	9.54 ± 0.20	CO(3-2)	7.74 ± 0.21	7.16 ± 0.33
NGC 4725	12:50:26.5	+25:30:01.2	SINGS	0.003	6.22 ± 0.20	–	–	–	8.35 ± 0.20	CO(3-2)	6.30 ± 0.21	6.56 ± 0.38
NGC 0855	02:14:03.7	+27:52:38.4	SINGS	0.002	6.15 ± 0.20	–	–	–	8.59 ± 0.20	CO(3-2)	7.18 ± 0.21	5.94 ± 0.36
NGC 4559	12:35:57.5	+27:57:34.2	SINGS	0.002	7.40 ± 0.20	–	–	–	8.96 ± 0.20	CO(3-2)	7.14 ± 0.21	6.72 ± 0.36
NGC 3265	10:31:06.8	+28:47:45.6	SINGS	0.005	7.68 ± 0.20	–	–	–	9.48 ± 0.20	CO(3-2)	8.11 ± 0.21	6.53 ± 0.29
NGC 4631	12:42:07.8	+32:32:34.6	SINGS	0.002	7.99 ± 0.20	–	–	–	9.57 ± 0.20	CO(3-2)	7.99 ± 0.21	6.94 ± 0.35
NGC 0925	02:27:17.2	+33:34:41.6	SINGS	0.002	6.67 ± 0.20	–	–	–	8.33 ± 0.20	CO(3-2)	6.40 ± 0.21	6.34 ± 0.36
NGC 7331	22:37:04.1	+34:24:55.3	SINGS	0.003	8.09 ± 0.20	–	–	–	9.33 ± 0.20	–	–	6.95 ± 0.38
NGC 4736	12:50:53.1	+41:07:14.4	SINGS	0.001	7.42 ± 0.20	–	–	–	9.09 ± 0.20	CO(3-2)	7.72 ± 0.21	6.29 ± 0.35
NGC 4625	12:41:52.6	+41:16:26.9	SINGS	0.002	6.66 ± 0.20	–	–	–	8.23 ± 0.20	CO(3-2)	6.42 ± 0.21	6.11 ± 0.33
NGC 3184	10:18:16.9	+41:25:24.7	SINGS	0.003	6.65 ± 0.20	–	–	–	8.32 ± 0.20	CO(3-2)	7.20 ± 0.21	6.17 ± 0.39
NGC 2798	09:17:22.8	+41:59:59.4	SINGS	0.006	8.56 ± 0.20	–	–	–	10.48 ± 0.20	–	–	7.17 ± 0.34
NGC 5055	13:15:49.3	+42:01:45.7	SINGS	0.002	7.33 ± 0.20	–	–	–	9.07 ± 0.20	CO(3-2)	7.94 ± 0.21	6.90 ± 0.40
NGC 3938	11:52:49.3	+44:07:13.6	SINGS	0.003	7.35 ± 0.20	–	–	–	9.01 ± 0.20	CO(3-2)	7.84 ± 0.21	6.66 ± 0.37
NGC 3198	10:19:54.8	+45:32:58.7	SINGS	0.003	7.11 ± 0.20	–	–	–	9.10 ± 0.20	CO(3-2)	7.81 ± 0.21	7.02 ± 0.32
NGC 5866	15:06:29.4	+55:45:45.0	SINGS	0.004	6.83 ± 0.20	–	–	–	9.31 ± 0.20	–	–	6.74 ± 0.37
NGC 6946	20:34:52.2	+60:09:14.4	SINGS	0.002	8.07 ± 0.20	–	–	–	9.54 ± 0.20	–	–	6.99 ± 0.39

Table A.2 continued from previous page

ID	R.A. [hh:mm:ss]	Decl. [dd:mm:ss]	Sample	z	$\log(L_{6.2})$ [$L_\odot$]	$\log(L_{7.7})$ [$L_\odot$]	$EW_{6.2}$ [μm]	$\log(M_*)$ [$M_\odot$]	$\log(L_{IR})$ [$L_\odot$]	Line	$\log(L'_{CO})$ [$L_\odot$]	$\log(M_d)$ [$M_\odot$]
NGC 2976	09:47:15.2	+67:55:00.3	SINGS	0.001	6.08 ± 0.20	–	–	–	7.80 ± 0.20	CO(3-2)	6.35 ± 0.21	5.44 ± 0.34
NGC 3521	11:05:48.5	-00:02:07.3	SINGS	0.002	7.66 ± 0.20	–	–	–	9.39 ± 0.20	CO(3-2)	8.00 ± 0.21	7.02 ± 0.37
NGC 5713	14:40:11.3	-00:17:24.2	SINGS	0.007	8.90 ± 0.20	–	–	–	10.50 ± 0.20	–	–	7.57 ± 0.36
NGC 1266	03:16:00.7	-02:25:36.9	SINGS	0.007	7.64 ± 0.20	–	–	–	10.28 ± 0.20	–	–	6.89 ± 0.34
NGC 0337	00:59:50.2	-07:34:45.8	SINGS	0.005	8.06 ± 0.20	–	–	–	9.91 ± 0.20	CO(3-2)	8.06 ± 0.21	7.19 ± 0.34
NGC 4594	12:39:59.5	-11:37:23.2	SINGS	0.002	6.55 ± 0.20	–	–	–	8.51 ± 0.20	CO(3-2)	6.59 ± 0.21	6.54 ± 0.39
NGC 1482	03:54:38.8	-20:30:07.1	SINGS	0.005	8.80 ± 0.20	–	–	–	10.60 ± 0.20	–	–	7.45 ± 0.35
NGC 1097	02:46:18.8	-30:16:27.2	SINGS	0.004	8.59 ± 0.20	–	–	–	10.46 ± 0.20	–	–	7.82 ± 0.36
NGC 7793	23:57:49.8	-32:35:27.1	SINGS	0.001	6.31 ± 0.20	–	–	–	7.87 ± 0.20	–	–	5.68 ± 0.37
NGC 3621	11:18:16.5	-32:48:49.3	SINGS	0.002	7.31 ± 0.20	–	–	–	8.71 ± 0.20	–	–	6.38 ± 0.39
NGC 1316	03:22:41.6	-37:12:29.4	SINGS	0.006	6.86 ± 0.20	–	–	–	9.43 ± 0.20	–	–	6.78 ± 0.33
NGC 1291	03:17:18.5	-41:06:28.0	SINGS	0.003	6.52 ± 0.20	–	–	–	8.48 ± 0.20	–	–	6.54 ± 0.35
NGC 1512	04:03:54.1	-43:20:54.4	SINGS	0.003	6.94 ± 0.20	–	–	–	9.06 ± 0.20	–	–	7.23 ± 0.18
NGC 2915	09:26:10.0	-76:37:32.2	SINGS	0.001	5.43 ± 0.20	–	–	–	7.31 ± 0.20	–	–	4.84 ± 0.27
IRAS 10565+2448	10:59:18.1	+24:32:34	ULIRG	0.043	9.57 ± 0.01	10.13 ± 0.01	–	–	12.04 ± 0.02	CO(1-0)	9.72 ± 0.05	8.40 ± 0.20
IRAS 16334+4630	16:33:24.3	+46:30:58	ULIRG	0.191	9.79 ± 0.03	10.40 ± 0.02	–	–	12.34 ± 0.02	CO(1-0)	10.07 ± 0.16	10.50 ± 0.20
IRAS 17208-0014	17:23:21.9	+00:17:01	ULIRG	0.043	9.62 ± 0.01	10.28 ± 0.01	–	–	11.99 ± 0.02	CO(1-0)	10.01 ± 0.05	8.76 ± 0.20
IRAS 19297-0406	19:32:21.2	+03:59:56	ULIRG	0.085	9.60 ± 0.02	10.25 ± 0.01	–	–	12.42 ± 0.02	CO(1-0)	9.87 ± 0.09	9.07 ± 0.20
IRAS 19458+0944	19:45:52.0	+09:44:30	ULIRG	0.100	9.71 ± 0.01	10.30 ± 0.01	–	–	12.40 ± 0.02	CO(1-0)	10.12 ± 0.10	9.12 ± 0.20
IRAS 20414-1651	20:44:18.2	+16:40:16	ULIRG	0.086	9.42 ± 0.02	10.05 ± 0.01	–	–	12.23 ± 0.02	CO(1-0)	9.57 ± 0.16	10.11 ± 0.20
Arp 220	15:34:57.2	+23:30:11	ULIRG	0.018	8.99 ± 2.44	–	–	–	12.15 ± 0.02	CO(1-0)	9.85 ± 0.09	8.60 ± 0.20
IRAS 05189-2524	05:21:01.4	-25:21:46	ULIRG	0.042	9.05 ± 0.03	9.85 ± 0.02	–	–	12.15 ± 0.02	CO(1-0)	< 9.88	8.61 ± 0.20
IRAS 12112+0305	12:13:46.0	+02:48:38	ULIRG	0.073	9.45 ± 0.02	10.12 ± 0.01	–	–	12.32 ± 0.02	CO(1-0)	10.13 ± 0.06	8.71 ± 0.20
IRAS 14348-1447	14:37:38.3	+15:00:22	ULIRG	0.083	9.44 ± 0.02	10.23 ± 0.01	–	–	12.34 ± 0.02	CO(1-0)	< 10.11	–
IRAS 22491-1808	22:51:49.0	-17:52:23	ULIRG	0.077	9.15 ± 0.04	9.91 ± 0.01	–	–	12.18 ± 0.02	CO(1-0)	< 9.78	8.47 ± 0.20
Mrk 273	13:44:42.1	+55:53:13	ULIRG	0.038	9.40 ± 0.01	10.16 ± 0.01	–	–	12.15 ± 0.02	CO(1-0)	9.83 ± 0.04	8.46 ± 0.20
UGC 5101	09:35:51.6	+61:21:11	ULIRG	0.039	9.20 ± 0.02	10.0 ± 0.01	–	–	12.00 ± 0.02	CO(1-0)	9.71 ± 0.04	8.42 ± 0.20
GN70.104	12:37:02.7	+62:14:01.5	HzSFG	1.246	10.23 ± 0.07	10.86 ± 0.06	–	11.28	12.08 ± 0.18	CO(2-1)	10.25 ± 0.03	–
GN70.14	12:36:45.8	+62:07:54.2	HzSFG	1.432	10.07 ± 0.25	10.90 ± 0.16	–	11.33	12.42 ± 0.17	CO(2-1)	10.31 ± 0.13	–

Table A.2 continued from previous page

ID	R.A. [hh:mm:ss]	Decl. [dd:mm:ss]	Sample	z	$\log(L_{6.2})$ [$L_\odot$]	$\log(L_{7.7})$ [$L_\odot$]	$EW_{6.2}$ [μm]	$\log(M_*)$ [$M_\odot$]	$\log(L_{IR})$ [$L_\odot$]	Line	$\log(L'_{CO})$ [$L_\odot$]	$\log(M_d)$ [$M_\odot$]
GN70.38	12:36:33.7	+62:10:05.9	HzSFG	1.016	9.98 ± 0.08	10.68 ± 0.10	–	11.41	11.86 ± 0.18	CO(2-1)	10.19 ± 0.10	–
GN70.8	12:36:20.9	+62:07:14.2	HzSFG	1.148	10.37 ± 0.15	11.18 ± 0.07	–	11.59	12.20 ± 0.16	CO(2-1)	10.08 ± 0.09	–
GN70.211	12:37:10.6	+62:22:34.5	HzSFG	1.523	10.39 ± 0.10	10.84 ± 0.11	–	10.89	12.30 ± 0.17	CO(1-0)	10.20 ± 0.12	–
BzK4171	12:36:26.5	+62:08:35.3	HzSFG	1.465	9.84 ± 0.33	10.63 ± 0.40	–	10.60	11.94 ± 0.18	CO(1-0)	10.36 ± 0.12	8.70 ± 0.20
GN06	12:36:18.3	+62:15:50.4	SMG	2.000	10.26 ± 0.04	–	0.83 ± 0.10	–	12.65 ± 0.17	CO(4-3)	10.67 ± 0.10	–
GN19	12:37:07.2	+62:14:08.0	SMG	2.490	10.23 ± 0.06	–	0.59 ± 0.20	–	12.56 ± 0.17	CO(1-0)	10.80 ± 0.07	–
GN20	12:37:11.9	+62:22:11.9	SMG	4.055	10.43 ± 0.07	–	–	–	13.08 ± 0.18	CO(1-0)	11.15 ± 0.10	9.67 ± 0.20
GN39a	12:37:11.4	+62:13:31.1	SMG	1.996	10.49 ± 0.09	11.02 ± 0.03	0.66 ± 0.26	–	12.82 ± 0.17	CO(3-2)	10.91 ± 0.04	–
GN39b	12:37:12.0	+62:13:25.8	SMG	1.992	10.48 ± 0.10	11.02 ± 0.03	1.09 ± 0.65	–	12.30 ± 0.17	CO(3-2)	10.72 ± 0.15	–
GN26	12:36:34.5	+62:12:40.9	SMG	1.223	10.55 ± 0.02	11.06 ± 0.02	0.38 ± 0.04	11.32	12.66 ± 0.17	CO(2-1)	10.92 ± 0.12	–
MIPS 15949	17:21:09.2	+60:15:01.3	HzSB	2.119	–	10.71 ± 0.08	< 0.14	–	12.90 ± 0.18	CO(3-2)	10.71 ± 0.06	–
MIPS 16059	17:24:28.4	+60:15:33.2	HzSB	2.326	–	10.76 ± 0.09	< 0.14	–	12.87 ± 0.15	CO(3-2)	10.52 ± 0.09	–
MIPS 16080	17:18:44.8	+60:01:15.9	HzSB	2.006	–	10.20 ± 0.17	< 0.14	–	12.71 ± 0.15	CO(3-2)	10.57 ± 0.08	–
MIPS 16144	17:24:22.1	+59:31:50.8	HzSB	2.128	–	11.20 ± 0.06	< 0.32	–	12.72 ± 0.12	CO(3-2)	10.83 ± 0.09	–
MIPS 429	17:16:11.8	+59:12:13.3	HzSB	2.201	–	10.63 ± 0.09	< 0.30	–	12.72 ± 0.15	CO(3-2)	10.66 ± 0.08	–
MIPS 506	17:11:38.6	+58:38:36.7	HzSB	2.470	–	11.11 ± 0.13	0.30 ± 0.14	–	12.93 ± 0.09	CO(3-2)	10.52 ± 0.10	–
MIPS 8196	17:15:10.3	+60:09:55.2	HzSB	–	–	11.09 ± 0.08	< 0.06	–	12.99 ± 0.15	CO(3-2)	< 10.52	–
MIPS 8327	17:15:35.8	+60:28:25.5	HzSB	2.442	–	10.62 ± 0.21	< 0.14	–	12.83 ± 0.21	CO(3-2)	10.41 ± 0.08	–
MIPS 8342	17:14:11.5	+60:11:09.3	HzSB	1.562	–	10.52 ± 0.10	< 0.16	–	12.55 ± 0.30	CO(2-1)	10.39 ± 0.05	–

Notes. This table contains the extended version of Table 2.4, enclosing all the information released as supplementary material. CO and PAH references for each data sample are listed in Section 2 of Cortzen et al. (2019). Column (1): Source name; column (2): Right ascension in units of hours, minutes, and seconds; column (3): Declination in units of degrees, arcminutes, and arcseconds; column (4): Galaxy sample or selection; column (5): Redshift; column (6): PAH 6.2 μm luminosity; column (7): PAH 7.7 μm luminosity; (8): Equivalent width of the PAH 6.2 μm feature; column (9): Stellar mass; (10): Infrared luminosity (integrated from 8 – 1000 μm); column (11): Observed CO line; column (12): CO(1 – 0) luminosity; (13): Dust mass.

Bibliography

Akimkin, V. V., Kirsanova, M. S., Pavlyuchenkov, Y. N., & Wiebe, D. S., 2015, MNRAS 449, 440

— 2017, MNRAS 469, 630

Alaghband-Zadeh, S., Chapman, S. C., Swinbank, A. M., et al., 2013, MNRAS 435, 1493

Albrecht, A. & Steinhardt, P. J., 1982, Phys. Rev. Lett. 48, 1220

Allain, T., Leach, S., & Sedlmayr, E., 1996, A&A 305, 602

Allamandola, L. J., Tielens, A. G. G. M., & Barker, J. R., 1989, ApJS 71, 733

Allen, R. J., Ivette Rodrıguez, M., Black, J. H., & Booth, R. S., 2012, AJ 143, 97

Alonso-Herrero, A., Esquej, P., Roche, P. F., et al., 2016, MNRAS 455, 563

Alonso-Herrero, A., Ramos Almeida, C., Esquej, P., et al., 2014, MNRAS 443, 2766

Alpher, R. A., Bethe, H., & Gamow, G., 1948, Physical Review 73, 803

Alpher, R. A. & Herman, R. C., 1949, Physical Review 75, 1089

Aravena, M., Carilli, C., Daddi, E., et al., 2010, ApJ 718, 177

Armus, L., Charmandaris, V., Bernard-Salas, J., et al., 2007, ApJ 656, 148

Bakes, E. L. O. & Tielens, A. G. G. M., 1994, ApJ 427, 822

Barišić, I., van der Wel, A., Bezanson, R., et al., 2017, ApJ 847, 72

Baum, W. A., 1959, PASP 71, 106

Bell, E. F., 2003, ApJ 586, 794

Bell, E. F., Wolf, C., Meisenheimer, K., et al., 2004, ApJ 608, 752

Bendo, G. J., Draine, B. T., Engelbracht, C. W., et al., 2008, MNRAS 389, 629

Bendo, G. J., Wilson, C. D., Warren, B. E., et al., 2010, MNRAS 402, 1409

Benford, D. J., Cox, P., Omont, A., Phillips, T. G., & McMahon, R. G., 1999, ApJ 518, L65

Berta, S., Lutz, D., Genzel, R., Förster-Schreiber, N. M., & Tacconi, L. J., 2016, A&A 587, A73
Bertemes, C., Wuyts, S., Lutz, D., et al., 2018, MNRAS 478, 1442
Best, P. N., Kauffmann, G., Heckman, T. M., et al., 2005, MNRAS 362, 25
Best, P. N., Ker, L. M., Simpson, C., Rigby, E. E., & Sabater, J., 2014, MNRAS 445, 955
Béthermin, M., Daddi, E., Magdis, G., et al., 2015, A&A 573, A113
Bisbas, T. G., Papadopoulos, P. P., & Viti, S., 2015, ApJ 803, 37
Bisbas, T. G., van Dishoeck, E. F., Papadopoulos, P. P., et al., 2017, ApJ 839, 90
Blain, A. W., Barnard, V. E., & Chapman, S. C., 2003, MNRAS 338, 733
Blanton, M. R. & Moustakas, J., 2009, ARA&A 47, 159
Blitz, L. & Rosolowsky, E., 2006, ApJ 650, 933
Bolatto, A. D., Wolfire, M., & Leroy, A. K., 2013, ARA&A 51, 207
Bothwell, M. S., Aguirre, J. E., Aravena, M., et al., 2017, MNRAS 466, 2825
Bothwell, M. S., Smail, I., Chapman, S. C., et al., 2013, MNRAS 429, 3047
Bouché, N., Cresci, G., Davies, R., et al., 2007, ApJ 671, 303
Bouché, N., Dekel, A., Genzel, R., et al., 2010, ApJ 718, 1001
Boulanger, F., Beichman, C., Desert, F. X., et al., 1988, ApJ 332, 328
Boulanger, F., Falgarone, E., Puget, J. L., & Helou, G., 1990, ApJ 364, 136
Brammer, G. B., van Dokkum, P. G., & Coppi, P., 2008, ApJ 686, 1503
Brammer, G. B., Whitaker, K. E., van Dokkum, P. G., et al., 2011, ApJ 739, 24
Brandl, B. R., Bernard-Salas, J., Spoon, H. W. W., et al., 2006, ApJ 653, 1129
Brinchmann, J., Charlot, S., White, S. D. M., et al., 2004, MNRAS 351, 1151
Bruzual, G. & Charlot, S., 2003, MNRAS 344, 1000
Calzetti, D., Kennicutt Jr., R. C., Bianchi, L., et al., 2005, ApJ 633, 871
Calzetti, D., Kennicutt, R. C., Engelbracht, C. W., et al., 2007, ApJ 666, 870
Cameron, A. G., 1955, The Astrophysical Journal 121, 144
Cañameras, R., Yang, C., Nesvadba, N. P. H., et al., 2018, A&A 620, A61
Capak, P. L., Carilli, C., Jones, G., et al., 2015, Nature 522, 455
Carilli, C. L., Daddi, E., Riechers, D., et al., 2010, ApJ 714, 1407
Carilli, C. L., Hodge, J., Walter, F., et al., 2011, ApJ 739, L33
Carilli, C. L. & Walter, F., 2013, ARA&A 51, 105
Casey, C. M., Chapman, S. C., Daddi, E., et al., 2009, MNRAS 400, 670
Casey, C. M., Chapman, S. C., Neri, R., et al., 2011, MNRAS 415, 2723

Casey, C. M., Narayanan, D., & Cooray, A., 2014, Phys. Rep. 541, 45
Castellanos, P., Candian, A., Andrews, H., & Tielens, A. G. G. M., 2018a, A&A 616, A167
Castellanos, P., Candian, A., Zhen, J., Linnartz, H., & Tielens, A. G. G. M., 2018b, A&A 616, A166
Cavagnolo, K. W., McNamara, B. R., Nulsen, P. E. J., et al., 2010, ApJ 720, 1066
Ceraj, L., Smolčić, V., Delvecchio, I., et al., 2018, A&A 620, A192
Chabrier, G., 2003, PASP 115, 763
Cherchneff, I., Barker, J. R., & Tielens, A. G. G. M., 1992, ApJ 401, 269
Chung, A., Narayanan, G., Yun, M. S., Heyer, M., & Erickson, N. R., 2009, AJ 138, 858
Churchwell, E., Povich, M. S., Allen, D., et al., 2006, ApJ 649, 759
Cibinel, A., Daddi, E., Sargent, M. T., et al., 2019, MNRAS 485, 5631
Combes, F., 2018, A&A Rev. 26, 5
Conley, A., Cooray, A., Vieira, J. D., et al., 2011, ApJ 732, L35
Cortzen, I., Garrett, J., Magdis, G., et al., 2019, MNRAS 482, 1618
Cortzen, I., Magdis, G. E., Valentino, F., et al., 2020, A&A 634, L14
Cox, P., Krips, M., Neri, R., et al., 2011, ApJ 740, 63
da Cunha, E., Groves, B., Walter, F., et al., 2013, ApJ 766, 13
Daddi, E., Bournaud, F., Walter, F., et al., 2010a, ApJ 713, 686
Daddi, E., Dannerbauer, H., Elbaz, D., et al., 2008, ApJ 673, L21
Daddi, E., Dannerbauer, H., Liu, D., et al., 2015, A&A 577, A46
Daddi, E., Dannerbauer, H., Stern, D., et al., 2009, ApJ 694, 1517
Daddi, E., Dickinson, M., Morrison, G., et al., 2007, ApJ 670, 156
Daddi, E., Elbaz, D., Walter, F., et al., 2010b, ApJ 714, L118
Dale, D. A., Aniano, G., Engelbracht, C. W., et al., 2012, ApJ 745, 95
Dale, D. A., Smith, J. D. T., Schlawin, E. A., et al., 2009, ApJ 693, 1821
Dale, D. A. & Helou, G., 2002, ApJ 576, 159
de Vaucouleurs, G., 1961, ApJS 5, 233
Decarli, R., Walter, F., Aravena, M., et al., 2016, ApJ 833, 70
Decarli, R., Walter, F., Gónzalez-López, J., et al., 2019, ApJ 882, 138
Desai, V., Armus, L., Spoon, H. W. W., et al., 2007, ApJ 669, 810
Desert, F. .-.-X., Boulanger, F., & Puget, J. L., 1990, A&A 500, 313
Diamond-Stanic, A. M. & Rieke, G. H., 2010, ApJ 724, 140
Díaz-Santos, T., Charmandaris, V., Armus, L., et al., 2011, ApJ 741, 32

Dicke, R. H., Peebles, P. J. E., Roll, P. G., & Wilkinson, D. T., 1965, ApJ 142, 414

Dickinson, M. & FIDEL Team, 2007, *American Astronomical Society Meeting Abstracts*, vol. 39, Bulletin of the American Astronomical Society, 822

Djorgovski, S. & Davis, M., 1987, ApJ 313, 59

Downes, D. & Solomon, P. M., 1998, ApJ 507, 615

Draine, B. T. & Li, A., 2007, ApJ 657, 810

Dressler, A., Lynden-Bell, D., Burstein, D., et al., 1987, ApJ 313, 42

Eales, S., Smith, M. W. L., Auld, R., et al., 2012, ApJ 761, 168

Einstein, A., 1916, Annalen der Physik 354, 769

Elbaz, D., Daddi, E., Le Borgne, D., et al., 2007, A&A 468, 33

Elbaz, D., Dickinson, M., Hwang, H. S., et al., 2011, A&A 533, A119

Engelbracht, C. W., Gordon, K. D., Rieke, G. H., et al., 2005, ApJ 628, L29

Engelbracht, C. W., Rieke, G. H., Gordon, K. D., et al., 2008, ApJ 678, 804

Esquej, P., Alonso-Herrero, A., González-Martın, O., et al., 2014, ApJ 780, 86

Fabian, A. C., 2012, ARA&A 50, 455

Fadda, D., Yan, L., Lagache, G., et al., 2010, ApJ 719, 425

Fadda, D., Marleau, F. R., Storrie-Lombardi, L. J., et al., 2006, AJ 131, 2859

Farrah, D., Afonso, J., Efstathiou, A., et al., 2003, MNRAS 343, 585

Farrah, D., Lonsdale, C. J., Weedman, D. W., et al., 2008, ApJ 677, 957

Fazio, G. G., Hora, J. L., Allen, L. E., et al., 2004, ApJS 154, 10

Frayer, D. T., Koda, J., Pope, A., et al., 2008, ApJ 680, L21

Friedmann, A., 1922, Zeitschrift fur Physik 10, 377

Förster Schreiber, N. M., Roussel, H., Sauvage, M., & Charmandaris, V., 2004, A&A 419, 501

Gamow, G., 1946, Physical Review 70, 572

Gao, Y. & Solomon, P. M., 2004, ApJ 606, 271

Garnavich, P. M., Kirshner, R. P., Challis, P., et al., 1998, ApJ 493, L53

Geach, J. E., Smail, I., Moran, S. M., et al., 2011, ApJ 730, L19

Genzel, R., Lutz, D., Sturm, E., et al., 1998, ApJ 498, 579

Genzel, R., Tacconi, L. J., Combes, F., et al., 2012, ApJ 746, 69

Genzel, R., Tacconi, L. J., Gracia-Carpio, J., et al., 2010, MNRAS 407, 2091

Genzel, R., Tacconi, L. J., Lutz, D., et al., 2015, ApJ 800, 20

Glazebrook, K., Schreiber, C., Labbé, I., et al., 2017, Nature 544, 71

Glover, S. C. O., Clark, P. C., Micic, M., & Molina, F., 2015, MNRAS 448, 1607
Glover, S. C. O. & Smith, R. J., 2016, MNRAS 462, 3011
Griffin, M. J., Abergel, A., Abreu, A., et al., 2010, A&A 518, L3
Guth, A. H., 1981, Phys. Rev. D 23, 347
Helou, G., Roussel, H., Appleton, P., et al., 2004, ApJS 154, 253
Helou, G., Ryter, C., & Soifer, B. T., 1991, ApJ 376, 505
Helou, G., Malhotra, S., Hollenbach, D., Dale, D., & Contursi, A., 2001, ApJl 548, L73
Herbst, E., 1991, ApJ 366, 133
Hodge, J. A., Carilli, C. L., Walter, F., et al., 2012, ApJ 760, 11
Hodge, J. A., Riechers, D., Decarli, R., et al., 2015, ApJ 798, L18
Hodge, J. A., Swinbank, A. M., Simpson, J. M., et al., 2016, ApJ 833, 103
Holland, W. S., Robson, E. I., Gear, W. K., et al., 1999, MNRAS 303, 659
Hollenbach, D. & Salpeter, E. E., 1971, ApJ 163, 155
Houck, J. R., Roellig, T. L., van Cleve, J., et al., 2004, ApJS 154, 18
Houck, J. R., Soifer, B. T., Weedman, D., et al., 2005, ApJ 622, L105
Houck, J. R., Weedman, D. W., Le Floc'h, E., & Hao, L., 2007, ApJ 671, 323
Hoyle, F., 1946, MNRAS 106, 343
— 1954, ApJS 1, 121
Huang, J. .-.-S., Faber, S. M., Daddi, E., et al., 2009, ApJ 700, 183
Huang, J. .-.-S., Rigopoulou, D., Magdis, G., et al., 2014, ApJ 784, 52
Huang, M.-L. & Kauffmann, G., 2014, MNRAS 443, 1329
Hubble, E., 1929, Proceedings of the National Academy of Science 15, 168
Hubble, E. & Humason, M. L., 1931, ApJ 74, 43
Hughes, T. M., Ibar, E., Villanueva, V., et al., 2017, MNRAS 468, L103
Hunt, L. K., Thuan, T. X., Izotov, Y. I., & Sauvage, M., 2010, ApJ 712, 164
Hönig, S. F., Kishimoto, M., Gandhi, P., et al., 2010, A&A 515, A23
Haas, M., Klaas, U., & Bianchi, S., 2002, A&A 385, L23
Ikeda, M., Oka, T., Tatematsu, K., Sekimoto, Y., & Yamamoto, S., 2002, ApJS 139, 467
Israel, F. P., 1997, A&A 317, 65
Israel, F. P., Rosenberg, M. J. F., & van der Werf, P., 2015, A&A 578, A95
Ivison, R. J., Papadopoulos, P. P., Smail, I., et al., 2011, MNRAS 412, 1913
Jeans, J. H., 1902, Philosophical Transactions of the Royal Society of London Series A 199, 1

Jensen, J. J., Hönig, S. F., Rakshit, S., et al., 2017, MNRAS 470, 3071
Jiao, Q., Zhao, Y., Lu, N., et al., 2019a, ApJ 883, 207
— 2019b, ApJ 880, 133
Jin, S., Daddi, E., Magdis, G. E., et al., 2019, ApJ 887, 144
Jin, S., Daddi, E., Liu, D., et al., 2018, ApJ 864, 56
Jones, A. G., Bendo, G. J., Baes, M., et al., 2015, MNRAS 448, 168
Kamenetzky, J., Rangwala, N., Glenn, J., Maloney, P. R., & Conley, A., 2016, ApJ 829, 93
Kauffmann, G., Heckman, T. M., White, S. D. M., et al., 2003, MNRAS 341, 33
Kelly, B. C., 2007, ApJ 665, 1489
Kennicutt Robert C., J., 1998, ARA&A 36, 189
Kennicutt Jr., R. C., Armus, L., Bendo, G., et al., 2003, PASP 115, 928
Kessler, M. F., Steinz, J. A., Anderegg, M. E., et al., 1996, A&A 500, 493
Kewley, L. J. & Dopita, M. A., 2002, ApJS 142, 35
Kim, D.-C., Veilleux, S., & Sanders, D. B., 1998, ApJ 508, 627
Kirkpatrick, A., Alberts, S., Pope, A., et al., 2017, ApJ 849, 111
Kirkpatrick, A., Pope, A., Aretxaga, I., et al., 2014, ApJ 796, 135
Kriek, M., van Dokkum, P. G., Labbé, I., et al., 2009, ApJ 700, 221
Krumholz, M. R., Dekel, A., & McKee, C. F., 2012, ApJ 745, 69
Krumholz, M. R., Leroy, A. K., & McKee, C. F., 2011, ApJ 731, 25
Kuno, N., Sato, N., Nakanishi, H., et al., 2007, PASJ 59, 117
Kaasinen, M., Scoville, N., Walter, F., et al., 2019, ApJ 880, 15
Lagos, C. D. P., Baugh, C. M., Lacey, C. G., et al., 2011, MNRAS 418, 1649
Lagos, C. d. P., Bayet, E., Baugh, C. M., et al., 2012, MNRAS 426, 2142
Langer, W. D., Velusamy, T., Pineda, J. L., Willacy, K., & Goldsmith, P. F., 2014, A&A 561, A122
Latter, W. B., 1991, ApJ 377, 187
Laurent, O., Mirabel, I. F., Charmandaris, V., et al., 2000, A&A 359, 887
Le Floc'h, E., Papovich, C., Dole, H., et al., 2005, ApJ 632, 169
Le Page, V., Snow, T. P., & Bierbaum, V. M., 2003, ApJ 584, 316
Lebouteiller, V., Brandl, B., Bernard-Salas, J., Devost, D., & Houck, J. R., 2007, ApJ 665, 390
Lemaître, G., 1927, Annales de la Société Scientifique de Bruxelles 47, 49
Leroy, A. K., Bolatto, A., Gordon, K., et al., 2011, ApJ 737, 12
Leroy, A. K., Walter, F., Brinks, E., et al., 2008, AJ 136, 2782

Li, A. & Draine, B. T., 2001, ApJ 554, 778
Liang, L., Feldmann, R., Faucher-Giguère, C.-A., et al., 2018, MNRAS 478, L83
Linde, A. D., 1982, Physics Letters B 108, 389
Liu, D., Gao, Y., Isaak, K., et al., 2015, ApJ 810, L14
Liu, D., Schinnerer, E., Groves, B., et al., 2019, ApJ 887, 235
Lonsdale, C. J., Smith, H. E., Rowan-Robinson, M., et al., 2003, PASP 115, 897
Lutz, D., Berta, S., Contursi, A., et al., 2016, A&A 591, A136
Lutz, D., Kunze, D., Spoon, H. W. W., & Thornley, M. D., 1998, A&A 333, L75
Lutz, D., Sturm, E., Tacconi, L. J., et al., 2007, ApJ 661, L25
Lutz, D., 2014, ARA&A 52, 373
Madau, P. & Dickinson, M., 2014, ARA&A 52, 415
Madden, S. C., Galliano, F., Jones, A. P., & Sauvage, M., 2006, A&A 446, 877
Magdis, G. E., Daddi, E., Sargent, M., et al., 2012a, ApJ 758, L9
Magdis, G. E., Rigopoulou, D., Daddi, E., et al., 2017, A&A 603, A93
Magdis, G. E., Rigopoulou, D., Helou, G., et al., 2013, A&A 558, A136
Magdis, G. E., Rigopoulou, D., Huang, J. .-.-S., & Fazio, G. G., 2010, MNRAS 401, 1521
Magdis, G. E., Bureau, M., Stott, J. P., et al., 2016, MNRAS 456, 4533
Magdis, G. E., Daddi, E., Béthermin, M., et al., 2012b, ApJ 760, 6
Magdis, G. E., Daddi, E., Elbaz, D., et al., 2011, ApJ 740, L15
Magdis, G. E., Rigopoulou, D., Hopwood, R., et al., 2014, ApJ 796, 63
Magnelli, B., Lutz, D., Saintonge, A., et al., 2014, A&A 561, A86
Magnelli, B., Lutz, D., Santini, P., et al., 2012a, A&A 539, A155
Magnelli, B., Saintonge, A., Lutz, D., et al., 2012b, A&A 548, A22
Man, A. & Belli, S., 2018, Nature Astronomy 2, 695
Mannucci, F., Cresci, G., Maiolino, R., Marconi, A., & Gnerucci, A., 2010, MNRAS 408, 2115
Meijerink, R., Glassgold, A. E., & Najita, J. R., 2008, ApJ 676, 518
Melbourne, J. & Boyer, M. L., 2013, ApJ 764, 30
Menéndez-Delmestre, K., Blain, A. W., Smail, I., et al., 2009, ApJ 699, 667
Micelotta, E. R., Jones, A. P., & Tielens, A. G. G. M., 2010a, A&A 510, A37
— 2010b, A&A 510, A36

Mitchell, P. D., Lacey, C. G., Cole, S., & Baugh, C. M., 2014, MNRAS 444, 2637
Moorwood, A. F. M., 1986, A&A 166, 4
Mullaney, J. R., Alexander, D. M., Fine, S., et al., 2013, MNRAS 433, 622
Mullaney, J. R., Alexander, D. M., Goulding, A. D., & Hickox, R. C., 2011, MNRAS 414, 1082
Murata, K. L., Yamada, R., Oyabu, S., et al., 2017, MNRAS 472, 39
Murphy, E. J., Chary, R. .-.-R., Alexander, D. M., et al., 2009, ApJ 698, 1380
Muzzin, A., Marchesini, D., Stefanon, M., et al., 2013, ApJ 777, 18
Narayanan, D., Krumholz, M. R., Ostriker, E. C., & Hernquist, L., 2012, MNRAS 421, 3127
Narayanan, D. & Krumholz, M. R., 2014, MNRAS 442, 1411
Narayanan, D., Krumholz, M., Ostriker, E. C., & Hernquist, L., 2011, MNRAS 418, 664
Neri, R., Cox, P., Omont, A., et al., 2020, A&A 635, A7
Nesvadba, N. P. H., Cañameras, R., Kneissl, R., et al., 2019, A&A 624, A23
Noeske, K. G., Weiner, B. J., Faber, S. M., et al., 2007, ApJ 660, L43
Nordon, R., Lutz, D., Genzel, R., et al., 2012, ApJ 745, 182
Nordon, R., Lutz, D., Shao, L., et al., 2010, A&A 518, L24
O'Dowd, M. J., Schiminovich, D., Johnson, B. D., et al., 2009, ApJ 705, 885
O'Halloran, B., Satyapal, S., & Dudik, R. P., 2006, ApJ 641, 795
Obreschkow, D., Croton, D., De Lucia, G., Khochfar, S., & Rawlings, S., 2009, ApJ 698, 1467
Ojha, R., Stark, A. A., Hsieh, H. H., et al., 2001, ApJ 548, 253
Oliver, S. J., Bock, J., Altieri, B., et al., 2012, MNRAS 424, 1614
Oliver, S. J., Wang, L., Smith, A. J., et al., 2010, A&A 518, L21
Omont, A., Cox, P., Bertoldi, F., et al., 2001, A&A 374, 371
Omont, A., 2007, Reports on Progress in Physics 70, 1099
Pahre, M. A., Ashby, M. L. N., Fazio, G. G., & Willner, S. P., 2004, ApJS 154, 235
Papadopoulos, P. P., Thi, W. .-.-F., & Viti, S., 2002, ApJ 579, 270
— 2004, MNRAS 351, 147
Papadopoulos, P. P., Isaak, K., & van der Werf, P., 2010, ApJ 711, 757
Papadopoulos, P. P., Bisbas, T. G., & Zhang, Z.-Y., 2018, MNRAS 478, 1716
Papadopoulos, P. P., van der Werf, P. P., Xilouris, E. M., et al., 2012, MNRAS 426, 2601

Peeters, E., Spoon, H. W. W., & Tielens, A. G. G. M., 2004, ApJ 613, 986
Peeters, E., Bauschlicher Charles W., J., Allamand ola, L. J., et al., 2017, ApJ 836, 198
Penzias, A. A. & Wilson, R. W., 1965, ApJ 142, 419
Pereira-Santaella, M., Rigopoulou, D., Farrah, D., Lebouteiller, V., & Li, J., 2017, MNRAS 470, 1218
Pereira-Santaella, M., Alonso-Herrero, A., Rieke, G. H., et al., 2010, ApJS 188, 447
Perera, T. A., Chapin, E. L., Austermann, J. E., et al., 2008, MNRAS 391, 1227
Perlmutter, S., Aldering, G., Goldhaber, G., et al., 1999, ApJ 517, 565
Pety, J., Teyssier, D., Fossé, D., et al., 2005, A&A 435, 885
Pilbratt, G. L., Riedinger, J. R., Passvogel, T., et al., 2010, A&A 518, L1
Pineda, J. L., Langer, W. D., Goldsmith, P. F., et al., 2017, ApJ 839, 107
Planck Collaboration, Aghanim, N., Akrami, Y., et al., 2018, arXiv e-prints, arXiv:1807.06209
Poglitsch, A., Waelkens, C., Geis, N., et al., 2010, A&A 518, L2
Pope, A., Bussmann, R. S., Dey, A., et al., 2008a, ApJ 689, 127
Pope, A., Scott, D., Dickinson, M., et al., 2006, MNRAS 370, 1185
Pope, A., Chary, R.-R., Alexander, D. M., et al., 2008b, ApJ 675, 1171
Pope, A., Wagg, J., Frayer, D., et al., 2013, ApJ 772, 92
Popping, G., Decarli, R., Man, A. W. S., et al., 2017, A&A 602, A11
Popping, G., Narayanan, D., Somerville, R. S., Faisst, A. L., & Krumholz, M. R., 2019, MNRAS 482, 4906
Povich, M. S., Stone, J. M., Churchwell, E., et al., 2007, ApJ 660, 346
Pracy, M. B., Ching, J. H. Y., Sadler, E. M., et al., 2016, MNRAS 460, 2
Privon, G. C., Narayanan, D., & Davé, R., 2018, ApJ 867, 102
Puget, J. L. & Leger, A., 1989, ARA&A 27, 161
Regan, M. W., Thornley, M. D., Vogel, S. N., et al., 2006, ApJ 652, 1112
Rémy-Ruyer, A., Madden, S. C., Galliano, F., et al., 2014, A&A 563, A31
Renzini, A., 2006, ARA&A 44, 141
Rho, J., Reach, W. T., Lefloch, B., & Fazio, G. G., 2006, ApJ 643, 965
Rickard, L. J., Palmer, P., Morris, M., Zuckerman, B., & Turner, B. E., 1975, ApJ 199, L75
Riechers, D. A., Bradford, C. M., Clements, D. L., et al., 2013, Nature 496, 329

Riechers, D. A., Pavesi, R., Sharon, C. E., et al., 2019, ApJ 872, 7
Riechers, D. A., Pope, A., Daddi, E., et al., 2014, ApJ 786, 31
Rieke, G. H., Young, E. T., Engelbracht, C. W., et al., 2004, ApJS 154, 25
Rigopoulou, D., Pereira-Santaella, M., Magdis, G. E., et al., 2018, MNRAS 473, 20
Rigopoulou, D., Spoon, H. W. W., Genzel, R., et al., 1999, AJ 118, 2625
Roche, P. F., Aitken, D. K., Smith, C. H., & Ward, M. J., 1991, MNRAS 248, 606
Rodighiero, G., Daddi, E., Baronchelli, I., et al., 2011, ApJ 739, L40
Roussel, H., Sauvage, M., Vigroux, L., & Bosma, A., 2001, A&A 372, 427
Rujopakarn, W., Rieke, G. H., Weiner, B. J., et al., 2013, ApJ 767, 73
Saintonge, A., Lutz, D., Genzel, R., et al., 2013, ApJ 778, 2
Saintonge, A., Wilson, C. D., Xiao, T., et al., 2018, MNRAS 481, 3497
Sajina, A., Yan, L., Armus, L., et al., 2007, ApJ 664, 713
Sajina, A., Yan, L., Lutz, D., et al., 2008, ApJ 683, 659
Sales, D. A., Pastoriza, M. G., & Riffel, R., 2010, ApJ 725, 605
Salpeter, E. E., 1955, ApJ 121, 161
Sanders, D. B. & Mirabel, I. F., 1996, ARA&A 34, 749
Sanders, D. B., Scoville, N. Z., & Soifer, B. T., 1991, ApJ 370, 158
Sandstrom, K. M., Bolatto, A. D., Bot, C., et al., 2012, ApJ 744, 20
Sandstrom, K. M., Bolatto, A. D., Draine, B. T., Bot, C., & Stanimirović, S., 2010, ApJ 715, 701
Sandstrom, K. M., Leroy, A. K., Walter, F., et al., 2013, ApJ 777, 5
Santini, P., Maiolino, R., Magnelli, B., et al., 2014, A&A 562, A30
Sargent, M. T., Béthermin, M., Daddi, E., & Elbaz, D., 2012, ApJ 747, L31
Sargent, M. T., Daddi, E., Béthermin, M., et al., 2014, ApJ 793, 19
Schinnerer, E., Meidt, S. E., Colombo, D., et al., 2017, ApJ 836, 62
Schinnerer, E., Meidt, S. E., Pety, J., et al., 2013, ApJ 779, 42
Schmidt, M., 1959, ApJ 129, 243
Schneider, N., Simon, R., Kramer, C., et al., 2003, A&A 406, 915
Schreiber, C., Elbaz, D., Pannella, M., et al., 2018, A&A 609, A30
Schreiber, C., Pannella, M., Elbaz, D., et al., 2015, A&A 575, A74
Scoville, N., Aussel, H., Brusa, M., et al., 2007, ApJS 172, 1
Scoville, N., Aussel, H., Sheth, K., et al., 2014, ApJ 783, 84
Scoville, N., Lee, N., Vanden Bout, P., et al., 2017a, ApJ 837, 150
Scoville, N., Sheth, K., Aussel, H., et al., 2016, ApJ 820, 83

Scoville, N., Murchikova, L., Walter, F., et al., 2017b, ApJ 836, 66
Sellgren, K., 1984, ApJ 277, 623
Shapley, A. E., Steidel, C. C., Pettini, M., & Adelberger, K. L., 2003, ApJ 588, 65
Sharples, R., Bender, R., Agudo Berbel, A., et al., 2013, The Messenger 151, 21
Shi, Y., Helou, G., Yan, L., et al., 2011, ApJ 733, 87
Shipley, H. V., Papovich, C., Rieke, G. H., Brown, M. J. I., & Moustakas, J., 2016, ApJ 818, 60
Shipley, H. V., Papovich, C., Rieke, G. H., et al., 2013, ApJ 769, 75
Shivaei, I., Reddy, N. A., Shapley, A. E., et al., 2017, ApJ 837, 157
Silverman, J. D., Daddi, E., Rodighiero, G., et al., 2015, ApJ 812, L23
Simpson, C., Westoby, P., Arumugam, V., et al., 2013, MNRAS 433, 2647
Simpson, J. M., Smail, I., Swinbank, A. M., et al., 2017, ApJ 839, 58
Smith, J. D. T., Draine, B. T., Dale, D. A., et al., 2007, ApJ 656, 770
Smith, R. J., Glover, S. C. O., Clark, P. C., Klessen, R. S., & Springel, V., 2014, MNRAS 441, 1628
Smolčić, V., Novak, M., Bondi, M., et al., 2017, A&A 602, A1
Smoot, G. F., Bennett, C. L., Kogut, A., et al., 1992, ApJ 396, L1
Solomon, P. M., Downes, D., Radford, S. J. E., & Barrett, J. W., 1997, ApJ 478, 144
Solomon, P. M., Rivolo, A. R., Barrett, J., & Yahil, A., 1987, ApJ 319, 730
Solomon, P. M. & Vanden Bout, P. A., 2005, ARA&A 43, 677
Sparre, M., Hayward, C. C., Springel, V., et al., 2015, MNRAS 447, 3548
Speagle, J. S., Steinhardt, C. L., Capak, P. L., & Silverman, J. D., 2014, ApJS 214, 15
Spilker, J. S., Marrone, D. P., Aravena, M., et al., 2016, ApJ 826, 112
Spoon, H. W. W., Marshall, J. A., Houck, J. R., et al., 2007, ApJ 654, L49
Steidel, C. C., Adelberger, K. L., Shapley, A. E., et al., 2003, ApJ 592, 728
Stockmann, M., Toft, S., Gallazzi, A., et al., 2020, ApJ 888, 4
Strateva, I., Ivezić, Ž., Knapp, G. R., et al., 2001, AJ 122, 1861
Stutzki, J., Graf, U. U., Haas, S., et al., 1997, ApJ 477, L33
Tacchella, S., Dekel, A., Carollo, C. M., et al., 2016, MNRAS 457, 2790
Tacconi, L. J., Genzel, R., Neri, R., et al., 2010, Nature 463, 781
Tacconi, L. J., Genzel, R., Saintonge, A., et al., 2018, ApJ 853, 179
Tacconi, L. J., Genzel, R., Smail, I., et al., 2008, ApJ 680, 246

Tacconi, L. J., Neri, R., Chapman, S. C., et al., 2006, ApJ 640, 228
Tacconi, L. J., Neri, R., Genzel, R., et al., 2013, ApJ 768, 74
Tan, B.-K., Leech, J., Rigopoulou, D., et al., 2013, MNRAS 436, 921
Tan, Q., Daddi, E., Magdis, G., et al., 2014, A&A 569, A98
Thilker, D. A., Boissier, S., Bianchi, L., et al., 2007, ApJS 173, 572
Thomas, D., Maraston, C., Bender, R., & Mendes de Oliveira, C., 2005, ApJ 621, 673
Tielens, A. G. G. M., 2008, ARA&A 46, 289
— 2011, *The Molecular Universe*, ed. by J. Cernicharo & R. Bachiller, vol. 280, IAU Symposium, 3
Tielens, A. G. G. M., McKee, C. F., Seab, C. G., & Hollenbach, D. J., 1994, ApJ 431, 321
Tielens, A. G. G. M., Seab, C. G., Hollenbach, D. J., & McKee, C. F., 1987, ApJ 319, L109
Toft, S., Gallazzi, A., Zirm, A., et al., 2012, ApJ 754, 3
Valentino, F., Magdis, G. E., Daddi, E., et al., 2018, ApJ 869, 27
Valentino, F., Magdis, G. E., Daddi, E., et al., 2020a, ApJ 890, 24
Valentino, F., Tanaka, M., Davidzon, I., et al., 2020b, ApJ 889, 93
Valiante, E., Lutz, D., Sturm, E., et al., 2007, ApJ 660, 1060
van Dokkum, P. G. & van der Marel, R. P., 2007, ApJ 655, 30
Veilleux, S., Rupke, D. S. N., Kim, D. .-.-C., et al., 2009, ApJS 182, 628
Voit, G. M., 1992, ApJ 399, 495
Wakelam, V., Bron, E., Cazaux, S., et al., 2017, Molecular Astrophysics 9, 1
Walter, F., Weiß, A., Downes, D., Decarli, R., & Henkel, C., 2011, ApJ 730, 18
Weedman, D. W., Hao, L., Higdon, S. J. U., et al., 2005, ApJ 633, 706
Weiß, A., Henkel, C., Downes, D., & Walter, F., 2003, A&A 409, L41
Weiß, A., Walter, F., & Scoville, N. Z., 2005, A&A 438, 533
Werner, M. W., Roellig, T. L., Low, F. J., et al., 2004, ApJS 154, 1
Whitaker, K. E., Franx, M., Leja, J., et al., 2014, ApJ 795, 104
Whitaker, K. E., van Dokkum, P. G., Brammer, G., & Franx, M., 2012, ApJ 754, L29
Williams, W. L. & Röttgering, H. J. A., 2015, MNRAS 450, 1538
Willott, C. J., Rawlings, S., Blundell, K. M., & Lacy, M., 1999, MNRAS 309, 1017
Wilson, A. S. & Colbert, E. J. M., 1995, ApJ 438, 62

Wilson, C. D., Warren, B. E., Israel, F. P., et al., 2012, MNRAS 424, 3050
Wolfire, M. G., Hollenbach, D., McKee, C. F., Tielens, A. G. G. M., & Bakes, E. L. O., 1995, ApJ 443, 152
Wolfire, M. G., Hollenbach, D., & McKee, C. F., 2010, ApJ 716, 1191
Wu, Y., Helou, G., Armus, L., et al., 2010, ApJ 723, 895
Xie, Y. & Ho, L. C., 2019, ApJ 884, 136
Yan, L., Tacconi, L. J., Fiolet, N., et al., 2010, ApJ 714, 100
Yan, L., Sajina, A., Fadda, D., et al., 2007, ApJ 658, 778
Yang, C., Omont, A., Beelen, A., et al., 2017, A&A 608, A144